COLLECTIVE FLOW IN INTERMEDIATE ENERGY HEAVY-ION COLLISIONS

By

Robert Pak

A DISSERTATION

Submitted to
Michigan State University
in partial fulfillment of the requirements
for the degree of

DOCTOR OF PHILOSOPHY

Department of Physics and Astronomy

1996

ABSTRACT

COLLECTIVE FLOW IN INTERMEDIATE
ENERGY HEAVY-ION COLLISIONS

By

Robert Pak

Collective flow in intermediate energy heavy-ion collisions has been investigated using the Michigan State University 4π Array upgraded with the High Rate Array (HRA). The projectile-target combination studied was ^{40}Ar+^{45}Sc at bombarding energies ranging between 35 and 115 MeV/nucleon. The impact parameter b of each event was assigned through cuts on centrality variables measured with the improved acceptance of the MSU 4π Array.

Collective radial flow of light fragments in the nuclear disassembly process is demonstrated through transverse energy production. The mean transverse kinetic energy $\langle E_t \rangle$ of the different particle types increases with event centrality, and increases as a function of the incident beam energy. Comparison of our measured values of $\langle E_t \rangle$ shows agreement with predictions of Boltzmann-Uehling-Uhlenbeck (BUU) model and WIX multifragmentation model calculations. The radial flow extracted from $\langle E_t \rangle$ accounts for approximately half of the emitted particle's energy for the heavier fragments ($Z \geq 4$) at the highest beam energy studied.

Collective directed transverse flow was measured with a transverse momentum analysis method in which the reaction plane was determined using the azimuthal correlation technique. The energy at which collective transverse flow in the reaction plane disappears, termed the balance energy E_{bal}, is found to increase approximately linearly as a function of impact parameter. Comparison of our measured values of $E_{bal}(b)$ shows agreement with predictions of Quantum Molecular Dynamics (QMD) model calculations.

To my lovely wife

ACKNOWLEDGEMENTS

Upon attaining this goal of my doctorate degree, I must reflect back upon what has brought me to this point. So I devote this space to acknowledge those who have made this reality, although these few words cannot possibly convey the proper gratitude for what has been given unto me. The Lord God has been good to me, for I find myself in most fortunate circumstances. Even at times when I have failed to recognize this, I was always able to return. That the word "we" is used throughout the remainder of this manuscript is no mistake, rather it serves as a reminder of the collective contribution of the following people to achieve this end.

I do not know how to begin to express my gratitude to Myung-Hee Pak, to whom this work is dedicated. Together we have overcome the many challenges to achieve this dream in the hope of a better life for our family. We wish to express our deepest heartfelt gratitude for the unconditional love and support given to us by our parents and our siblings.

I will always be deeply indebted to Prof. Gary Westfall for the giving me the opportunity to become a scientist. Gary Westfall has continued to stand by me throughout my graduate career. Had it not been for Gary Westfall, I would not have written the words upon this page. His ideas were the seeds that became this document, and every page bears his imprint. I am truly grateful for his unflagging support, his invaluable guidance, and his irrepressible sense of humor. Thank God for Gary Westfall. Kowwabungga Dude!!

I would like to thank Prof. Wolfgang Bauer for bringing his keen insight to bear on the many problems I presented before him. After we'd stop dancing about our latest physics result, we'd show them to Wolfgang and he'd gently bring us back to earth. Prof. Julius S. Kovacs has been faithful mentor since the first day I walked into the PA Dept., and I hope I have met his expectations when he selected me to come to MSU as a doctoral candidate. I would also like to recognize the other members on my thesis guidance committee, Drs. Gerald Pollack and Michael Thoennessen for their time and effort in the careful reading of my manuscript. Prof. Pollack's "How ya doin' Pak?" ringing down the halls of the PA Dept. in my first year at MSU made them a welcome place to be.

I have profited from the careful instruction of all the professors in my graduate coursework at MSU. Of special assistance to me were Profs. Dan Stump, Thomas Kaplan, and Jerzy Borysowicz whose solid encouragement and patient teaching helped me overcome the candidacy exam. I have benefited greatly from the course in heavy-ion reactions taught by Prof. Pawel Danielewicz, and all the helpful discussions with him related to my research since then. The education these faculty have afforded me has brought me to the realization that MSU/NSCL is a world-class institution to receive a degree in nuclear science.

I would like to individually thank the members of the 4π Group whose tenure coincided with my stint in the group. Thanks to Skip Vander Molen who "put-out the fire" countless times during 4π runs. Skip's phone number is one of the most important pieces of information you need to successfully finish a 4π experiment. Thanks to Bill Llope for initiating me to the fine art of data analysis and simulation. Bill's the embodiment of Gary's fireball model. Thanks to Roy Lacey who oversaw the production of my first set of physics tapes by fillin' in the groove while Gary was on sabbatical. Thanks to Aruna Nadasen, Darren Craig, and John Svoboda for many

tireless hours of gain matching the data.

To the rest of the staff at the NSCL, it has indeed been a pleasure working together. I never cease to amaze at the help I have received from all departments at the lab to complete a project or experiment. In particular I must mention Jim Wagner and Dennis Swan whose technical expertise made the design, fabrication, and assembly of the High Rate Array possible.

I am truly fortunate not only to count among my fellow graduate students, but also to be in the same research group as Nathan Stone. Nathan has been the little brother I never had, and the friendship we have built together is best thing I take with me when I leave the lab. Other graduate students who have selflessly assisted me in innumerable ways along the very busy path to achieving their own doctorate degrees were Stefan Hannuschke, Jerome Lauret, Easwar Ramakrishnan, Georg Hoffstatter, Khodr Shamseddine, Sangil Hyun, Mathias Steiner, and Yeong Duk Kim. Sometimes, simply by being there. If I could be like each of them in some small way, then I am a better man for it.

Finally, I'd like to thank my son Ted for reminding me what really matters in life, and for helping make Figures 3.1 and 3.7.

Contents

LIST OF TABLES ix

LIST OF FIGURES x

1 Introduction 1

1.1 Background 1
1.2 Radial Flow 8
1.3 Directed Transverse Flow 10
1.4 Thesis Structure 17

2 Experimental Details 18

2.1 Beams and Target 18
2.2 Detectors 19
2.2.1 Geometry 19
2.2.2 Specifications 27
2.3 Electronics 31
2.4 Raw Data 34
2.5 Data Calibration and Reduction 38

3 Event Characterization 43

3.1 Introduction 43
3.2 Impact Parameter 44
3.3 Reaction Plane 54
3.4 Temperature 65

4 Radial Flow 69

4.1 Introduction 69
4.2 Transverse Energy Production 71
4.3 BUU Model 79

4.4 Comparison to BUU and WIX 84
4.5 Conclusions 91

5 Directed Transverse Flow **92**
5.1 Introduction 92
5.2 Preliminary Results 93
5.3 Transverse Momentum Analysis 100
5.4 Balance Energy 111
5.5 Comparison to QMD 118
5.6 Conclusions 121

6 Conclusion **122**

A Mean Angles for the Phoswiches **124**

LIST OF REFERENCES **127**

List of Tables

2.1 Solid angle subtended by the ball phoswiches. 20
2.2 Solid angle subtended by the HRA phoswiches. 27
2.3 Phoswich scintillator specifications. 28
2.4 Low energy thresholds for the HRA. 30
2.5 Low energy thresholds for the ball telescopes. 30

3.1 Reduced impact parameter bins. 51

4.1 Radial flow parameters. 88

5.1 Balance energies for four reduced impact parameter bins. 115

A.1 Mean angles for the ball phoswiches. 125
A.2 Mean angles for the HRA phoswiches. 126

List of Figures

1.1 Equation of state for two different values of the compressibility of nuclear matter. 3

1.2 Measured balance energies for central collisions of nearly symmetric entrance channels compared with the predictions of the BUU model for a soft EOS with a density dependent reduction of the in-medium cross sections. 4

1.3 Participant-spectator geometry used in the Nuclear Fireball Model. . 5

1.4 Nucleon density contour plots in the reaction plane at three impact parameters for 400 MeV/nucleon Au + Au from BUU theory. 7

1.5 Measured c.m. kinetic energy spectra for light fragments emitted into $\theta_{\text{c.m.}} = 90° \pm 15°$ from 1.0 GeV/nucleon Au + Au collisions. 9

1.6 Momentum distributions of protons, deuterons, helions, and pions from central 800 MeV/nucleon La + La collision within the c.m. polar angle range $60° \leq \theta_{\text{c.m.}} \leq 120°$. 11

1.7 Schematic representation of the directed transverse flow in the c.m. frame for three incident energies: (a) $E < E_{bal}$; (b) $E = E_{bal}$; and (c) $E > E_{bal}$. 13

1.8 Fraction of the mean transverse momentum in the reaction plane versus the c.m. rapidity for various fragment types from semi-central Au + Au collisions at 200 MeV/nucleon. 14

1.9 Mean transverse momenta calculated from BUU theory for mass 40 projectiles and mass 40, 100, and 197 targets, at three impact parameters, and four bombarding energies. 16

2.1 Basic geometry of the MSU 4π Array. 20

2.2 The High Rate Array (HRA). 22

2.3 The Maryland Forward Array (MFA). 23

2.4 Cross-sectional view of the forward arrays. 24

2.5 Simulation results for double hits in HRA designs. 25

2.6 HRA numbering scheme. 26

2.7 MSU 4π module 28

2.8 Phoswich signal and gates. 29

2.9 A MSU 4π Bragg Curve Counter (BCC). 31
2.10 Electronics layout for the MSU 4π Array. 32
2.11 HRA ΔE-E spectrum. 35
2.12 Expanded HRA ΔE-E spectrum. 36
2.13 BCC vs fast plastic spectrum. 39

3.1 Geometrical description of the impact vector and the reaction plane. . 44
3.2 Impact-parameter-inclusive centrality variable distributions. 47
3.3 Reduced impact parameter as a function of centrality variable. 48
3.4 Renormalization of the inclusive $\hat{E}_t$ spectrum to determine b_{max} for the Ball-2 data. 50
3.5 Fraction of events in each $\hat{b}$ bin for cuts on N_{chgd}, Z_{mr}, and $\hat{E}_t$. 52
3.6 Means and rms widthes of $\langle p_x/p_t \rangle$ plotted vs $\hat{E}_t$. 53
3.7 Definition of the forward side of the reaction plane for both attractive and repulsive scattering. 54
3.8 Quantities used to determine the reaction plane with the azimuthal correlation method. 56
3.9 Distribution of azimuthal angle differences between reaction planes in the event and the average value of the event. 58
3.10 Distribution of azimuthal angle differences between reaction planes found using the transverse momentum analysis and the azimuthal correlation method. 59
3.11 Azimuthal distribution of the differences between reaction planes found for the entire event and reaction planes found leaving out the POI. . 60
3.12 Correlation between the azimuthal angles of reaction planes found for different particle types as the POI. 61
3.13 Azimuthal distributions of all charged particles from 45 MeV/nucleon ^{40}Ar+^{45}Sc reactions under various conditions. 62
3.14 Azimuthal distributions for $Z = 3$ fragments from ^{40}Ar+^{45}Sc reactions at four incident beam energies. 64
3.15 Kinetic energy spectra in the laboratory frame for protons from central ^{40}Ar+^{45}Sc collisions at $\theta_{\rm c.m.} = 90° \pm 15°$ for nine beam energies. . . . 67
3.16 Kinetic energy spectra in the laboratory frame for lithiums from central ^{40}Ar+^{45}Sc collisions at $\theta_{\rm c.m.} = 90° \pm 15°$ for nine beam energies. . . . 68

4.1 Mean transverse kinetic energy from ^{40}Ar+^{45}Sc reactions at beam energy 115 MeV/nucleon versus fragment mass number for various centrality and angular gating conditions. 71

4.2 Mean transverse kinetic energy of fragments from ^{40}Ar+^{45}Sc reactions at polar angles $\theta_{\text{c.m.}} = 90° \pm 15°$ versus incident beam energy for two impact parameters bins. 73

4.3 Same as Figure 4.2 except with an artificial common low-energy threshold set for all fragments with $Z \leq 5$. 75

4.4 Mean transverse kinetic energy of fragments from central ^{40}Ar+^{45}Sc collisions versus incident beam energy for two c.m. polar angle bins. . 77

4.5 Mean transverse kinetic energy of fragments from ^{40}Ar+^{45}Sc reactions at polar angles $\theta_{\text{c.m.}} = 90° \pm 15°$ versus the reduced impact parameter at four incident beam energies. 78

4.6 Mean transverse kinetic energy per nucleon for ^{40}Ar+^{45}Sc reactions at four bombarding energies as a function of time from BUU theory. . . 80

4.7 Maximum density attained in ^{40}Ar+^{45}Sc reactions at two bombarding energies as a function of time from BUU theory. 81

4.8 Mean total kinetic energy per nucleon, and its longitudinal and transverse components plotted as a function of time for 115 MeV/nucleon ^{40}Ar+^{45}Sc collisions from BUU theory. 83

4.9 Mean transverse kinetic energy per nucleon of fragments from central ^{40}Ar+^{45}Sc collisions at polar angles $\theta_{\text{c.m.}} = 90° \pm 15°$ versus incident beam energy compared with predictions of BUU model calculations. . 85

4.10 Mean transverse kinetic energy of fragments from central ^{40}Ar+^{45}Sc reactions at polar angles $\theta_{\text{c.m.}} = 90° \pm 15°$ versus incident beam energy compared with predictions of WIX model calculations assuming half the available energy is associated with radial flow. 90

5.1 Mean fraction of the transverse momentum in the reaction plane determined using the PLF for protons versus the reduced c.m. rapidity for 45 MeV/nucleon ^{40}Ar+^{45}Sc reactions. 95

5.2 Transverse momentum distribution in the reaction plane determined using the PLF for protons from 45 MeV/nucleon ^{40}Ar+^{45}Sc reactions. 96

5.3 Transverse momentum in the reaction per nucleon for all POI versus reduced c.m. rapidity for 45 MeV/nucleon ^{40}Ar+^{45}Sc reactions. 98

5.4 Mean fraction of the transverse momentum in the reaction plane for all POI versus the reduced c.m. rapidity for central ^{40}Ar+^{45}Sc collisions at 45 MeV/nucleon compared to FREESCO simulations. 99

5.5 Mean transverse momentum in the reaction plane versus the reduced c.m. rapidity for $Z = 2$ fragments from 55 MeV/nucleon ^{40}Ar+^{45}Sc reactions in seven reduced impact parameter bins. 101

5.6 Mean transverse momentum in the reaction plane versus the reduced c.m. rapidity for $Z = 1$ fragments from 55 MeV/nucleon ^{40}Ar+^{45}Sc reactions in seven reduced impact parameter bins. 102

5.7 Mean transverse momentum in the reaction plane versus the reduced c.m. rapidity for $Z = 3$ fragments from 55 MeV/nucleon ^{40}Ar+^{45}Sc reactions in seven reduced impact parameter bins. 103

5.8 Directed transverse flow as a function of reduced impact parameter for He fragments from ^{40}Ar+^{45}Sc collisions at eight beam energies. 105

5.9 Mean transverse momentum in the reaction plane versus the reduced c.m. rapidity for $Z = 2$ fragments from ^{40}Ar+^{45}Sc reactions with reduced impact parameter in BIN1. 107

5.10 Mean transverse momentum in the reaction plane versus the reduced c.m. rapidity for $Z = 2$ fragments from ^{40}Ar+^{45}Sc reactions with reduced impact parameter in BIN2. 108

5.11 Mean transverse momentum in the reaction plane versus the reduced c.m. rapidity for $Z = 2$ fragments from ^{40}Ar+^{45}Sc reactions with reduced impact parameter in BIN3. 109

5.12 Mean transverse momentum in the reaction plane versus the reduced c.m. rapidity for $Z = 2$ fragments from ^{40}Ar+^{45}Sc reactions with reduced impact parameter in BIN4. 110

5.13 Excitation functions of the measured transverse flow in the reaction plane for $Z = 2$ fragments at four reduced impact parameter bins for ^{40}Ar+^{45}Sc reactions. 112

5.14 Excitation functions of the measured reduced transverse flow in the reaction plane calculated with the recoil correction for $Z = 2$ fragments at four reduced impact parameter bins for ^{40}Ar+^{45}Sc reactions. . . . 114

5.15 Excitation functions of the measured transverse flow in the reaction plane calculated for $Z = 2$ fragments at four $\hat{b}$ bins for ^{40}Ar+^{45}Sc collisions taken with a HRA-1 hardware trigger. 116

5.16 Excitation functions of the measured transverse flow in the reaction plane for three particle types at four reduced impact parameter bins for ^{40}Ar+^{45}Sc reactions. 117

5.17 Measured balance energies for ^{40}Ar+^{45}Sc reactions at the four most central reduced impact parameter bins compared with the predictions of the QMD model for ^{40}Ca+^{40}Ca reactions. 119

5.18 Measured balance energies for ^{40}Ar+^{45}Sc reactions at the four most central reduced impact parameter bins compared with the predictions of the QMD model with and without momentum dependence in the mean field for ^{40}Ca+^{40}Ca reactions. 120

Chapter 1

Introduction

1.1 Background

This thesis is entitled "Collective Flow in Intermediate Energy Heavy-Ion Collisions", because we will explain the collective motion manifested in the fragment emission pattern resulting from the collision of two nuclei. Collective motion is ordered motion characterized by the correlation between particle positions and momenta of a dynamic origin (superimposed on a random background). Examples of collective motion in heavy-ion collisions include:

(1) rotational motion
(2) radial flow
(3) directed transverse flow
(4) squeeze-out.

The two collective modes we will examine here in detail are radial flow and directed transverse flow, which are the most significant forms of collective motion for the originally proposed beam energies of the data set comprising this thesis (65 - 115 MeV/nucleon). Rotational motion becomes an important contribution to the collective motion for non-central events below these incident beam energies [Wils91b]. This collective mode is the result of "friction" between the colliding nuclei, which causes partial orbiting due to the mean-field deflection. Squeeze-out is the enhancement

of particle emission orthogonal to the reaction plane, *i.e.,* the plane containing the the beam axis and the center of the target. Heavier systems colliding at incident beam energies higher than those studied here [Gutb89] are required to attain the compression necessary to produce a clear squeeze-out signal. In this chapter we will introduce some of the basic concepts to allow a better understanding of the topics to be discussed in detail in the following chapters. The citations in this chapter are not meant to encompass entirely the body of literature that exists in the field, and additional references are provided in the discussion of following chapters. Excellent introductory works on collective flow in heavy-ion reaction dynamics are also found elsewhere [Gutb91, DGup93].

One of the fundamental problems remaining in the field of heavy-ion reaction dynamics is the description of nuclear matter in terms of an equation of state (EOS). A more familiar example of an equation of state is the ideal gas law, and likewise the nuclear EOS would completely describe all the measurable properties of matter comprising the nucleus in a verifiable self-consistent manner. The idea of deriving an EOS to describe the bulk properties of nuclear matter from heavy-ion collisions has existed for over 25 years. For infinite nuclear matter in its ground state it is established that the binding energy $B \approx 16$ MeV/nucleon at a saturation density $\rho_0 \approx 0.17$ nucleons fm^{-3}. The minima of the curves shown in Figure 1.1 represent the point at which nuclear matter is in the ground state. This figure [Moli85a] shows a calculation for the compressional energy E_C (the sum of the potential energy and the Fermi energy) as a function of the reduced density ρ/ρ_0 for two different values of the compressibility κ. The solid (dashed) line is for a stiff (soft) EOS for which $\kappa = 380$ MeV ($\kappa = 200$ MeV). The compressibility is a measure of how difficult it is to push the system away from its equilibrium density, and is a property of the mean field collectively produced by the nucleons. Heavy-ion collisions excite nuclear

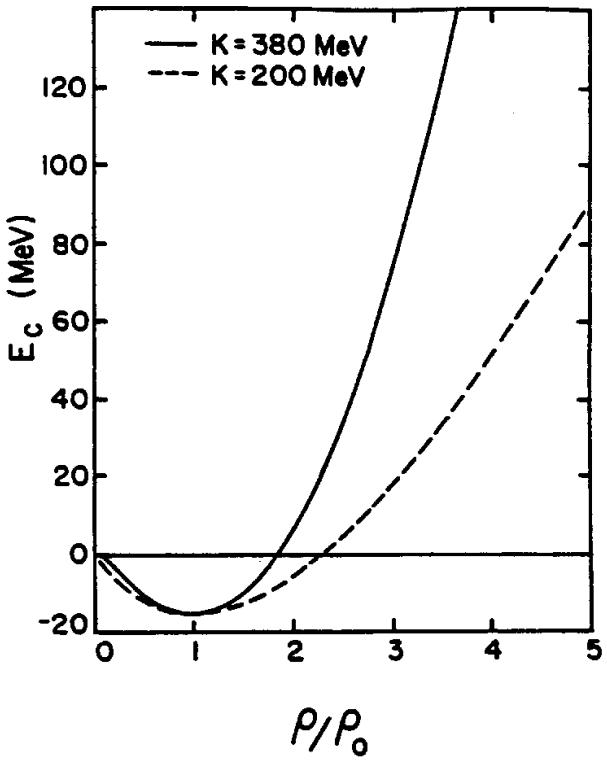

Figure 1.1: The equation of state for two different values of the compressibility of nuclear matter [Moli85a].

matter into a region of higher density above the ground state. A higher value of κ for the nuclear matter should produce larger transverse momenta and consequently more "flow". Depending on how the results derived from the measured quantities for the excited matter compare to these calculated curves, it should in principle be possible to distinguish between equations of state with different stiffness. Although at this time the value of κ has been determined to only within large error bars, the study of excited nuclear matter produced in heavy-ion collisions has provided further constraints on the nuclear EOS.

A good example of how information pertaining to the nuclear EOS can be extracted by comparing the experimentally measured data to the values predicted by theoretical model calculations is shown in Figure 1.2. From the mass dependence of the disappearance of directed transverse flow, it has been deduced that there is

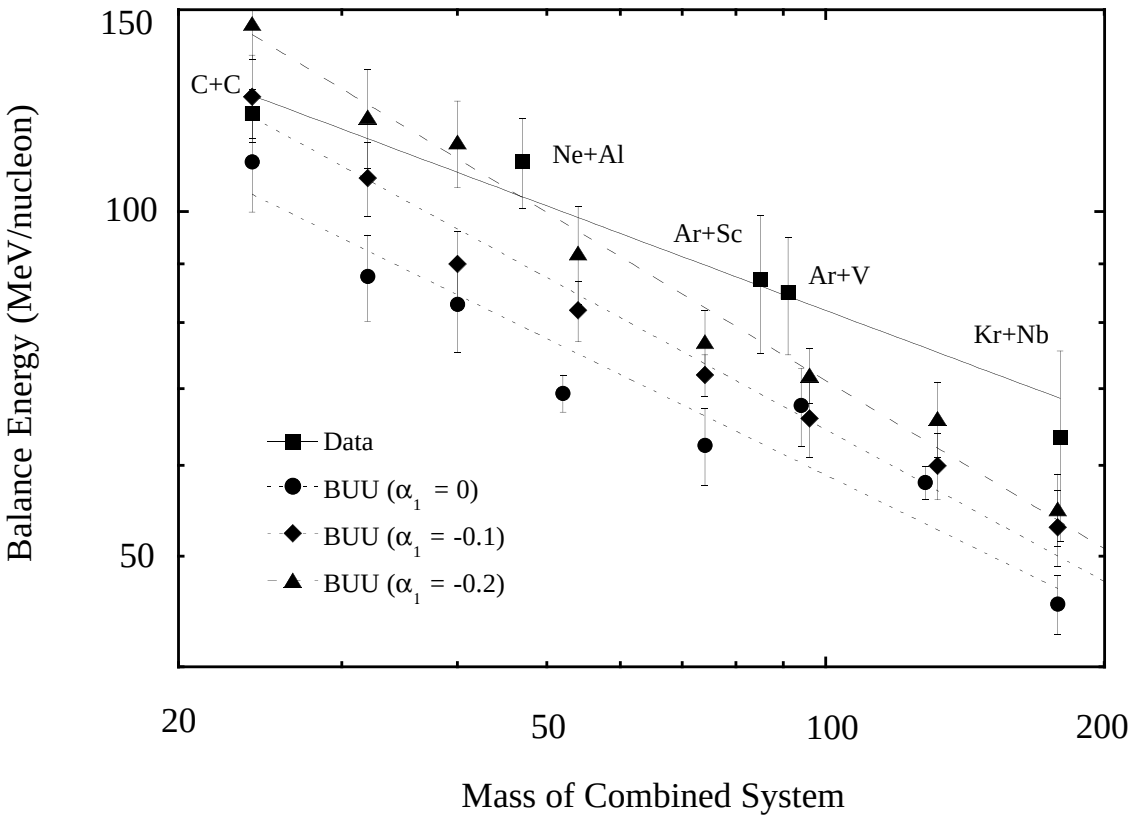

Figure 1.2: Measured values (squares) of the balance energy for central collisions of nearly symmetric entrance channels of different mass compared with the predictions of the BUU model for a soft EOS with a density dependent reduction of the in-medium cross sections of 0% (circles), 10% (diamonds), and 20% (triangles) [West93, Klak93]. The experimental value for ^{40}Ar+^{51}V is from [Krof91], and the lines correspond to power law fits.

a density dependent reduction of the in-medium nucleon-nucleon cross section from its free-space value. The squares are the experimental values of the balance energies (the energy at which directed transverse flow disappears) for central collisions of the approximately symmetric entrance channels: ^{12}C+^{12}C; ^{20}Ne+^{27}Al; ^{40}Ar+^{45}Sc; ^{40}Ar+^{51}V; and ^{86}Kr+^{93}Nb [West93]. The measured balance energies exhibit an $A^{-1/3}$ dependence where A is the mass of the combined system (solid line). This is due to the competition between the repulsive nucleon-nucleon scattering, which scales as the volume A, and the attractive mean field interaction, which scales as the surface area $A^{2/3}$. The remaining points in this diagram are the balance energies calculated using a Boltzmann-Uehling-Uhlenbeck (BUU) model with a soft EOS (κ = 200 MeV) at a fixed impact parameter for central collisions [Klak93]. The theoretical values which are in best agreement with the experimental data were calculated with 20% reduction of the in-medium nucleon-nucleon cross section (triangles).

A simplified schematic picture of what occurs in a heavy-ion collision is shown in Figure 1.3. This will be referred to throughout the remainder of this thesis as

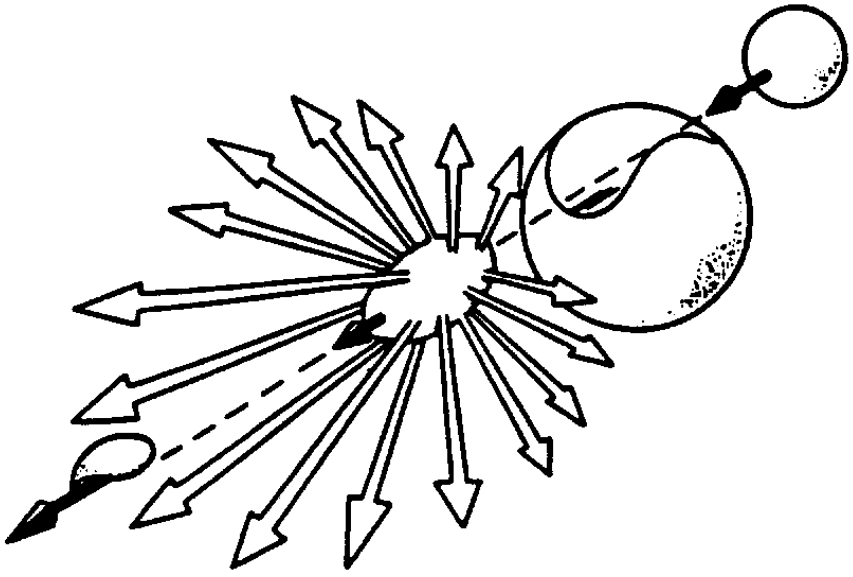

Figure 1.3: The participant-spectator geometry used in the Nuclear Fireball Model [West76].

the participant-spectator geometry from the Nuclear Fireball Model [West76]. The projectile (which approaches from the upper right) collides with the stationary target creating an excited participant volume from the overlapping region. The velocity and excitation energy of this participant "fireball" can be deduced from the assumption of a completely inelastic collision and clean cut geometry. The participant source rapidly de-excites by decaying into numerous light charged particles (LCPs have $Z \leq 2$), and intermediate-mass-fragments (IMFs have $3 \leq Z \lesssim 20$). The number or multiplicity of these fragments in the event depends upon the violence of the collision, *i.e.,* the centrality and incident beam energy. For non-central events a target and projectile remnant are created (which also move off to the lower left corner in the figure), and these spectator sources may also de-excite via fragment emission.

Dynamical transport models have been highly successful in predicting the effects of collective motion in heavy-ion collisions. These models incorporate the collisions produced in the intranuclear cascade with an additional interaction mediated by the nuclear mean field. The Boltzmann-Uehling-Uhlenbeck (BUU) and Quantum Molecular Dynamics (QMD) models are examples of this approach. The difference between radial and directed transverse flow is demonstrated in Figure 1.4 using the BUU model, which shows the evolution of the nucleon density profile projected onto the reaction plane for a 400 MeV/nucleon Au + Au collision at three different impact parameters [Dani95]. The perspective of this figure is looking down onto the reaction plane where the beam direction is along the z-axis. The values on the contours represent different fractions of normal nuclear matter density (ρ/ρ_0 = 0.1, 0.5, 1.0, 1.5, and 2.0). For a perfectly central collision ($b = 0$) in the column on the left-hand side, the incident projectile is completely stopped, and the nuclear matter of the equilibrated compound system is compressed and heated. Subsequently, the compressional energy stored in the longitudinal direction is converted to motion in the transverse

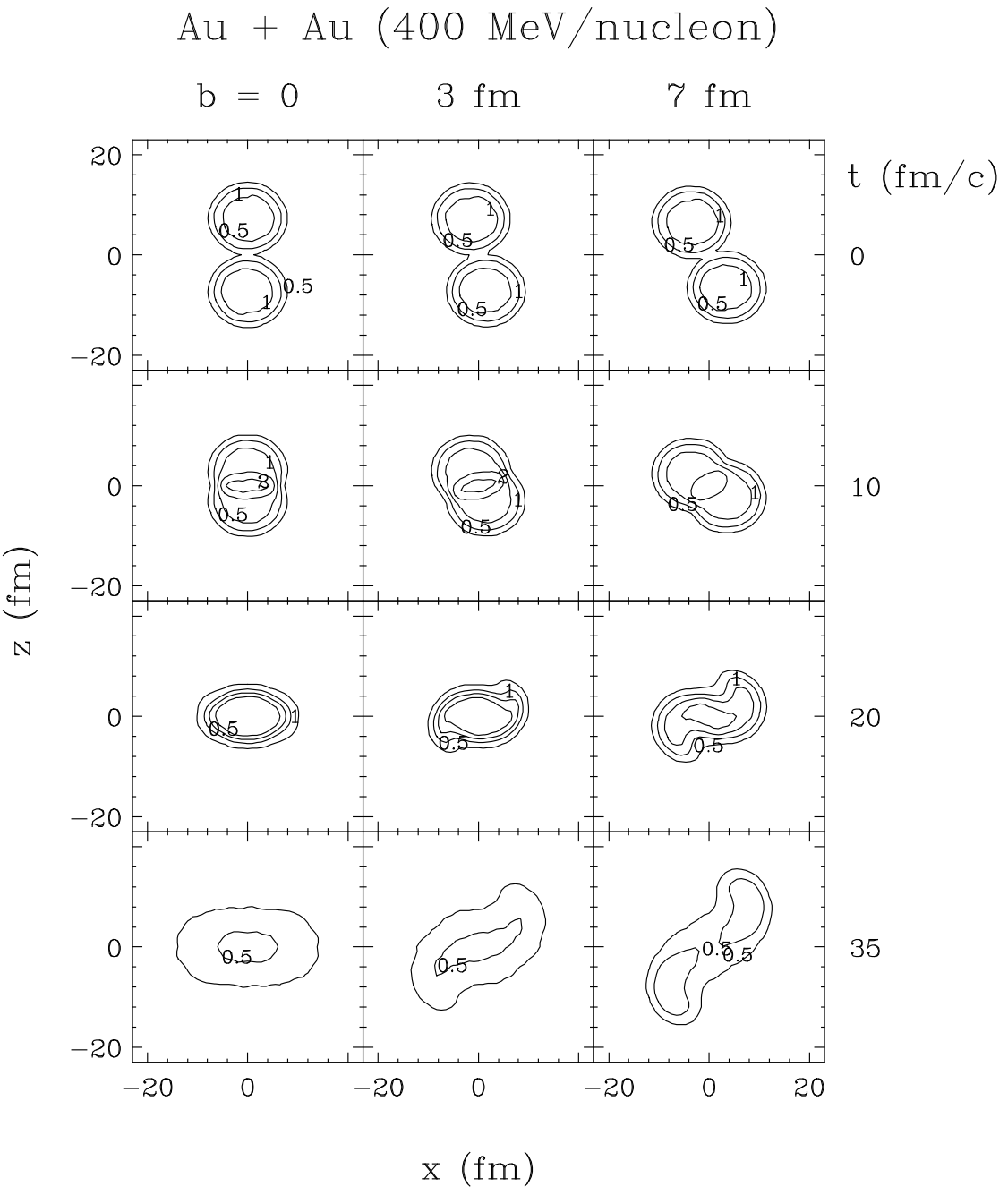

Figure 1.4: Contour plots of nucleon density in the reaction plane at three impact for 400 MeV/nucleon Au + Au from BUU theory [Dani95]. The displayed contour lines are for the reduced densities $\rho/\rho_0 = 0.1$, 0.5, 1.0, 1.5, and 2.0.

direction. This radial expansion has been suggested to result in increased curvature in the single-particle kinetic energy spectra at 90° in the center-of-mass (c.m.) frame [Siem79], and enhanced values for the mean transverse kinetic energy $\langle E_t \rangle$ at this angle [Doss88]. At larger impact parameters the excited nuclear matter streams out of the compressed participant zone in the direction of the pressure gradient resulting in directed transverse flow. This collective effect becomes more pronounced as the impact parameter increases in the columns on the right-hand side of the figure.

1.2 Radial Flow

Radial flow is isotropic collective expansion described by a self-similar velocity field, *i.e.,* a collective velocity field proportional to the radial distance $\mid \mathbf{r} \mid$ from the source center. As previously mentioned, this radial expansion has been suggested to result in increased curvature in the single-particle kinetic energy spectra, and enhanced values for $\langle E_t \rangle$. Experimentally the radial flow and Coulomb repulsion for particles emitted from the spherical source cannot be separately distinguished without isotopic resolution. Central events are selected to search for a radial flow signal because stopping power, compression, and equilibration are expected to be greatest for collisions at small impact parameters. In addition to selecting central collisions, reaction products should be measured at 90° the c.m. frame in order to suppress the contamination by spectator emission and directed flow effects. In Figure 1.5 the measured c.m. kinetic energy spectra for H and He isotopes emitted into polar angles $\theta_{\mathrm{c.m.}} = 90° \pm 15°$ from 1.0 GeV/nucleon Au + Au collisions are shown [Lisa95]. The solid lines are a simultaneous fit (excluding protons) for a thermally equilibrated, radially expanding source, characterized by a temperature and a radial flow velocity (as given by Equation 4.3). The dashed lines show a similar fit for a purely thermal source (no radial expansion). The fits which incorporate radial expansion clearly better describe the

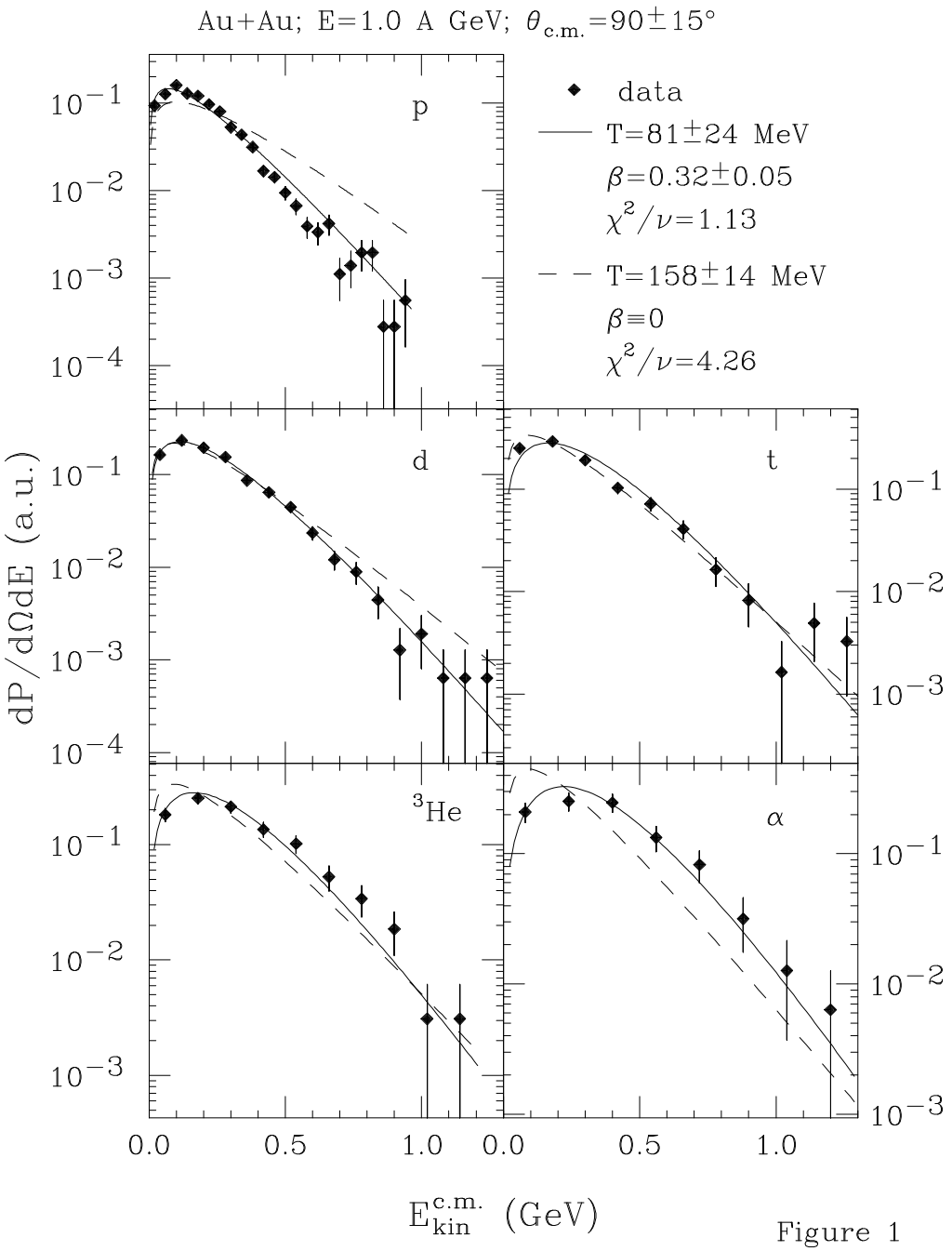

Figure 1.5: Measured c.m. kinetic energy spectra for light fragments emitted into polar angles $\theta_{c.m.} = 90° \pm 15°$ from 1.0 GeV/nucleon Au + Au collisions [Lisa95]. Fits to the spectra assuming a radially expanding thermal source (solid lines) and a purely thermal source (dashed lines) are also shown.

data than a purely thermal scenario, especially for the heavier fragments.

Theoretical evidence for the existence of radial flow from BUU model calculations is presented in Figure 1.6. Shown in this figure are calculated c.m. momentum distributions of different particles (solid symbols) at polar angle $\theta_{\rm c.m.} \approx 90°$ for central 800 MeV/nucleon La + La collisions [Dani95]. The increased curvature of these spectra is evident in the left panel, which become more concave as the mass of the fragment increases. (The open symbols and the fitted curves in the left panel are not considered here.) The right panel is the result of interchanging the fragment positions during evolution of the calculation for each of the different particle types while collisions were still frequent (particle momenta were not altered). This effectively destroys the correlation between particle spatial positions and their momenta that results in collective motion. Thus the spectra collapse to a single value of the inverse slope as would be the case for a purely thermal source (the straight parallel lines in the right panel serve to guide the eye). Comparison of the calculated spectra in the left panel reveals similar trends to the data presented in Figure 1.5 already for this lighter system at a lower incident energy. This lends further support to the concept of an isotropic radial expansion during the disassembly of these excited nuclear systems.

1.3 Directed Transverse Flow

As two nuclei collide, the pressure and density increase in the interaction region, *i.e.,* compression of the nuclear matter occurs in the participant volume. At nonzero impact parameters there is anisotropy in the pressure, resulting in a transverse flow of nuclear matter in the directions of lowest pressure. The directed or in-plane transverse momentum p_x is simply the projected component of the total transverse momentum of the particle of interest into the reaction plane. To quantify how this directed

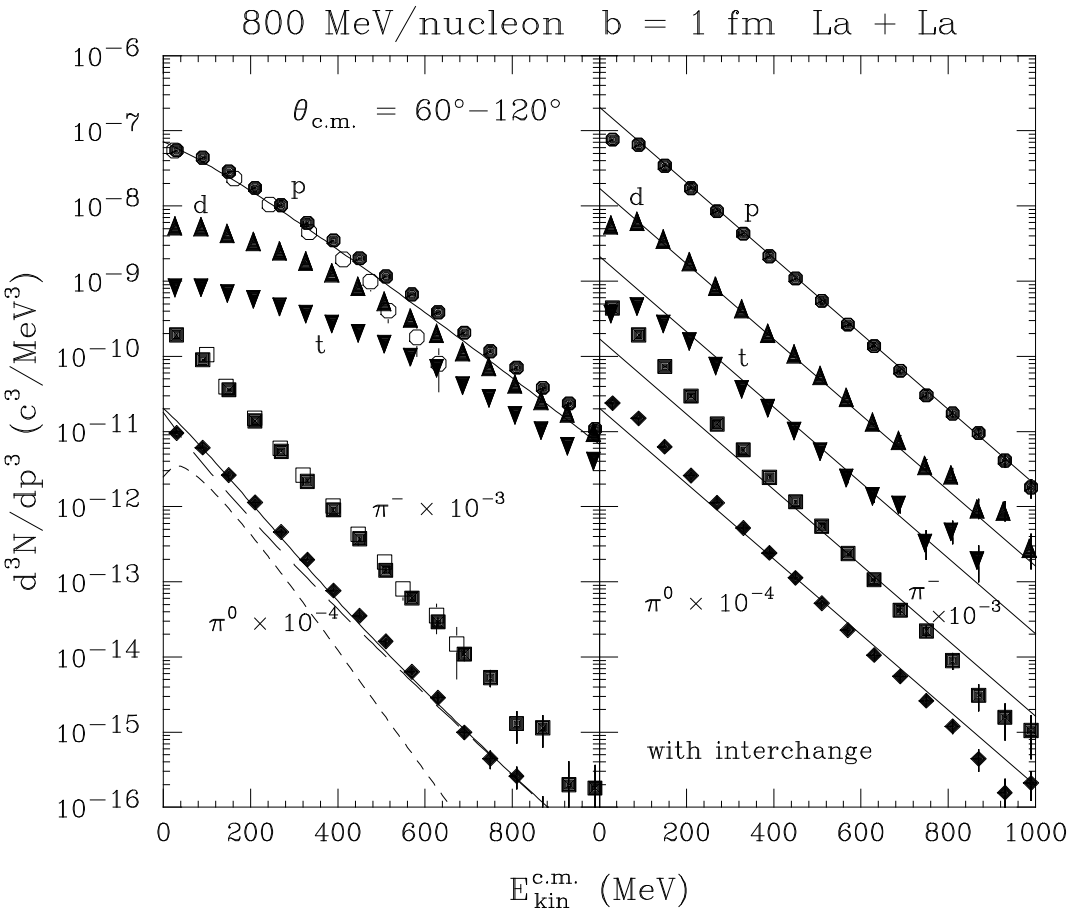

Figure 1.6: Momentum distributions of protons (circles), deuterons (triangles), helions (inverted triangles), negative (squares) and neutral (diamonds) pions from central 800 MeV/nucleon La + La collision within the c.m. polar angle range $60° \leq \theta_{c.m.} \leq 120°$ [Dani95]. The right (left) panel shows the results of BUU calculations with (without) particle positions interchanged during evolution.

transverse momentum varies along the direction of the beam axis, the mean transverse momentum in the reaction plane is plotted as a function of the rapidity [Dani85]. The rapidity y given by:

$$y = \frac{1}{2} \ln \left(\frac{1 + \beta_{\|}}{1 - \beta_{\|}} \right) \tag{1.1}$$

is a Galilean invariant function of the velocity parallel to the beam axis, which reduces to $\beta_{\|}$ if this velocity is small compared to the speed of light. From this plot the flow is extracted by fitting a straight line to the data over the midrapidity region. The slope of this line is defined as the directed transverse flow, which is a measure of the amount of collective momentum transfer in the collision. Collective transverse flow in the reaction plane disappears at an incident energy, the balance energy E_{bal} [Ogil90], where the attractive scattering dominant at energies around 10 MeV/nucleon balances the repulsive interactions dominant at energies around 400 MeV/nucleon.

A schematic representation of the directed transverse flow in the c.m. frame for three incident energies: (a) $E < E_{bal}$; (b) $E = E_{bal}$; and (c) $E > E_{bal}$ is shown in Figure 1.7 [Buta95]. In this diagram the projectile **P** moves from left to right along the z-axis, and collides with the target **T** moving in the opposite direction (the x-y plane is perpendicular to the beam direction). The central column is the projection of the linear momenta onto the reaction plane (the x-z plane), and these linear momenta projected onto the x-y plane are the transverse momenta. The left (right) column shows the transverse momenta for particles with c.m. rapidity $y < y_{c.m.}$ ($y > y_{c.m.}$). Focusing attention on the case for particles moving forward in the c.m. frame ($y > y_{c.m.}$) in the right column, we observe:

1. For $E < E_{bal}$ where the interaction is dominated by the attractive mean field, the particles are mainly scattered away from the projectile side of the reaction plane (to negative angles).

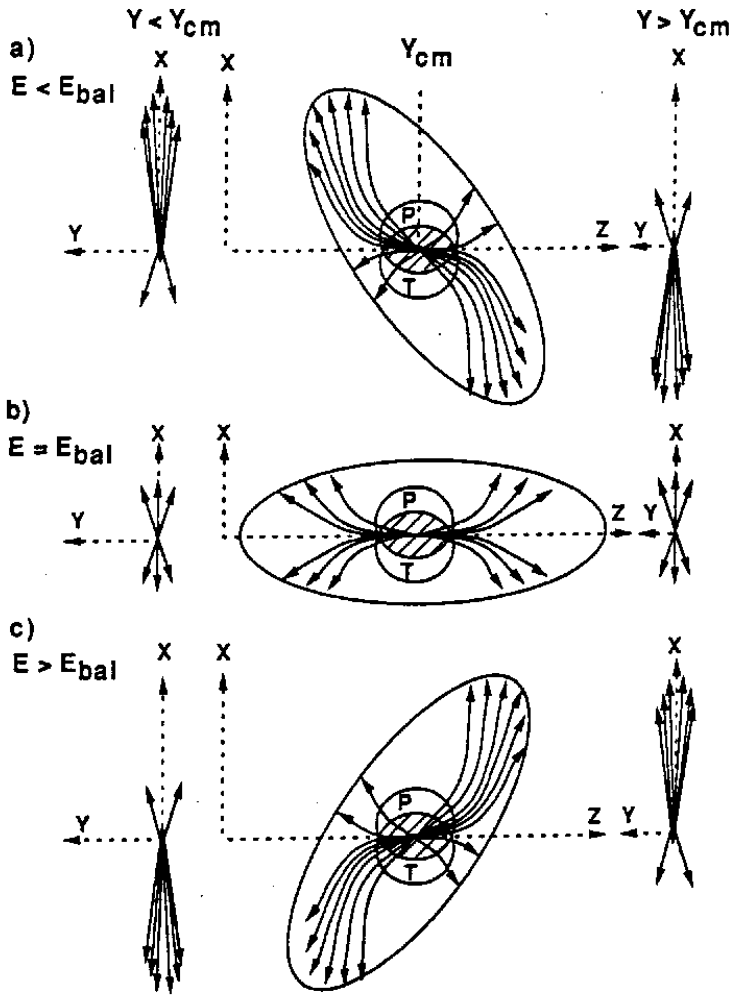

Figure 1.7: Schematic representation of the directed transverse flow in the c.m. frame for three incident energies: (a) $E < E_{bal}$; (b) $E = E_{bal}$; and (c) $E > E_{bal}$ [Buta95]. The central column is the projection of the linear momenta onto the reaction plane. The left (right) column is the transverse momenta for c.m. rapidity $y < y_{c.m.}$ ($y > y_{c.m.}$).

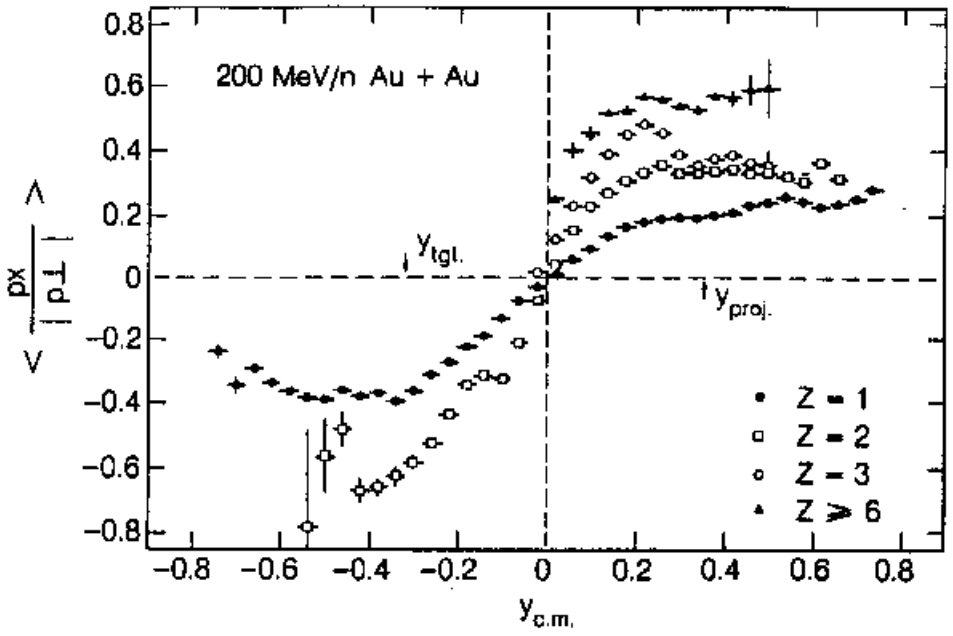

Figure 1.8: Fraction of the mean transverse momentum in the reaction plane versus the c.m. rapidity for semi-central Au + Au collisions at 200 MeV/nucleon [Doss87, Harr87]. Displayed are the values for $Z = 1$, 2, 3, and $Z \geq 6$.

2. For $E > E_{bal}$ where the interaction is dominated by the repulsive nucleon-nucleon scattering, the particles are mainly scattered toward the projectile side of the reaction plane (to positive angles).

3. For $E = E_{bal}$ these two effects balance, the particles are symmetrically deflected in the reaction plane, and the directed transverse flow vanishes.

The converse is true for particles moving backward in the c.m. frame ($y < y_{c.m.}$).

We now display the experimental results corresponding to Case (c) in Figure 1.7 from a transverse momentum analysis done by the group responsible for the first measurement of directed transverse flow. Figure 1.8 shows the fraction of the mean transverse momentum in the reaction plane versus the c.m. rapidity for various fragment types from semi-central Au + Au collisions at 200 MeV/nucleon [Doss87, Harr87]. The transverse momentum is reduced in this manner so that the data for the different

particle types can be displayed on the same scale. For the H and He isotopes the data exhibit the characteristic "S-shape" associated with directed collective transverse flow, demonstrating the dynamical momentum transfer on opposite sides of the reaction plane. The asymmetry for fragments with $Z = 3$ and $Z \geq 6$ is an artifact of detector acceptance produced by forward focusing effects in fixed target experiments. The directed transverse flow clearly increases as the fragment mass increases, because the flow energy is an increasingly larger fraction of the fragment energy while the thermal energy is less important as the fragment mass increases. This is under the assumption that the thermal energy was equally partitioned for the equilibrated system of nucleons and fragments at a fixed freezeout temperature. The mass dependence of fragment flow is additional experimental evidence that the disassembly mechanism resulting from heavy-ion collisions is not simply a thermal process.

There exists abundant theoretical evidence demonstrating directed transverse flow consistent with the scenario provided above. A beautiful example is presented in Figure 1.9 which shows predictions of BUU model [Bert87] calculations for different combinations of the EOS and nucleon-nucleon cross section σ_{nn}. The parameter sets in the calculations were: (1) soft EOS and $\sigma_{nn} = 41$ mb (solid circles and solid lines); (2) stiff EOS and $\sigma_{nn} = 41$ mb (open circles); (3) soft EOS and $\sigma_{nn} = 20$ mb (solid squares and dashed lines); and (4) stiff EOS and $\sigma_{nn} = 20$ mb (open squares). The mean transverse momenta are calculated for mass 40 projectiles and mass 40, 100, and 197 targets, impact parameters of 3, 5, 7 and 9 fm, and bombarding energies E = 60, 100, 200, and 400 MeV/nucleon. Focusing attention on the symmetric mass 40 system in the left-hand side panel, we find that at low incident energy the mean transverse momenta are negative at all impact parameters. This is consistent with negative scattering by the attractive mean field, because the two-body collisions are suppressed due to the Pauli exclusion principle. The mean transverse momentum

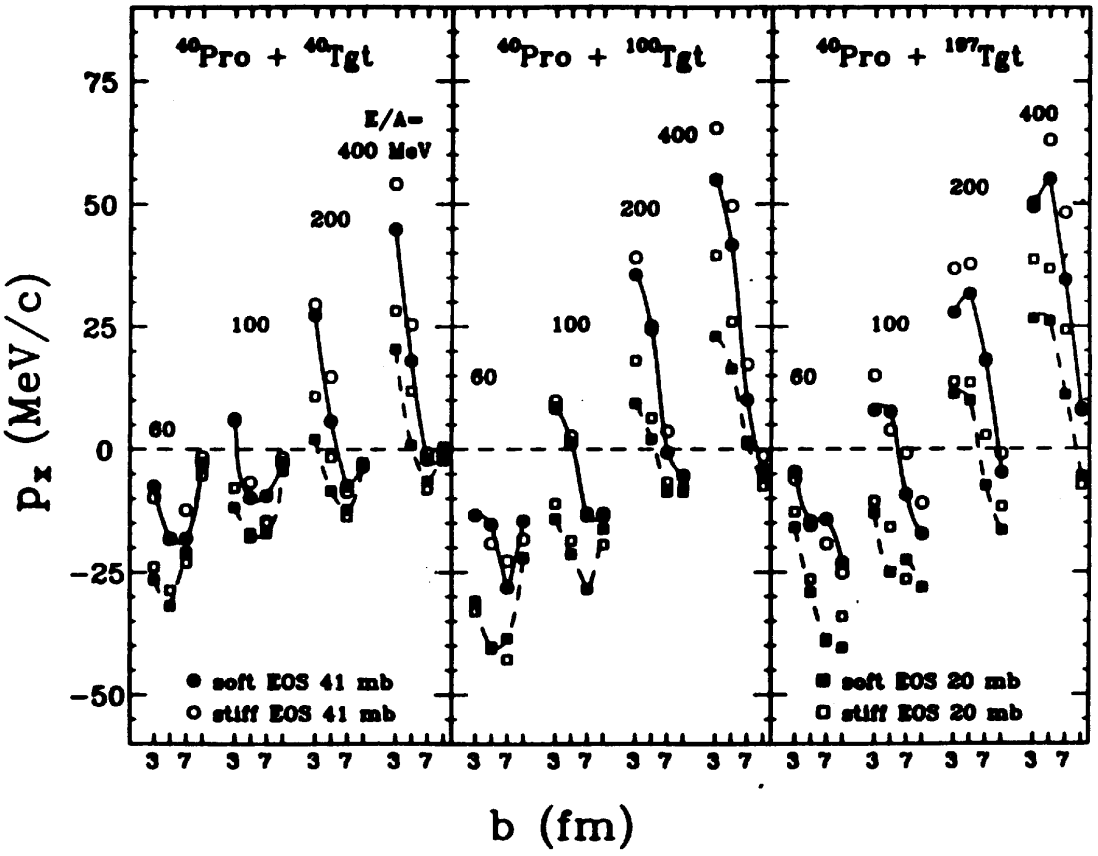

Figure 1.9: Mean transverse momenta calculated from BUU theory for mass 40 projectiles and mass 40, 100, and 197 targets, impact parameters of 3, 5, 7 and 9 fm, and bombarding energies E = 60, 100, 200, and 400 AMeV [Bert87]. Calculations are with: (1) soft EOS and σ_{nn} = 41 mb (solid circles and solid lines); (2) stiff EOS and σ_{nn} = 41 mb (open circles); (3) soft EOS and σ_{nn} = 20 mb (solid squares and dashed lines); and (4) stiff EOS and σ_{nn} = 20 mb (open squares).

monotonically increases with bombarding energy, which is particularly evident at small impact parameters where $\langle p_x \rangle$ changes sign and rapidly becomes positive for $E > 100$ MeV/nucleon. This flip in the sign of $\langle p_x \rangle$ occurs at the balance energy where the competing effects of the attractive mean field and the repulsive nucleon-nucleon scattering cancel, producing no net transverse momentum. Above the balance energy positive values for $\langle p_x \rangle$ result from kinetic pressure built up during the high density compression stage of the collision. At these energies repulsive two-body collisions are frequent, the mean field is lost, and positive scattering dominates. These trends are preserved for the other systems in the remaining panels of Figure 1.9. The importance of the role of the impact parameter in the determination of the disappearance of transverse flow is also apparent from this figure, because the sign flip is shown to occur at higher incident energies for events with larger impact parameters.

1.4 Thesis Structure

The following is a brief outline of the structure of this thesis:

Chapter 1: Introduction and background to collective flow in heavy-ion collisions.

Chapter 2: Experimental details of the MSU 4π Array.

Chapter 3: Event characterization with impact parameter, reaction plane, and temperature parameter.

Chapter 4: Radial flow from transverse energy production with comparison to BUU and WIX model calculations.

Chapter 5: Directed transverse flow and the balance energy from transverse momentum analysis with comparison to QMD model calculations.

Chapter 2

Experimental Details

2.1 Beams and Target

The data presented in this thesis were taken with the Michigan State University (MSU) 4π Array [West85] at the National Superconducting Cyclotron Laboratory (NSCL) using heavy-ion beams accelerated by the K1200 cyclotron. Prior to this experiment, the MSU 4π Array was upgraded with the High Rate Array (HRA). The MSU 4π Array has been recently used in various experiments as diverse in purpose as subthreshold pion production [Hann95], proton-proton correlation experiments [Hand95, Gaff95], and fusion-fission studies [Yee95, Gual95]. Other accomplishments with the MSU 4π Array include the first measurement of the balance energy [Krof91], the mass dependence of the disappearance of flow [West93], evidence for the liquid-gas phase transition [Li93, Li94], and systematic event shape analysis [Llop95b]. During the experiments, information from each collision which satisfied a minimum bias hardware trigger was digitized on an event-by-event basis, written to magnetic tape, and later analyzed off-line.

A target of 1.0 mg/cm^2 natural Sc (scandium) was bombarded with ^{40}Ar (argon) projectiles ranging in energy between 35 and 115 MeV/nucleon in 10 MeV/nucleon steps. For symmetric systems the experimental identification of specific collective

effects is less ambiguous, because then it can assumed that the projectile and target contribute equally to the participant (overlap) region. This produces a source that moves with the well-defined center-of-mass velocity regardless of impact parameter. We had already successfully run with the nearly symmetric entrance channel ^{40}Ar+^{45}Sc [Li93, Li94], but our improved acceptance would now allow better impact parameter selection. Scandium was also the closest naturally pure stable isotope for a mass forty target available.

We were originally approved to run at beam energies of 65, 75, 85, 95, 105, and 115 MeV/nucleon, because we had shown the balance energy to be 87±12 MeV/nucleon [West93] for central ^{40}Ar+^{45}Sc collisions. At the time the experiment was run, 115 MeV/nucleon was the highest energy $^{40}Ar^{16+}$ beam the K1200 cyclotron could produce. Beam intensities were approximately 100 electrical pA. With RF beam bursts approximately every 50 ns, these currents corresponded to only one or two ^{40}Ar ions in each burst, thus the possibility of multiple events in a single burst is quite small. In order to reduce tuning time for the beams, a primary ^{40}Ar beam was degraded in the A1200 to produce a series of several lower energy secondary ^{40}Ar beams without a significant loss of intensity. The following sections in this chapter describe in detail the MSU 4π Array, its various components and their acceptance, the methods used to calibrate them, and the data they produce.

2.2 Detectors

2.2.1 Geometry

The underlying geometry of the MSU 4π Array is a 32 faced truncated icosahedron, as shown in Figure 2.1, of which twenty faces are hexagons and twelve are pentagons. This geometric configuration allows close-packing of detector modules to

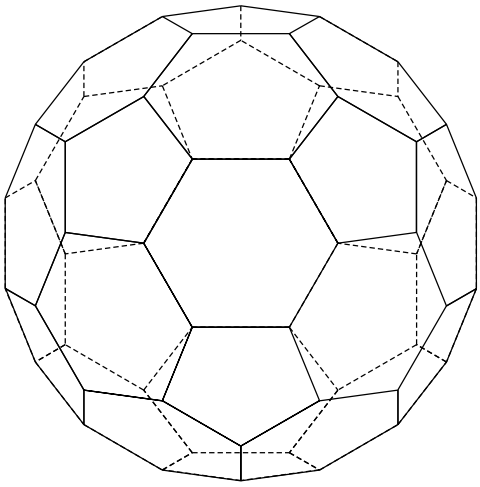

Figure 2.1: Basic geometry of the MSU 4π Array.

provide nearly full 4π steradian (sr) coverage in solid angle. Two of the pentagonal faces serve as the entrance and exit for the beam; all the remaining sites are filled by detector modules. Each hexagonal (pentagonal) module contains a subarray of six (five) close-packed fast/slow plastic detectors resulting in a total of 170 phoswiches [Wilk52] in the main ball.

The detectors of the main ball cover laboratory polar angles $18° \lesssim \theta_{lab} \lesssim 162°$. Table A.1 in Appendix A lists the mean angular position for each ball fast/slow counter. The individual phoswich detectors in the main ball are truncated triangular pyramids which subdivide either hexagons (60°, 60°, 60°) or pentagons (72°, 54°, 54°). The solid angle subtended by each of the ball phoswiches is listed in Table 2.1. The

Table 2.1: Solid angle subtended by the ball phoswiches.

Module Type	Ideal (msr)	True (msr)
Hexagon	(6×) 75.2	66.0
Pentagon	(5×) 59.0	49.9

true solid angles are slightly smaller than those predicted from ideal geometry due to dead spaces between the modules.

Prior to this thesis experiment, the MSU 4π Array was upgraded to include a newly designed forward array called the High Rate Array (HRA) [Pak93]. The HRA is a close-packed pentagonal configuration of 45 phoswich detectors spanning polar angles $3° \lesssim \theta_{lab} \lesssim 18°$. This array has acceptable granularity, minimum dead area, and high data rate capability (HRA detector count rates $\approx$ 25,000 events/sec). The HRA consists of three pentagonal rings of 10, 15, and 20 fast/slow plastic counters as shown schematically in Figure 2.2. A 45 detector design was chosen so that no additional electronics would be necessary, because the HRA replaced a forward array with this many detectors. The only investment was in scintillator plastic and the mechanical support structure. Machining was done at the NSCL, and all additional fabrication was carried out by the 4π Group. The installation of the completed HRA occurred on schedule in December of 1993.

A major constraint in the design of the HRA was that it subtend the solid angle between the Maryland Forward Array (MFA) and the main ball of the MSU 4π Array. In this experiment, the MFA was a close-packed annular configuration of 16 phoswich detectors spanning polar angles $1.5° \lesssim \theta_{lab} \lesssim 3°$. A schematic view of the MFA as it attaches to the frame of the HRA is shown in Figure 2.3. A cross-sectional view of how the HRA mounts forward of the MSU 4π Array between the modules of the main ball and the MFA is schematically shown in Figure 2.4. The HRA subtends all solid angle between the MFA and the modules of the main ball resulting in over 90% geometric efficiency for the entire MSU 4π Array.

Simulated events were run through a software replica of the HRA to determine the positions and sizes of the 45 HRA elements that provide the optimal granularity for

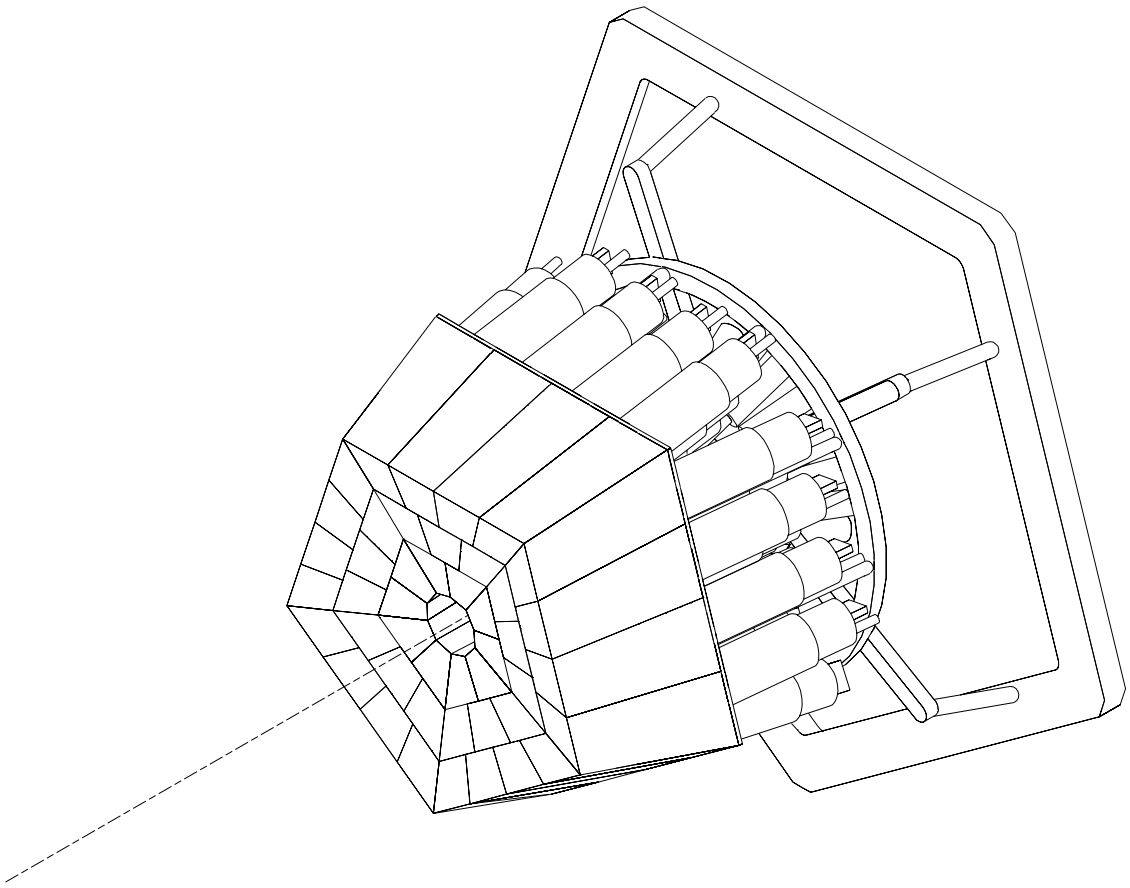

Figure 2.2: The High Rate Array (HRA).

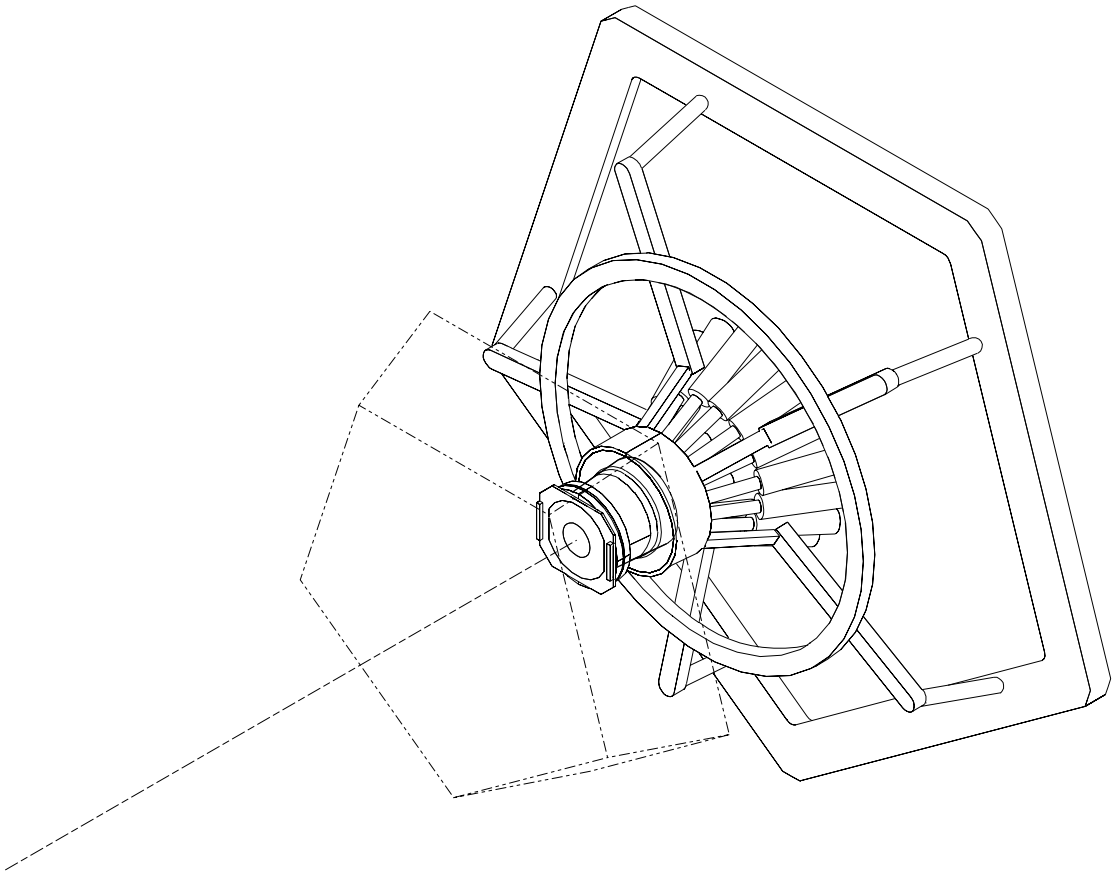

Figure 2.3: The Maryland Forward Array (MFA) as it attaches onto the frame of the HRA.

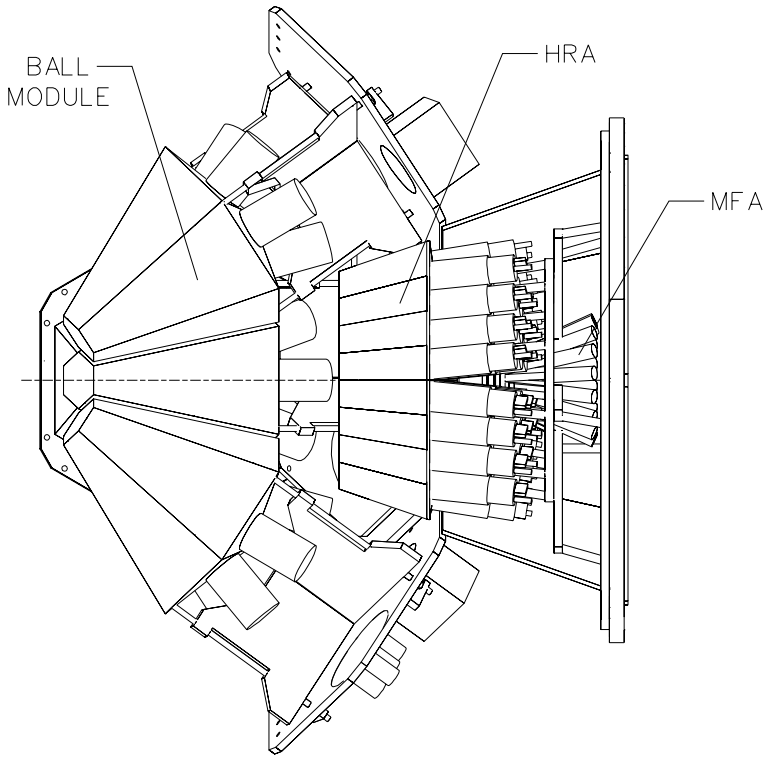

Figure 2.4: Schematic view of how the HRA mounts in the MSU 4π Array between the MFA and the modules in the main ball.

these generated events, and minimize the probability for double hits in each detector. Three designs were considered, each having a different combination of the number of detectors in each of the pentagonal rings: DESIGN(1) 20-15-10; DESIGN(2) 15-15-15; and DESIGN(3) 10-15-20 (counting from the ring closest to the beam axis). At each incident energy, events were generated with specific multiplicities in a projectile-like frame (upper curves) and in an ^{40}Ar+^{45}Sc center-of-mass frame (lower curves), as shown in Figure 2.5 [Pak92]. The particles were distributed isotropically in each frame with thermal (T = 10 MeV) kinetic energy distributions. The vertical axis is the probability that two or more particles hit the same HRA element. The results indicate that the design that overall is least susceptible to double hits is DESIGN(3), and was therefore considered the most suitable for the proposed upgrade.

The numbering scheme for the detectors in the HRA is shown in Figure 2.6. The

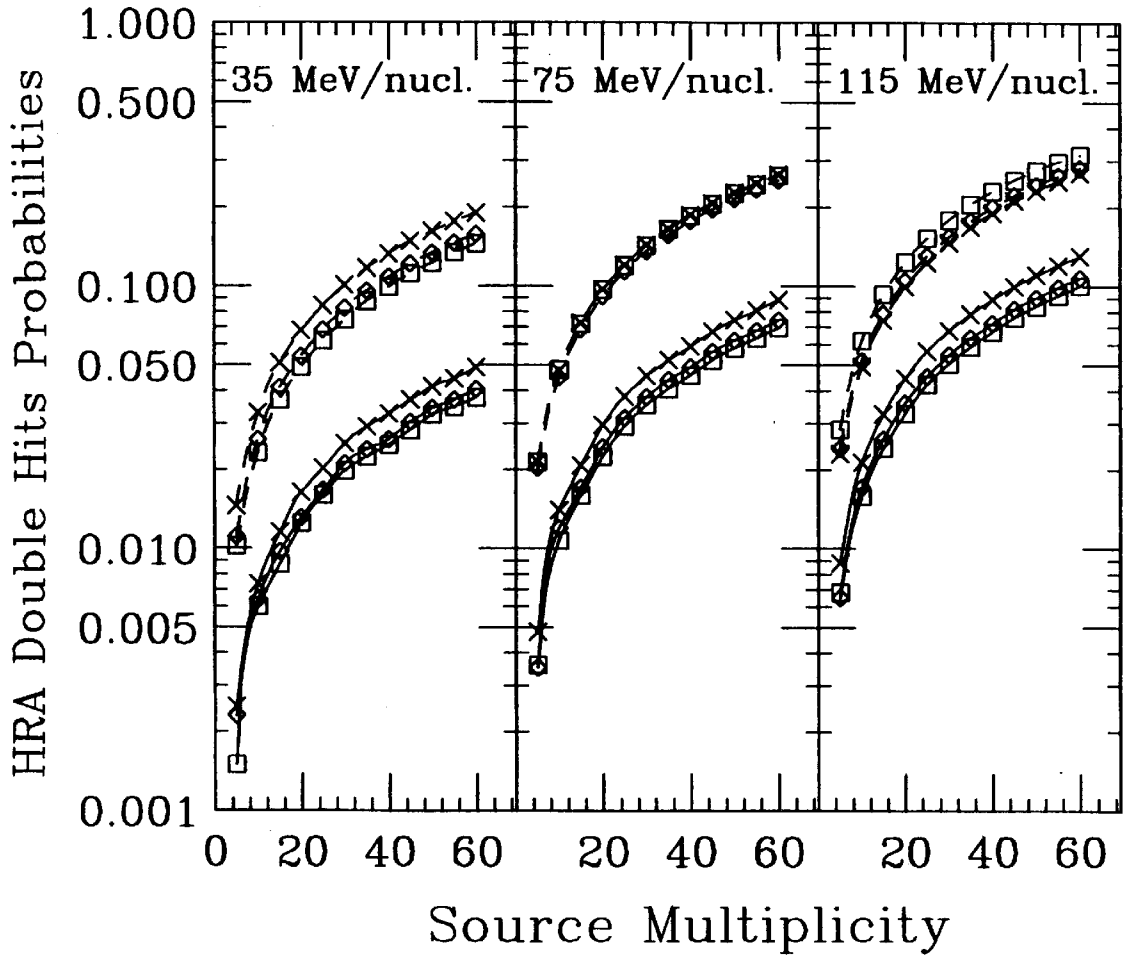

Figure 2.5: Simulation results for double hits probabilities in various proposed designs for the HRA. At each incident energy the upper curves are for projectile source emission, and the lower curves are emission at midrapidity from ^{40}Ar+^{45}Sc reactions. Crosses are for DESIGN(1); diamonds are for DESIGN(2); and squares are for DESIGN(3) as described in the text.

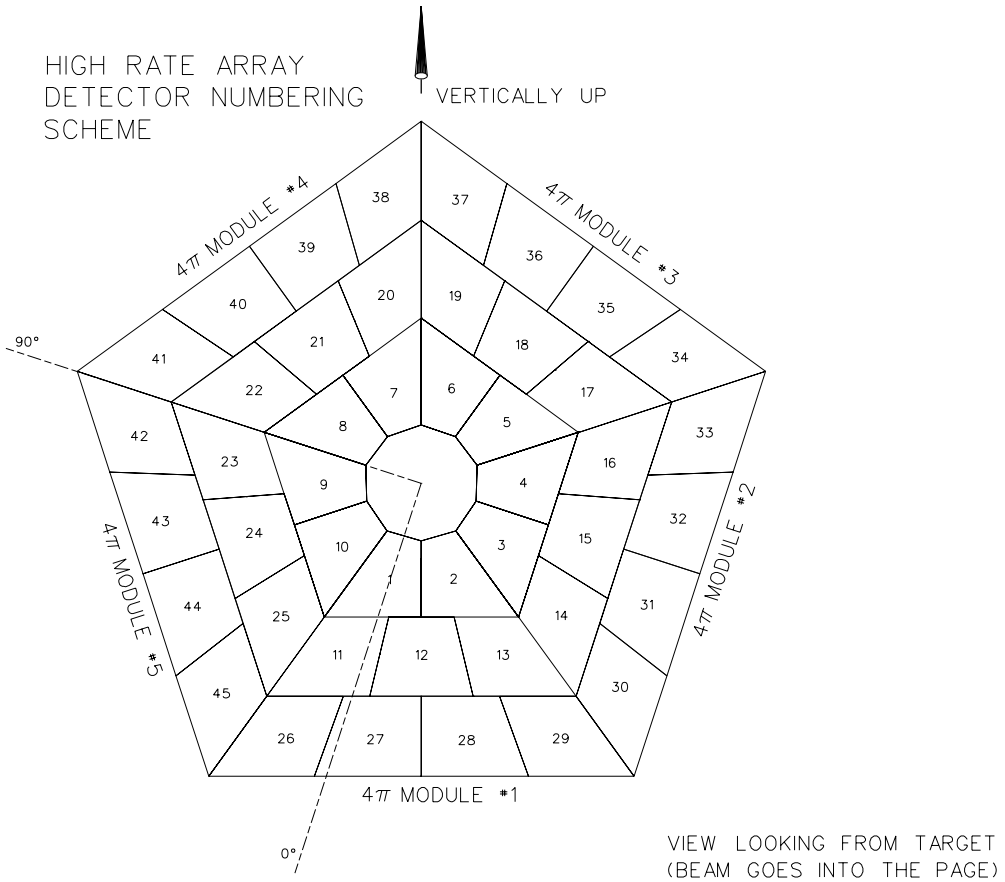

Figure 2.6: The numbering scheme for the phoswiches in the HRA.

array is composed of five wedges of nine detectors. The mean angular position for each HRA phoswich is given in Table A.2 in Appendix A. The solid angle subtended by each HRA detector is given in Table 2.2 below. The HRA is positioned as close

Table 2.2: Solid angle subtended by the HRA phoswiches.

HRA Detector Number	Solid Angle (msr each)
1, 2, 3, 4, 5, 6, 7, 8, 9, 10	5.11
12, 15, 18, 21, 24	6.27
11, 13, 14, 16, 17, 19, 20, 22, 23, 25	6.18
27, 28, 31, 32, 35, 36, 39, 40, 43, 44	6.88
26, 29, 30, 33, 34, 37, 38, 41, 42, 45	6.65

to the target as would allow a 5 cm diameter photomultiplier tube (PMT) to be optically coupled onto the back of each detector, which is $\approx$ 71 cm to the front face of the array.

2.2.2 Specifications

Figure 2.7 is a schematic diagram showing the components of a hexagonal module of the MSU 4π Array. The phoswiches [Wilk52] consist of a thin layer of fast plastic scintillator, followed by a thick block of slow plastic scintillator, which is optically coupled to a PMT. These detectors will stop all but the most energetic light ions. Mounted in front of each phoswich subarray is a gas ionization chamber known as a Bragg Curve Counter (BCC) [Gruh82], which primarily measures intermediate mass fragments (IMFs), *i.e.,* particles with charge $3 \leq Z \lesssim 20$. The hexagonal anodes of the five most forward BCCs are segmented, resulting in a total of 55 separate detectors of this type. Mounted in front of each BCC is another gas detector called a low pressure multi-wire proportional counter (MWPC) [Bres82] for detection of heavy slow fragments, *e.g.,* fission fragments. The 30 MWPCs were not in operation during

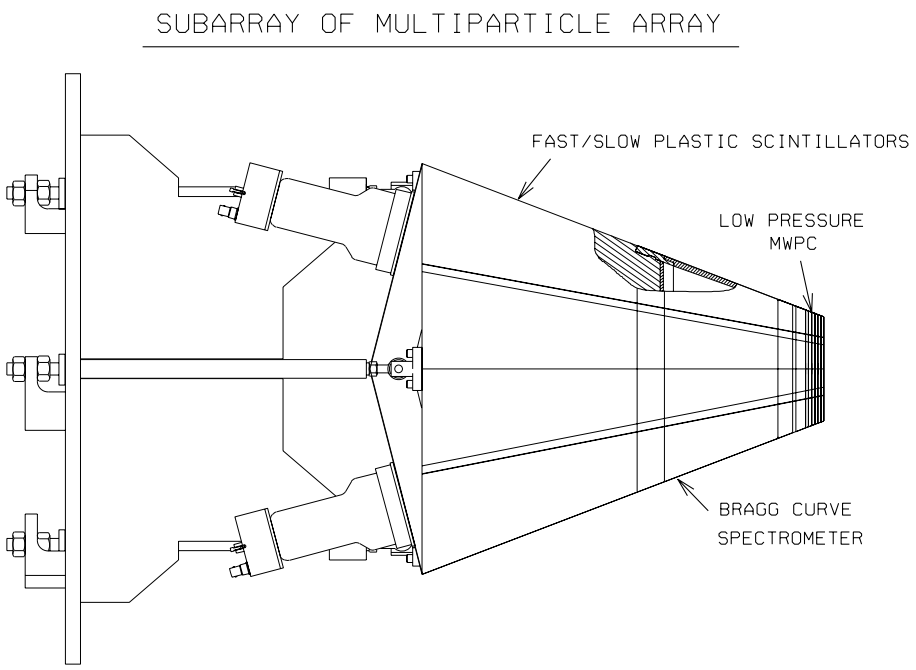

Figure 2.7: Schematic diagram showing the components of a hexagonal MSU 4π module.

this experiment because ^{40}Ar+^{45}Sc is a relatively light non-fissile system.

When a charged particle impinges on the scintillator elements of the phoswiches, light is produced, which is collected by the PMT and turned into a current pulse. The fast and slow plastic have different decay times [Bicr85] as shown in Table 2.3, so that their individual contributions to this current pulse can be electronically separated. This is called the ΔE-E method because the fast component of this signal is

Table 2.3: Phoswich scintillator specifications.

Element	Plastic	Thickness (mm)	Rise time (ns)	Decay time (ns)
Ball Fast ΔE	BC412	3.2	1.0	3.3
Ball Slow E	BC444	250	20	180
HRA Fast ΔE	NE110	1.7	1.1	3.3
HRA Slow E	NE115	194	8.0	320

a measure of the energy loss in transmission through the thin fast plastic, while the

slow component is a measure of the total energy deposited in the thick slow plastic. The current pulse from a phoswich detector, and the ΔE and E gates to separate the fast and slow components of this signal are schematically shown in Figure 2.8.

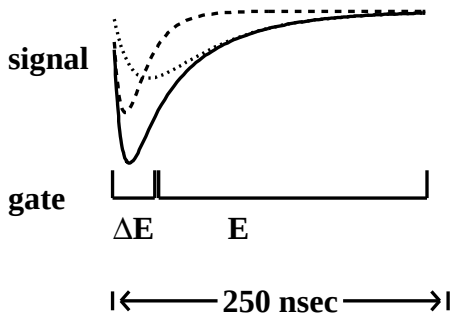

Figure 2.8: Diagram of the phoswich signal and gates.

The phoswich detectors were painted with an epoxy based paint pigmented with TiO_2. Only this opaque epoxy layer and a thin reflective foil (to insure no crosstalk) separate adjacent detectors, effectively minimizing the dead area. A 4.5 kÅ-thick (0.12 mg/cm^2) aluminum layer was evaporated onto the front face of the HRA detectors to minimize light leaks without compromising the kinetic energy thresholds. The 25 kÅ-thick Al layer on the front face of the main ball phoswich subarray serves as the anode for the BCC.

With the HRA we obtained Z resolution up to the charge of the ^{40}Ar projectile, and mass resolution for the hydrogen isotopes. In Table 2.4 we give the punch-in energies in MeV for various particle types entering the slow plastic of an HRA phoswich, as calculated using the energy loss routine DONNA. The thickness (given in Table 2.3), and density (ρ = 1.032 g/cm^3) of the fast plastic determines the low energy threshold for well identified particles. The Al layer on the front face the HRA is negligible in the determination of these energies.

Table 2.4: Low energy thresholds for the HRA.

Particle Type	Punch-in Energy (MeV)	Particle Type	Punch-in Energy (MeV)	Particle Type	Punch-in Energy (MeV)
p	13	C	269	Al	877
d	17	N	341	Si	962
t	20	O	419	P	1079
He	50	F	515	S	1170
Li	99	Ne	591	Cl	1294
Be	152	Na	687	Ar	1455
B	212	Mg	767		

Figure 2.9 displays a schematic cross-sectional view showing the components of a BCC. For this experiment, the BCCs were operated in ion chamber mode with a pressure of 125 Torr of C_2F_6 gas (cathode voltage = -500 V and anode voltage = +150 V). The BCCs were used to measure the energy loss of charged particles that stopped in the fast plastic scintillator of the main ball. This is similar to the method used in the phoswiches, but with significantly lower kinetic energy thresholds (especially for heavier mass fragments). In Table 2.5 we give the punch-in energies in MeV for the various particle types entering the fast plastic of a main ball phoswich in this experiment. These values were calculated using the DONNA code, and include losses in the MWPC (protons, deuterons, and tritons are not detected in the BCCs).

Table 2.5: Low energy thresholds for the ball telescopes.

Particle Type	Punch-in Energy (MeV)	Particle Type	Punch-in Energy (MeV)	Particle Type	Punch-in Energy (MeV)
He	12	N	74	Mg	163
Li	23	O	91	Al	184
Be	34	F	108	Si	202
B	46	Ne	123	P	224
C	59	Na	146	S	242

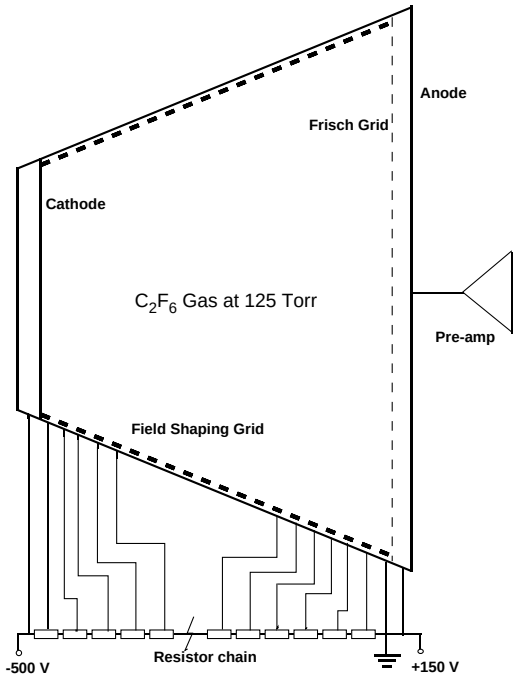

Figure 2.9: A schematic cross-sectional view of a MSU 4π Bragg Curve Counter (BCC).

Physical characteristics, operational principles, and calibration of the BCCs in the MSU 4π Array are well detailed elsewhere [Cebr91].

2.3 Electronics

The PMT, PMT-base, and voltage divider card for each phoswich detector are contained within the vacuum chamber of the MSU 4π Array. All amplification of the light produced by the fast/slow scintillator plastic takes place in the PMT. Typical voltages on the PMTs range between +1300 and +1900 V. Figure 2.10 is a schematic diagram of the electronics layout for one of the phoswich detectors in the MSU 4π Array [VMol95]. Each detector receives its bias and transmits its signal over a single SHV cable (the MFA has separate signal and voltage cables). These cables are connected to splitter box modules in the electronics racks where the phoswich signal is passively separated from the high voltage into its fast, slow, and timing signals.

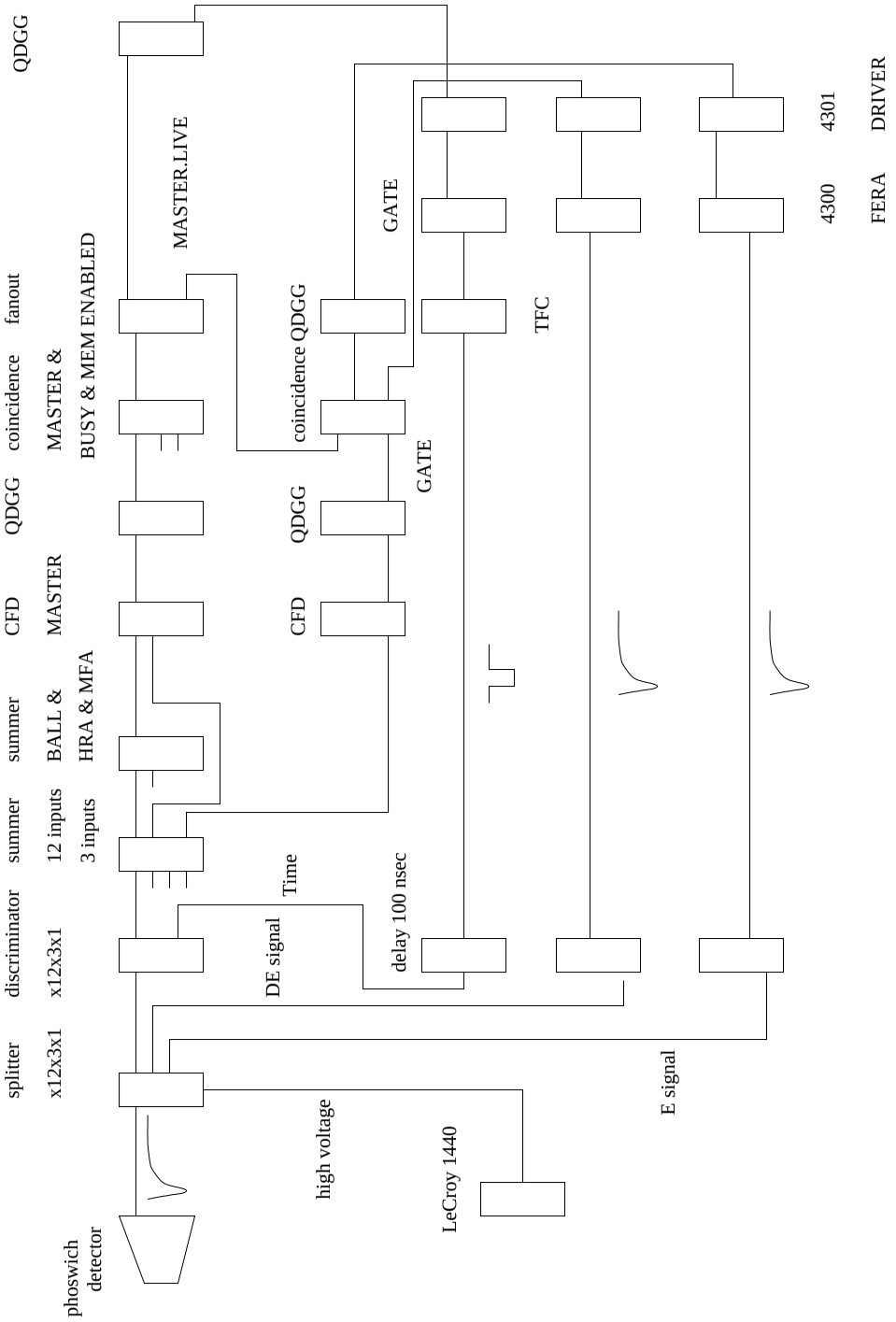

Figure 2.10: A schematic diagram of the electronics layout for the MSU 4π Array [VMol95].

There are twelve banks of signals for the main ball, three banks for the HRA, and one bank for the MFA.

The triggering system allows on-line selection of events on the basis of particle multiplicity for storage to magnetic tape. The trigger condition can be on the number of hits in the main ball, the HRA, the MFA, or the entire detector system (the BCCs are not included in the trigger stream). The trigger stream for the MSU 4π Array starts with the analog timing signals out of the splitter boxes. These signals are sent to leading edge discriminators with thresholds set to fire above noise. These discriminators provide a sum output whose amplitude is proportional to the number channels above threshold in that bank. The twelve sum signals for the main ball and the three sum signals for the HRA are then separately combined in an analog summer box. The total sum of the main ball, HRA, and MFA is further combined to provide a sum signal proportional to the total hit multiplicity in the entire detector array. The four corresponding sum signals are passed into a constant fraction discriminator (CFD) which can be programmed to select a multiplicity greater than or equal to a given value for any of the four inputs (Ball, HRA, MFA, or total system). The output of this octal CFD becomes the master trigger (QDGG represents delayed gate generation in Figure 2.10).

For events that satisfy the specified trigger, the availability of the 4π transputer based data acquisition (DAQ) system is checked. A Master.Live signal is created if the computer is not busy, which commands the DAQ system to initiate an event. Gates are generated via a second octal CFD which indicates at least one signal present in the main ball, HRA, or MFA (and allows separate timing for these arrays). Coincidence between these "singles" and Master.Live, to create Ball.Live, HRA.Live, or MFA.Live, insures gate generation only for acceptable events when the DAQ is free. For these events, all FERA charge-to-digital converters (QDCs) with signals in their gates above

a set pedestal (effective digital threshold) are read-out. The integrated signals above threshold in the BCC gates of the Silena ADCs are also read-out at this time.

In general, a HRA or MFA multiplicity trigger will enrich the data sample with peripheral events due to the forward focusing of particles in fixed target experiments, while a main ball trigger will select more central events in which particles are emitted at larger polar angles with respect to the beam axis. Data in this thesis were taken with a minimum bias trigger requiring at least one hit in the HRA (HRA-1 data), and a more central trigger for which two hits in the main ball (Ball-2 data) were necessary. The radial flow analysis in Chapter 4 was performed with the Ball-2 data because the radial flow signal is enhanced for central collisions. The transverse flow analysis in Chapter 5 was performed with the Ball-2 data for the purpose of comparison to our previous results [West93].

2.4 Raw Data

When the integrated signals from the thin fast plastic are plotted versus the corresponding signals from the thick slow plastic, particles with different charges and masses fall into different bands in the resulting ΔE-E spectrum. A typical example of a raw two-dimensional (2-D) spectrum produced by a HRA phoswich is shown in Figure 2.11. The data shown are a compilation of samples for ^{40}Ar+^{45}Sc reactions at beam energies ranging between 35 and 115 MeV/nucleon in 10 MeV/nucleon steps for a detector at polar angle $\theta_{lab} \approx 5.4°$. Clearly there is charge resolution up to $Z = 17$; (this spectrum is displayed in 256 channel resolution, but the data were actually recorded in 2048 channel resolution). To demonstrate there is also mass resolution of the hydrogen isotopes for the HRA phoswiches the lower left corner of this spectrum is expanded as shown in Figure 2.12. The effect of the DAQ real-time filter,

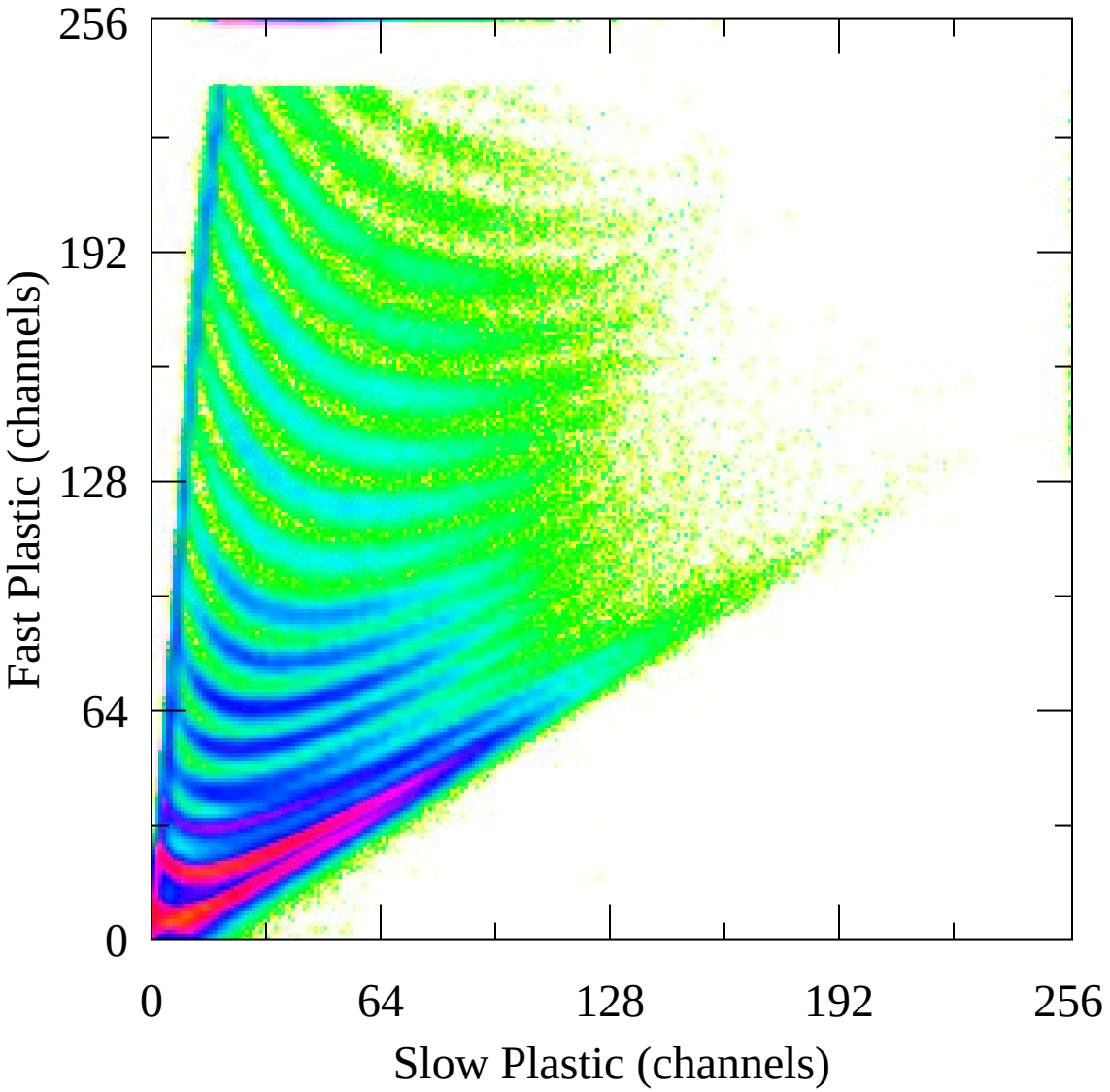

Figure 2.11: A two-dimensional histogram of the integrated signal in the fast (ΔE) QDC gate versus the integrated signal in slow (E) QDC gate. The data are ^{40}Ar+^{45}Sc reactions at beam energies ranging between 35 and 115 MeV/nucleon for a HRA detector at polar angle $\theta_{lab} \approx 5.4°$.

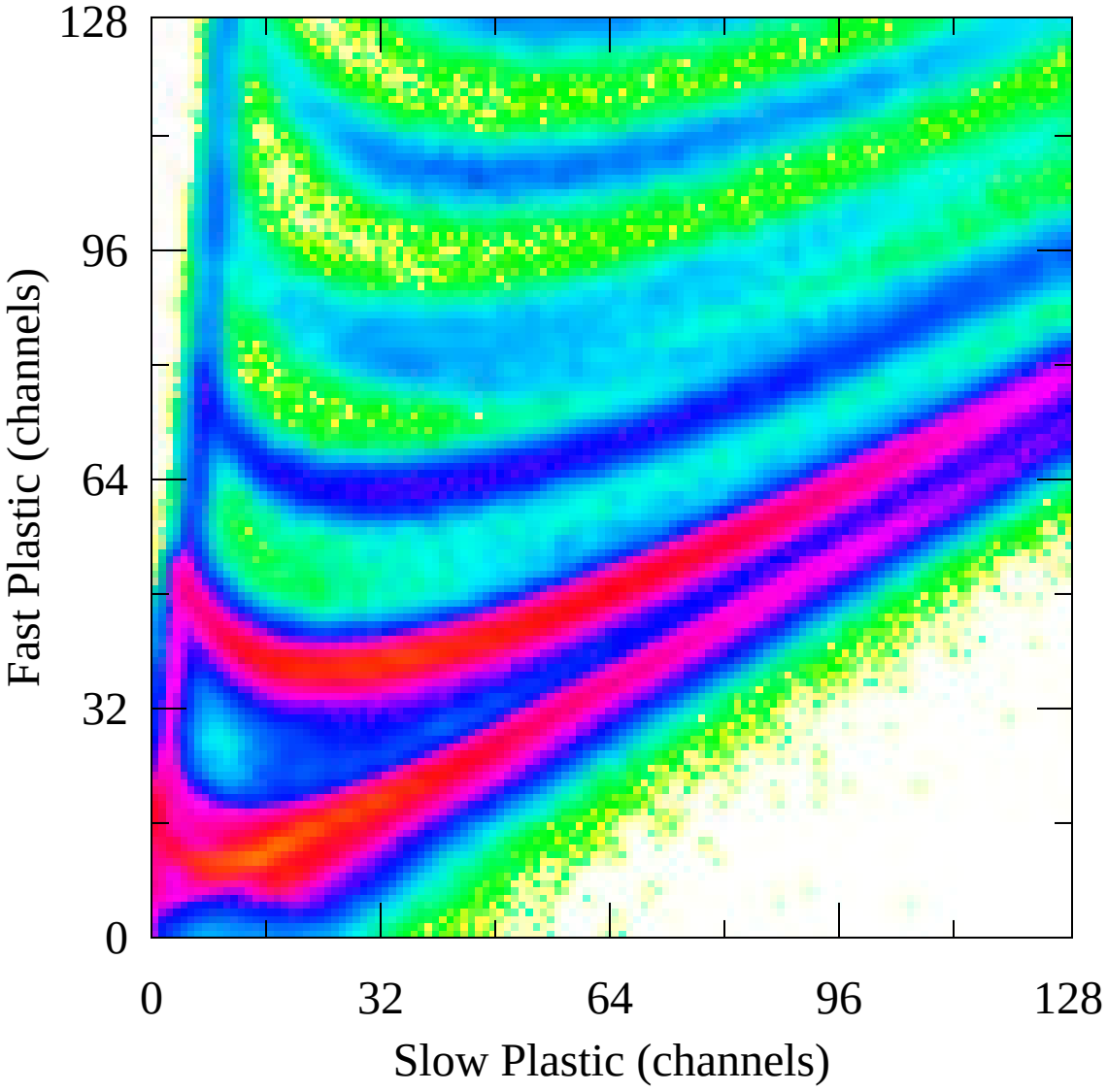

Figure 2.12: Lower left corner of Figure 2.11 expanded to demonstrate mass resolution for the hydrogen isotopes.

which greatly reduced the background noise by discarding hits without a valid time, is apparent from the hollowed-out corner below the protons. The spectra presented also demonstrate the stability of the HRA phoswiches against drifts in gain since these data were collected over a period of about a week. The remaining phoswiches in the HRA and main ball show a similar response, with progressively fewer bands in the spectrum as the polar angle increases, due to the forward focusing of particles in fixed target experiments.

Features common to all these raw 2-D spectra are explained in the following paragraph. The strong band close to the vertical axis, the "punch-in" line, is caused by particles with insufficient energy to punch through the fast ΔE plastic layer. In this case, no energy is deposited in the slow stopping plastic, but these points do not lie exactly on the vertical axis because the decaying fast signal leaks into the E gate (see Figure 2.8). Particles which leave little or no signal in the ΔE layer but leave a large signal in the slow plastic such as cosmic ray muons, neutrons, or gamma rays, populate the "neutral" line. This band near the horizontal axis results when the ΔE gate picks up some of the rising slow E signal even though these particles had no fast signal. The intersection point of these two lines corresponds to zero energy for all particles, and thus represents an electronic offset in the QDCs. As the energy of the fragments striking the phoswich is increased from zero, these particles appear higher and higher in the punch-in line until they have enough energy to punch into the slow plastic, emerging along the different bands in the spectrum.

The BCCs were operated in ion chamber mode so that only charged particles that stopped in the fast plastic of the phoswich directly behind them were well identified (thus there are effectively 170 BCC-fast plastic telescopes). When the integrated signals from the BCC are plotted versus those corresponding to the fast plastic scintillator, particles with different charges again fall into different bands in the resulting

spectrum, similar to the ΔE-E method for the phoswiches. A typical example of a raw 2-D spectrum produced in this manner is shown in Figure 2.13. The data shown are a compilation of samples for ^{40}Ar+^{45}Sc reactions at beam energies ranging between 45 and 115 MeV/nucleon in 10 MeV/nucleon steps for a detector at polar angle $\theta_{lab} \approx 32°$. There is charge resolution for $2 \leq Z \leq 10$ and mass resolution for $Z = 4$ for this detector telescope (this spectrum is displayed in 256 channel resolution, but the data were actually recorded in 2048 channel resolution in the fast plastic and 4096 channel resolution in the BCC). Fragments just punching into the fast plastic are found along the vertical axis. The raw 2-D BCC vs fast plastic spectra do not have a punch-in line because there is no overlap between the two different signals from the separate detector components gated and integrated to produce them. Also apparent in the spectrum shown in Figure 2.13 are the charged particles that begin to punch into the slow plastic of the phoswich, and consequently deposit less energy than if they were completely stopped in the fast plastic.

2.5 Data Calibration and Reduction

The large number of detectors in the MSU 4π Array necessitated development of a method [Cebr92] to minimize the amount of time required to calibrate each detector. A similar gain matching procedure, briefly outlined below, was followed using the HRA ΔE-E, the main ball ΔE-E, and the BCC-fast plastic spectra. For each spectral type this process involves creating a single calibrated template, which is then used to match all of the raw 2-D spectra. There are two main components to each of these templates: the gate lines and the response function.

The gate lines for the phoswiches are created by directly drawing them over a typical raw 2-D spectrum using a mouse driven graphics program called PIDMAKER.

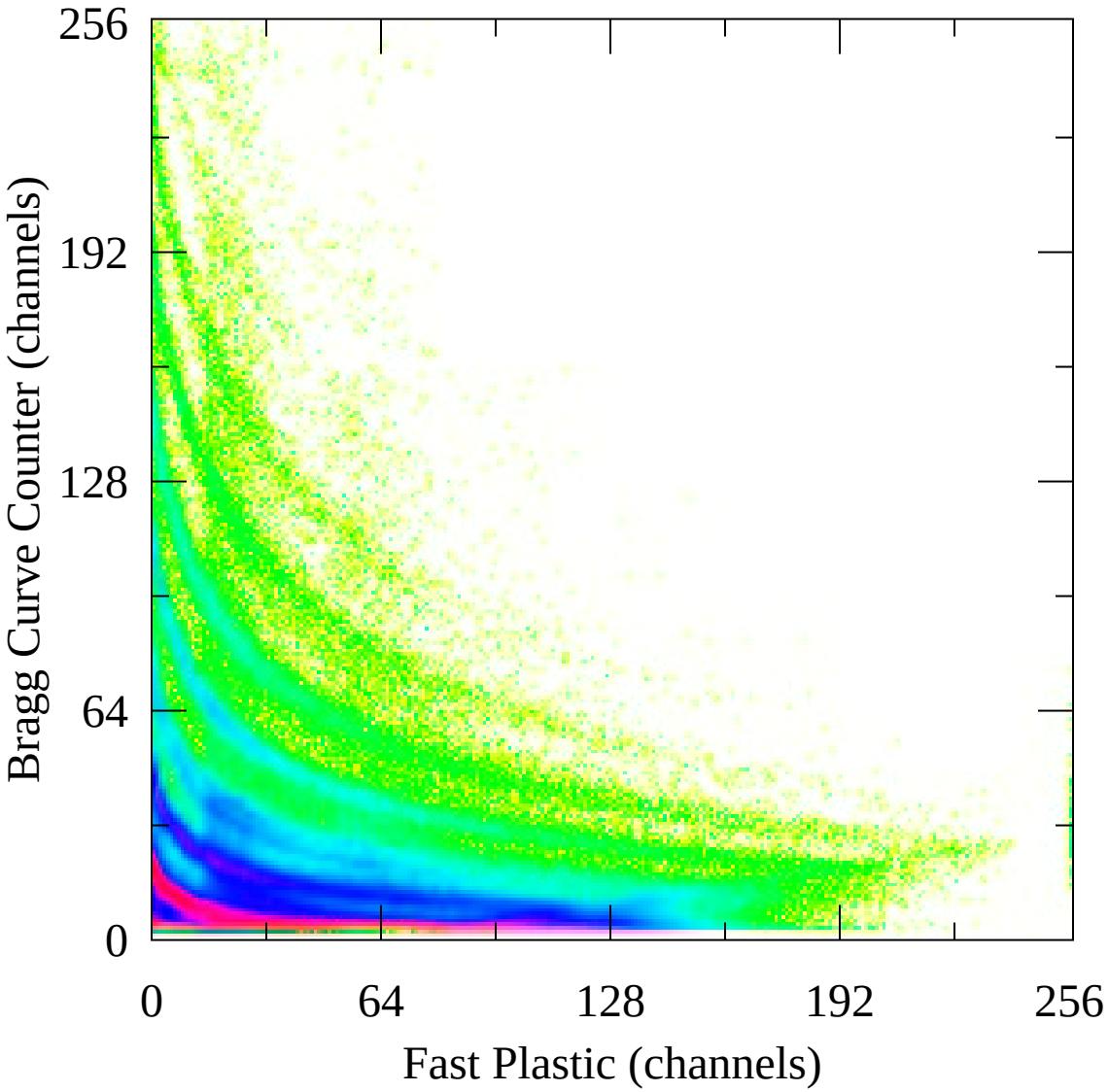

Figure 2.13: A two-dimensional histogram of the integrated signal in the BCC gate versus the integrated signal in fast plastic QDC gate. The data are ^{40}Ar+^{45}Sc reactions at beam energies ranging between 45 and 115 MeV/nucleon for a main ball detector telescope at polar angle $\theta_{lab} \approx 32°$.

Before this is done, the spectrum is transformed such that the punch-in line and neutral line lie exactly on the vertical and horizontal axes. This is done using the following mapping algorithm [Cebr92]:

$$\begin{aligned} Ch_{fast} &= G_{\Delta L} \times [(\Delta L - Y_0) - (L - X_0)M_n] \\ Ch_{slow} &= G_L \times [(L - X_0) - (\Delta L - Y_0)/M_p], \end{aligned} \tag{2.1}$$

where ΔL and L are the fast and slow channel numbers recorded in the QDCs during the experiment, M_n and M_p are the slopes of the neutral and punch-in lines, X_0 and Y_0 are the coordinates of the intersection point of the neutral and punch-in lines, and $G_{\Delta L}$ and G_L are multiplicative gain factors. The quantities Ch_{fast} and Ch_{slow} are the transformed channel numbers, which are proportional to the light produced in the fast and slow scintillator. The gate lines are used to produce particle identification (PID) lookup tables, which convert the transformed channel numbers into the correct mass number A and charge Z for each particle. Isotopic resolution is only obtained for $Z = 1$, and all other fragments are assigned a mass number corresponding to the most abundant isotope.

The form of the response functions, as determined from a previous calibration experiment [Cebr92], are given by:

$$\begin{aligned} Ch_{fast} &= aE_{fast}^{\alpha} - b \\ Ch_{slow} &= c\left(\frac{E_{slow}^{\beta}}{A^{\gamma}Z^{\delta}}\right). \end{aligned} \tag{2.2}$$

These equations convert the transformed fast and slow channel numbers into the energy lost in the corresponding plastic for a fragment of mass number A and charge Z. The exponential parameters α, β, γ, and δ, and arbitrary constants a, b, and c are determined by simultaneously fitting the curves following this functional form to the bands in the same representative spectrum used to create the gate lines. The final

step is to determine the incident energies for the particles based on their energy loss. With output from the energy loss routine DONNA, the response functions are used in PIDMAKER to generate MeV lookup tables which directly convert the transformed channel number into incident kinetic energy. Thus, when a raw 2-D spectrum is matched to the gate line template for particle identification, the transformed channel numbers are also assigned the correct incident kinetic energies. In this manner all phoswich spectra are gain matched to fit these gate line templates, using another set of programs with a graphical interface called the DALI package [Laur93]. The resulting six mapping parameters (M_n, M_p, X_0, Y_0, $G_{\Delta L}$, and G_L) for each phoswich detector are written to disk. The estimated error in the resulting energy calibration of the gain matched detectors is less than 10%.

The calibration of the BCC-fast plastic spectra is accomplished in a similar fashion to the phoswich calibration. The difference is that the gate lines are generated from known functional forms, whereas the gate lines are drawn by hand for the phoswich templates. These formulae are given by:

$$\begin{aligned} Ch_{BCC} &= aE_{BCC}^{\alpha Z+\epsilon} \\ Ch_{fast} &= b\left(\frac{E_{fast}^{\beta}}{A^{\gamma}Z^{\delta}}\right), \end{aligned} \tag{2.3}$$

where the exponential parameters α, β, γ, δ, and ϵ, and arbitrary constants a, and b are determined by fitting the curves described by these equations to the bands in the spectrum. Now the response function for the fast plastic has the same form as that previously used for the slow plastic in the phoswich calibration, because here the fast plastic is the stopping detector. Charge dependence was introduced into the exponent of the transmission mode equation to better fit the data produced by using lighter ionizing gases in the BCCs. Gain matching for the BCC-fast plastic spectra was done using the routine BRAGGMATCH, and the six mapping parameters (two

offsets, two gain factors, and the slope and intercept of the phoswich punch-in line) for each detector telescope are stored on disk.

To summarize, a master template is created for each spectral type to which all remaining spectra are gain matched. From these templates, lookup tables are generated which map channel number into particle type and incident kinetic energy. Emission angles for the detected particles are assigned as the geometric mean angles (listed in Appendix A) of the corresponding detector hit by the particle. Using these lookup tables and the gain matching parameters, raw data tapes are converted into "physics" tapes which contain the Z, A, θ, ϕ, kinetic energy, and number of the detector hit of each measured particle on an event-by-event basis. The intermediate step of producing physics tapes saves overall computation time, because multiple analyses can then be performed with the same data set without repeated preliminary reduction of the raw data.

Chapter 3

Event Characterization

3.1 Introduction

In this chapter three important quantities which characterize heavy-ion collisions: the impact parameter; the reaction plane; and the nuclear temperature, will be discussed for reference in the analyses of the remainder of this thesis. The impact parameter along with the target and projectile masses, and the incident projectile kinetic energy are the quantities which characterize the initial state of the system before the collision occurs. The impact parameter b characterizes the centrality of a collision (small (large) b correspond to central (peripheral) events), and consequently is a gauge of the violence of the event. The reaction plane is geometrically defined by the momentum vector $\mathbf{P}_z$ of the projectile and the center of the target. The impact vector $\mathbf{b}$, which joins the centers of the target and projectile at their closest approach, also lies in this plane. These geometrical relationships are shown schematically in Figure 3.1 for the laboratory reference frame. When applied to microscopic nuclear systems, the classical thermodynamic concept of temperature for macroscopic systems has provided considerable insight into heavy-ion reaction mechanisms. In nuclear collisions the collective translational kinetic energy can be deposited into other modes, predominantly the microscopic degrees of freedom of the the total system. Full damping

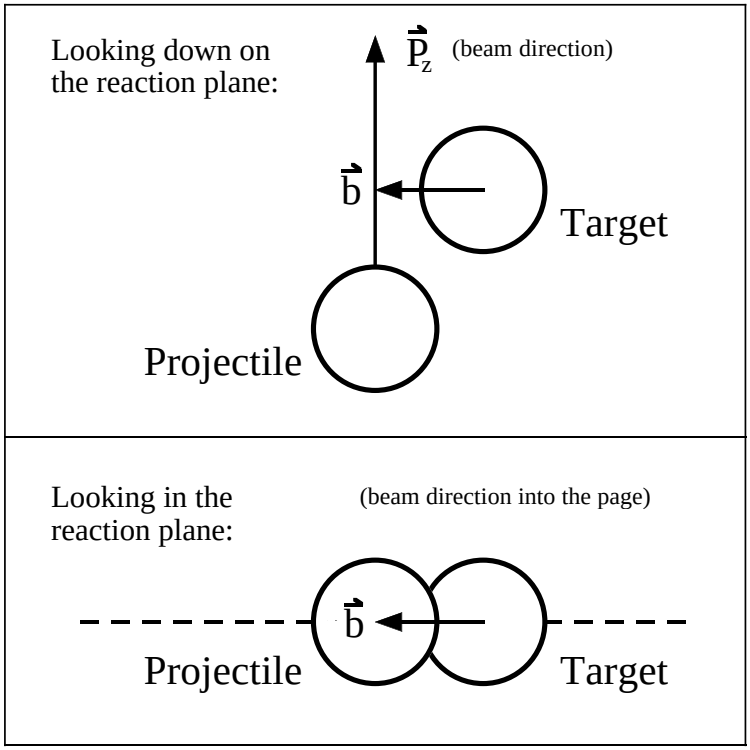

Figure 3.1: Geometrical description of the impact vector **b** and the reaction plane.

with the attainment of equilibration, represents a limit to this process, and nuclear temperature is one of the natural variables used to characterize systems that have reached this limit [Morr94].

3.2 Impact Parameter

A powerful feature of the MSU 4π Array is the ability to act as an impact parameter filter to make high-statistics exclusive measurements. So this device is well suited for this thesis experiment, because proper impact parameter selection is a critical component for both the radial flow analysis in Chapter 4, and the directed transverse flow analysis in Chapter 5. The importance of selecting central events to search for a radial flow signal has been previously emphasized [Barz91, Baue93, Jeon94, Dani95, Lisa95], because stopping power, compression, and equilibration are expected to be

greatest for collisions at small impact parameters. In these events nearly all the initial kinetic energy of the projectile is deposited into one midrapidity participant source. The importance of the role of the impact parameter in the determination of the disappearance of flow has also been previously recognized [Bert87, Sull90, Klak93]. As two nuclei collide at nonzero impact parameters, there is anisotropy in the pressure, resulting in a transverse flow of nuclear matter in the directions of the pressure gradient. In symmetric collisions the compressed midrapidity participant volume is expected to decrease in size with increasing impact parameter, so that a larger incident energy is required to compensate for the effects of the mean field in more peripheral collisions [Klak93]. In this section we will outline our method for impact parameter selection, so that the effects of the impact parameter on the collective motion can be determined through the analyses of the following chapters.

The impact parameter of a heavy-ion collision is classically defined to be the distance between the straight-line trajectories of the centers of the the two nuclei before their interaction. Impact parameter is not a directly accessible experimental quantity, but there are several measurable "centrality" variables which have been shown to be strongly correlated with the impact parameter [Gutb89, Ogil89a, Tsan89, Cava90, Pete90b, Phai92]. These global observables include the total charged-particle multiplicity N_{chgd}, the midrapidity charge Z_{mr}, and the reduced total transverse kinetic energy $\hat{E}_t$. The total charged-particle multiplicity is simply the number of charged particles identified in each event. The midrapidity charge [Ogil89a] is defined as the sum over identified charged particles in each event within the center-of-mass (c.m.) rapidity gate:

$$0.75y_{c.m.}^{targ} \leq y_{c.m.} \leq 0.75y_{c.m.}^{proj}, \tag{3.1}$$

or equivalently in the laboratory frame:

$$0.25y_{c.m.}^{sys} \leq y \leq 0.75y^{proj} + 0.25y_{c.m.}^{sys}. \tag{3.2}$$

The notation *proj*, *targ*, and *sys* refers to the projectile, target, and total system, and the rapidity in the laboratory frame is given by:

$$y = \frac{1}{2}\ln\left(\frac{\sqrt{m^2+p^2}+p\cos\theta}{\sqrt{m^2+p^2}-p\cos\theta}\right) = \tanh^{-1}(\beta\cos\theta), \tag{3.3}$$

where m, β, p, and θ denote the fragment's mass, velocity, momentum, and emission angle with respect to the beam axis. The rapidity is a Galilean invariant function of the velocity parallel to the beam axis, which reduces to β if this velocity is small compared to the speed of light. The reduced total transverse kinetic energy of identified particles is given by:

$$\hat{E}_t = (E_t/E_{proj}), \tag{3.4}$$

where the total transverse kinetic energy [Phai92] in each event, defined as:

$$E_t = \sum_{i=1}^{N} E_i \sin^2\theta_i = \sum_{i=1}^{N}(p_i\sin\theta_i)^2/2m_i, \tag{3.5}$$

has been divided by the projectile kinetic energy. Here E_i, m_i, p_i, and θ_i denote the kinetic energy, mass, momentum, and polar emission angle of ith particle in the laboratory frame. Impact-parameter-inclusive distributions containing three million events taken with a Ball-2 hardware trigger for each of these centrality variables are shown in Figure 3.2 where the solid (dashed) histograms are for incident beam energy of 115 (35) MeV/nucleon. The impact parameter of each event is assigned through cuts on such centrality variables, measured with the improved acceptance of the upgraded MSU 4π Array, as outlined below.

To obtain a quantitative estimate of impact parameter from any of the centrality variables, we use a straightforward geometrical prescription [Cava90] which assumes

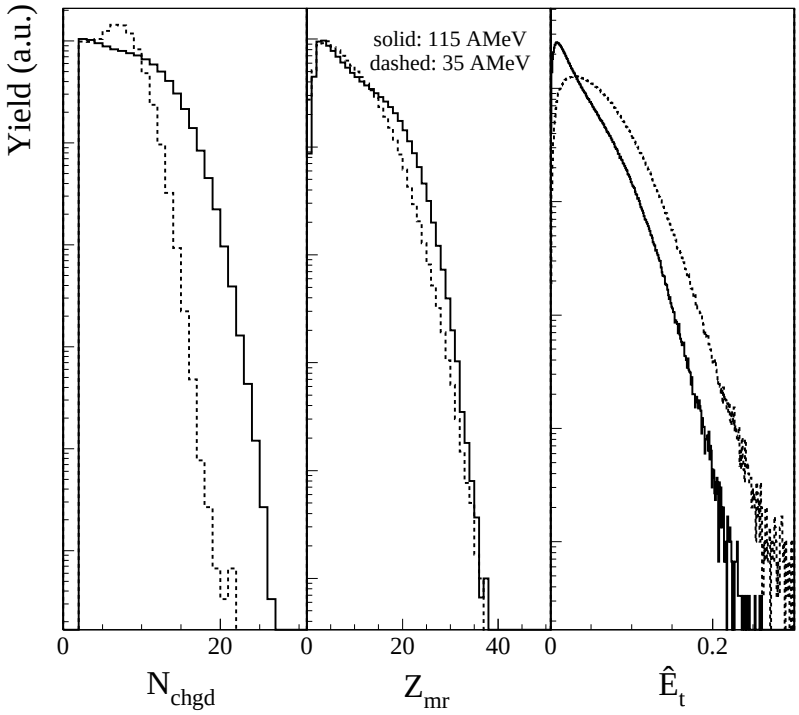

Figure 3.2: Impact-parameter-inclusive spectra taken with a Ball-2 trigger for each of the centrality variables defined in the text. Solid (dashed) histograms are for incident beam energy of 115 (35) MeV/nucleon.

that each variable q is monotonically related to impact parameter b. Thus the following relation can be written:

$$\frac{2\pi b db}{\pi b_{max}^2} = \pm f(q) dq. \tag{3.6}$$

In this expression b_{max} is the maximum impact parameter and $f(q)$ is the probability density function of observable q, *i.e.,* $f(q)dq$ is the probability of detecting a collision with a value of q' between q and $q+dq$. The function $f(q)$ is normalized to unity; the plus (minus) sign indicates that the variable q increases (decreases) as b increases. Integrating Equation 3.6 from b to b_{max} we obtain:

$$\int_b^{b_{max}} \frac{2bdb}{b_{max}^2} = \pm \int_{q(b)}^{q(b_{max})} f(q')dq'. \tag{3.7}$$

If we let:

$$F(q) = \pm \int_{q(b)}^{q(b_{max})} f(q')dq', \tag{3.8}$$

then:

$$b/b_{max} = \sqrt{1 - F(q)}. \tag{3.9}$$

Equation 3.9 constitutes our formula for calculating the impact parameter from a chosen centrality variable on an event-by-event basis. Figure 3.3 displays the results of using this equation for each of the global observables shown in Figure 3.2, where again the solid (dashed) histograms are for Ball-2 data at an incident beam energy of 115 (35) MeV/nucleon. Thus the measured impact-parameter-inclusive distribution

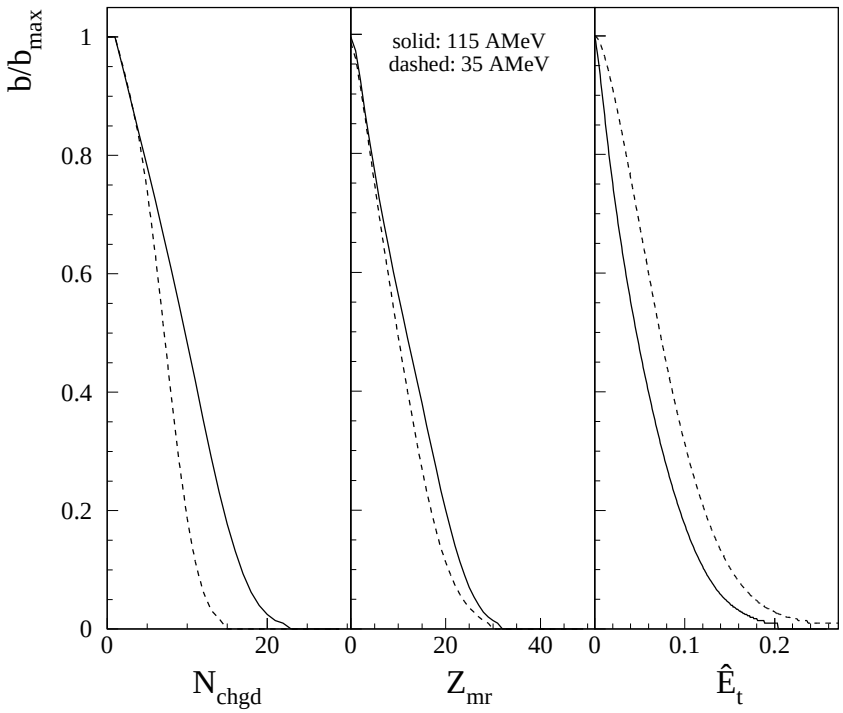

Figure 3.3: Reduced impact parameter as a function of the centrality variables shown in Figure 3.2 calculated using Equation 3.9. Solid (dashed) histograms are for Ball-2 data at an incident beam energy of 115 (35) MeV/nucleon.

of the centrality variable q is integrated, and the values of q corresponding to the specified values of b/b_{max} for the cuts become the thresholds used to accept or reject

events, *i.e.,* the limits on the reduced impact parameter bins.

From Figure 3.3 it is evident that events with larger values for each of these centrality variables correspond to events with smaller impact parameters. Because more kinetic energy will be transferred to the internal modes of the colliding system as the impact parameter decreases, this is physically reasonable to expect in each case. Certainly with higher internal energy the system is more likely to disassemble into a higher number of fragments, *i.e.,* N_{chgd} will be larger for central collisions. A greater number of these fragments will be from the participant volume moving at midrapidity, consequently contributing to a larger value for Z_{mr} in these reactions. In central collisions more energy is removed from the beam direction, increasing the value of $\hat{E}_t$ for these events compared to those with larger impact parameters.

As an example of the method used for impact parameter selection, events with $\hat{E}_t$ in the top 10% of the impact-parameter-inclusive $\hat{E}_t$ spectrum for the Ball-2 data were assigned to the most central bin. This corresponds to a reduced impact parameter of $\hat{b} = (b/b_{max}) \leq 0.32$ as calculated through the above geometric prescription [Cava90], where b_{max} represents the largest impact parameter leading to a triggered event. If the measured cross section was equivalent to the geometric (hard sphere) cross section, then b_{max} would be the sum of the projectile and target radii $R_{proj} + R_{targ}$. However, the actual maximum impact parameter to trigger an event is less than $R_{proj} + R_{targ}$, due to hardware trigger bias and detector acceptance [Llop95a].

In order to estimate b_{max} for the Ball-2 data, we adjusted the overall normalization of the inclusive $\hat{E}_t$ spectrum to fit the same distribution for data taken with the less selective HRA-1 trigger. Figure 3.4 is a typical example of the result for this fitting procedure. The solid (dashed) histogram is for data at 95 MeV/nucleon taken with a HRA-1 (Ball-2) hardware trigger. The deficiency of events with low

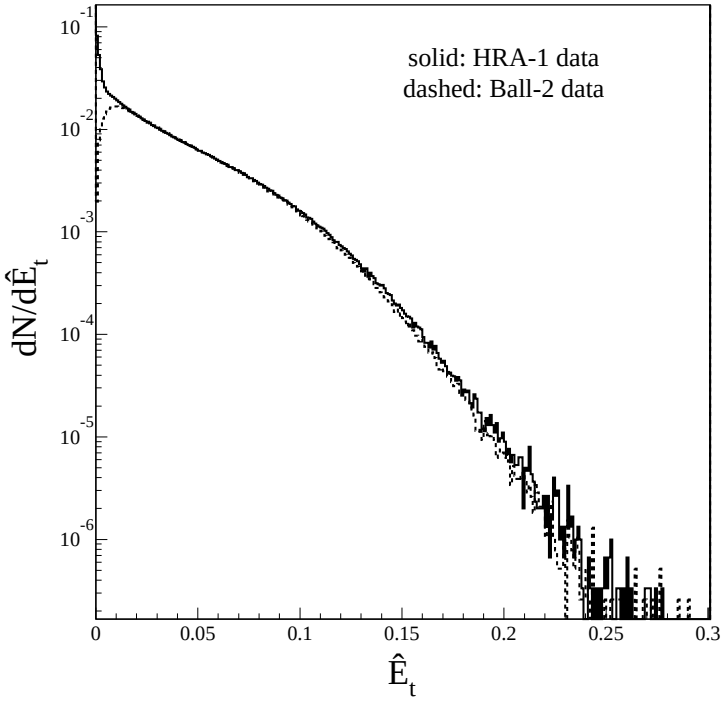

Figure 3.4: Renormalization of the inclusive $\hat{E}_t$ spectrum to determine b_{max} for the Ball-2 data. Solid (dashed) histogram is for data taken with a HRA-1 (Ball-2) hardware trigger.

$\hat{E}_t$ (mainly resulting from peripheral collisions) is the bias introduced by the Ball-2 hardware trigger for which we correct. From the ratio of the cross sections represented by the two inclusive $\hat{E}_t$ distributions we extracted for the Ball-2 events a value of $b_{max} = 0.88 \pm 0.04(R_{proj} + R_{targ})$, under the assumption that $R_{proj} + R_{targ}$ is the largest impact parameter leading to a triggered HRA-1 event. This results in a corrected $\hat{b} \leq 0.28$ for the top 10% most central Ball-2 events.

The correction factor did not vary significantly over the range of beam energies we measured. The remaining impact parameter bins and the corresponding reduced impact parameters in the simple geometric picture are summarized in Table 3.1. Also listed in this table are the effective values of the reduced impact parameter corrected for bias due to the Ball-2 hardware trigger condition. The values of $\hat{b}$ correspond to

the upper limit of each reduced impact parameter bin.

Table 3.1: Reduced impact parameter bins.

Bin No.	Centrality Variable Cut	Geometric $\hat{b}$	Corrected $\hat{b}$
BIN1	Top 10%	0.32	0.28
BIN2	10% - 20%	0.45	0.39
BIN3	20% - 30%	0.55	0.48
BIN4	30% - 40%	0.63	0.56
BIN5	40% - 50%	0.71	0.62
BIN6	50% - 75%	0.87	0.76
BIN7	Bottom 25%	1.00	0.88

The preferred centrality variable for impact parameter selection for this relatively light system is $\hat{E}_t$, because impact parameter binning could be more precisely controlled with $\hat{E}_t$ than N_{chgd} or Z_{mr} due to their discrete nature (integer values). This is demonstrated in Figure 3.5, which shows histograms of the fraction of events in each of the impact parameter bins specified in Table 3.1 for cuts on each of the centrality variables: solid for $\hat{E}_t$; dashed for Z_{mr}; and dotted for N_{chgd}. These Ball-2 data are the same three million event sample at incident beam energy of 115 MeV/nucleon shown in Figure 3.2. The bins for cuts on $\hat{E}_t$ clearly contain the more precise values for the specified percentages of events listed in Table 3.1.

Ideally, the variable upon which a centrality cut is made should be tightly correlated with the impact parameter, and negligibly correlated with the experimental observable of interest in all ways except through the impact parameter. Charge, mass, and momentum conservation laws can cause significant "autocorrelations" between a centrality variable and an observable. These autocorrelations may artificially enhance or suppress the measured value of that observable in events which are selected using the centrality variable to assign impact parameter [Llop95a]. For this reason, $\hat{E}_t$ should not be used as a centrality filter in the radial flow analysis because the

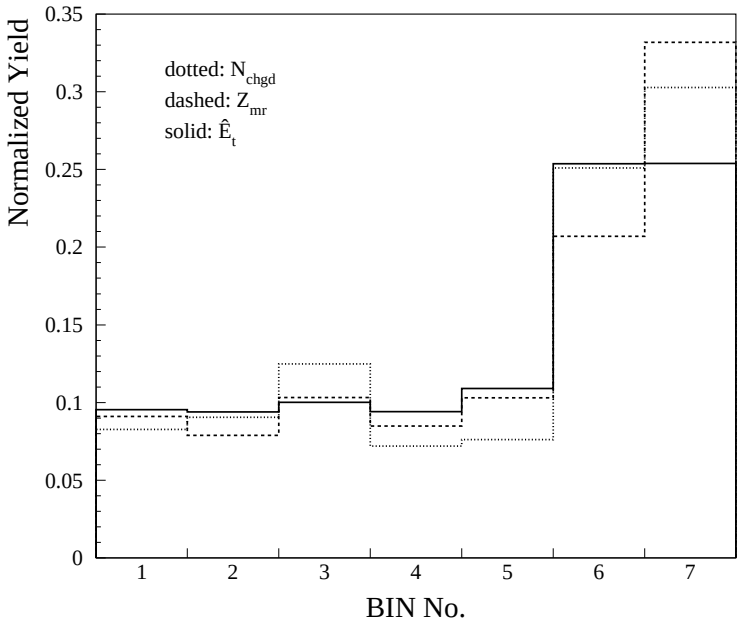

Figure 3.5: Fraction of events in each reduced impact parameter bin of Table 3.1 for cuts on N_{chgd} (dotted), Z_{mr} (dashed); and $\hat{E}_t$ (solid). The three million event sample was taken with a Ball-2 trigger at 115 MeV/nucleon.

radial flow energy is calculated from the mean transverse kinetic energy $\langle E_t \rangle$.

That $\hat{E}_t$ does not autocorrelate with the observable for directed transverse flow in the reaction plane $\langle p_x/p_t \rangle$ is demonstrated in Figure 3.6. The upper (lower) curves shown are the root-mean-square widthes (mean values) of $\langle p_x/p_t \rangle$ plotted versus $\hat{E}_t$ for three incident beam energies: circles are at 35 MeV/nucleon; squares are at 75 MeV/nucleon; and triangles are at 115 MeV/nucleon. The quantity $\langle p_x/p_t \rangle$ has been normalized because all charged particles are considered here (For further explanation of $\langle p_x/p_t \rangle$ refer to Chapter 5). That: (1) the mean values $\langle p_x/p_t \rangle$ are not correlated with $\hat{E}_t$; and (2) the relatively large rms widthes ($\sigma \approx 75\%$ of the maximum allowable value of $\langle p_x/p_t \rangle$) do not diminish in value, provide sufficient evidence that no autocorrelation exists between these observables. This is certainly reasonable, because the reaction plane can have an arbitrary orientation in space. Using methods similar to those outlined above, Z_{mr} is found to be an appropriate variable to use as a

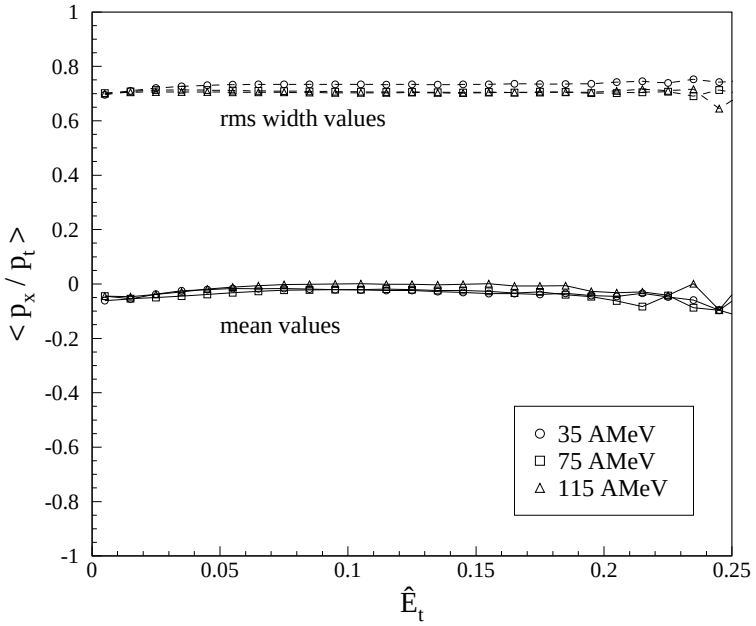

Figure 3.6: Means and root-mean-square widthes of the observable for directed transverse flow in the reaction plane $\langle p_x/p_t \rangle$ plotted versus the reduced transverse kinetic energy for three incident beam energies: 35 MeV/nucleon (circles); 75 MeV/nucleon (squares); and 115 MeV/nucleon (triangles).

centrality filter in the radial flow analysis, and does not autocorrelate with the radial flow observables.

To summarize, the centrality variable chosen for impact parameter selection was: (1) the midrapidity charge Z_{mr} of each event in the radial flow analysis of Chapter 4; (2) the reduced transverse kinetic energy $\hat{E}_t$ of each event in the directed transverse flow analysis of Chapter 5. The reduced impact parameter bins for either case are listed in Table 3.1. When we specify impact parameter in the analyses of the following chapters, we will use the corrected values in the fourth column of this table. This is an approximation because each value of the reduced impact given in Table 3.1 corresponds to a distribution of impact parameters in that $\hat{b}$ bin.

3.3 Reaction Plane

Various methods have been developed to construct the reaction plane on an event-by-event basis from the measured distribution of light fragments produced in heavy-ion collisions. These include the sphericity tensor method [Cugn82, Gyul82], the transverse momentum analysis [Dani85], and the azimuthal correlation technique [Wils92]. Both the sphericity tensor and transverse momentum techniques depend on the existence of directed transverse flow in the reaction plane. When collective flow is present, it is imperative to distinguish between the two sides of the reaction plane (as divided by the beam axis) which contain the forward and backward directed components of the particle flow. These two regions of the reaction plane are shown schematically in Figure 3.7 for the center-of-mass (c.m.) frame, where the perspective of this figure is looking down on the reaction plane. The projectile (target) is labeled with

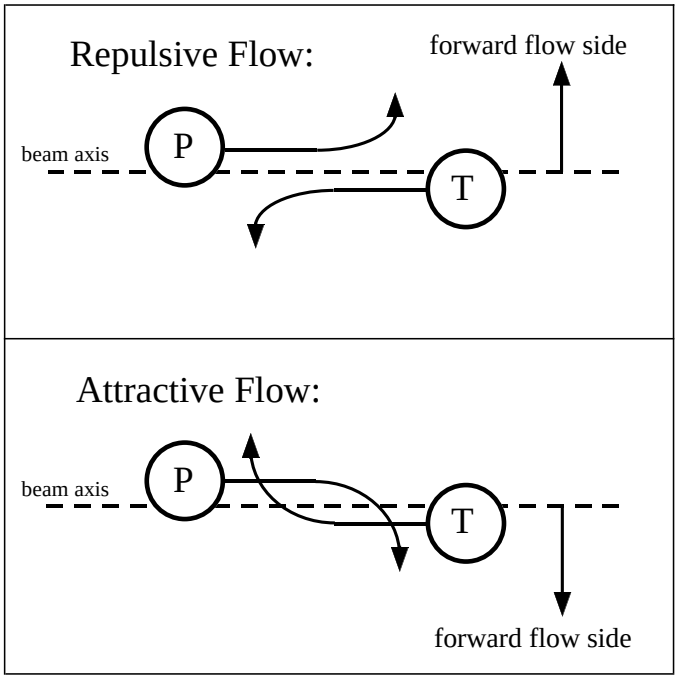

Figure 3.7: Definition of the forward side of the reaction plane for both repulsive and attractive scattering. The perspective of this figure is looking down on the reaction plane.

the letter **P** (**T**) in this diagram. For repulsive (attractive) scattering shown in the top (bottom) panel, the forward flow side is the area above (below) the dashed line, which represents the beam axis. As a convention, azimuthal angles with respect to the reaction plane will always be measured from the forward flow side.

The transverse momentum analysis has proven to be a more sensitive technique to extract the signal for collective transverse flow in the reaction plane than the sphericity tensor method [Dani85, Gutb89]. In the transverse momentum analysis [Dani85], a vector **Q** is constructed from the transverse momenta $\mathbf{p}_i^{\perp}$ of particles in an event:

$$\mathbf{Q} = \sum_{i=1}^{N} \omega_i \mathbf{p}_i^{\perp} \tag{3.10}$$

where the weight ω_i is chosen to be positive (negative) for particles emitted in the forward (backward) center-of-mass hemisphere. The reaction plane is defined by the beam axis and **Q**, *i.e.,* **Q** points toward the positive side of the plane. Application of the transverse momentum analysis method presumes that the dominant correlation between the fragment's transverse momenta is caused by collective motion within the reaction plane.

The azimuthal correlation technique [Wils90, Wils92, Hann95, Pak95] is a method for reaction plane determination based on the observation that particle emission is strongly enhanced in the reaction plane [Tsan84]. Thus, this technique involves finding the plane that aligns best with the enhancement plane. First a particle of interest (POI) is chosen from the event. Autocorrelation is avoided by omitting this POI in the calculation of the reaction plane [Dani85]. A recoil correction [Ogil89a] given by:

$$\mathbf{v}_{boost}^{\perp} = \frac{\mathbf{p}_{\mathrm{POI}}^{\perp}}{m_{sys} - m_{\mathrm{POI}}} \tag{3.11}$$

can be applied to boost each of the remaining particles toward the POI, where m_{sys} is the sum of the target and projectile masses, and m_{POI} and $\mathbf{p}_{\mathrm{POI}}^{\perp}$ are the mass and

transverse momentum of the particle of interest. The c.m. momenta of the remaining particles in the event are projected into a plane perpendicular to the beam axis (taken as the origin in this plane) as shown in Figure 3.8. In this diagram, the p^x

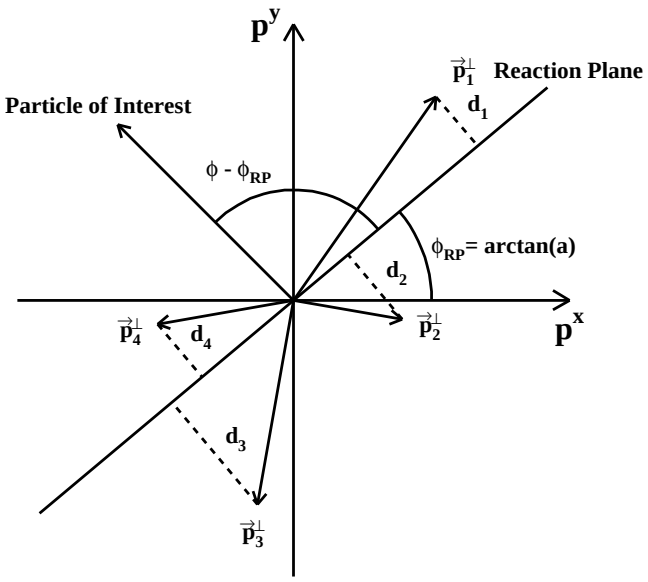

Figure 3.8: Quantities used to determine the reaction plane with the azimuthal correlation method, as described in the text, for an event projected into a plane perpendicular to the beam axis.

and p^y axes lie in the transverse plane, and the p^z axis coincides with the beam axis. The projection of the reaction plane, taken as a line with slope a, is determined by a simultaneous fit to the transverse momentum coordinates of these fragments (excluding the POI). The deviation of the particles in the event from the reaction plane D^2 is parameterized by the sum of the perpendicular squared distances d_i^2 between the line and the particles in the p^x-p^y plane as shown in Figure 3.8. The slope a corresponds to the tangent of the azimuthal angle of the reaction plane measured from the p^x axis, labeled $\phi_{\rm RP}$ in the figure. The deviation D^2 as a function of the

slope of the reaction plane's projection onto the p^x-p^y plane [Wils92] is given by:

$$D^2 = \sum_{i=1}^{N}[d_i^2] = \sum_{i=1}^{N}\left[(p_i^x)^2 + (p_i^y)^2 - \frac{(p_i^x + a p_i^y)^2}{1+a^2}\right]. \tag{3.12}$$

The sums in the equation are taken over the particles in the event. The condition that the derivative of D^2 with respect to a vanishes produces a quadratic equation whose roots,

$$a = \frac{\sum^N}{\sum_{i=1}[(p_i^y)^2 - (p_i^x)^2] \pm \sqrt{\left(\sum^N\right.}} \overline{\left.\begin{array}{l} 2\sum_{i=1}^{N}[(p_i^x)^2 - (p_i^y)^2])^2 + 4(\sum^N \\ \qquad\qquad i=1[p_i^x p_i^y] \qquad\qquad i=1[p_i^x p_i^y])^2 \end{array}\right.} \tag{3.13}$$

can be used to determine a. Substituting these roots back into the original equation allows selection of the root that minimizes D^2 and hence maximizes the in-plane enhancement.

The positive half of the reaction plane is associated with the side on which the total transverse momentum in the reaction plane $p^x_{\rm RP}$ is greatest in value. This is determined by substituting the roots in Equation 3.13 into an expression for the weighted projection of the transverse momenta onto the line found with slope a [Hann95]:

$$p^x_{\rm RP} = \sum_{i=1}^{N}\omega_i \mathbf{p}_i^{\perp}\cdot\hat{\mathbf{a}} = \sum_{i=1}^{N}\left[\omega_i \frac{(p_i^x + a p_i^y)}{\sqrt{1+a^2}}\right]. \tag{3.14}$$

In this expression $\hat{\mathbf{a}}$ is a unit vector of slope a, and the weight ω_i is chosen to be positive (negative) for particles emitted in the forward (backward) c.m. hemisphere. The root which minimizes D^2 in Equation 3.12 is correlated to the maximum value of $p^x_{\rm RP}$, and therefore defines the positive side of the reaction plane. This has made the azimuthal correlation method self-contained, *i.e.,* it is no longer necessary to rely on another technique (*e.g.,* **Q**-vector) to determine the positive side of the reaction plane. The azimuthal angle of a particle of interest with respect to the forward flow side of the reaction plane (ϕ - $\phi_{\rm RP}$) is shown in Figure 3.8.

This procedure is repeated for each particle in the event for all events with at least four identified particles, resulting in N_{chgd} reaction planes for each of these events.

The dispersion of the azimuthal angles of the reaction planes ϕ_{RP} in an event about the average value for the event ϕ_{RP}(event ave.) is shown in Figure 3.9. These data are

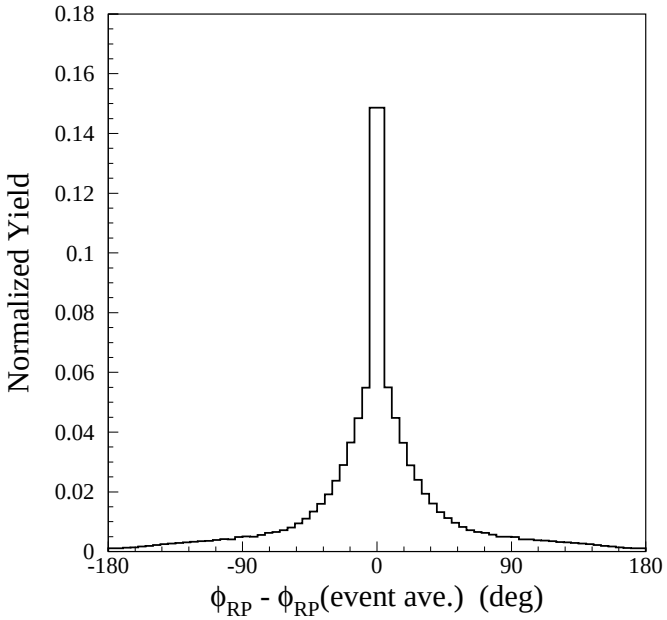

Figure 3.9: Distribution of azimuthal angle differences between reaction planes in the event ϕ_{RP}, and the average value of the event ϕ_{RP}(event ave.) for 115 MeV/nucleon ^{40}Ar+^{45}Sc reactions.

^{40}Ar+^{45}Sc reactions at 115 Mev/nucleon, and similar results are found at the other incident beam energies. The fairly narrow distribution (rms width = 49°) about the event average demonstrates the validity of viewing each event as a set of subevents with a separate reaction plane for each POI, which greatly enhances the statistics of the method.

Figure 3.10 displays the distribution of azimuthal angle differences between reaction planes found using the transverse momentum analysis ϕ_{RP}(TM), and the azimuthal correlation method ϕ_{RP}(AC) for ^{40}Ar+^{45}Sc reactions at 75 MeV/nucleon. Reasonable agreement (rms width = 34°) is obtained between the different techniques for reaction plane determination. Since the transverse momentum analysis primarily uses the presence of transverse flow to find the reaction plane, this implies

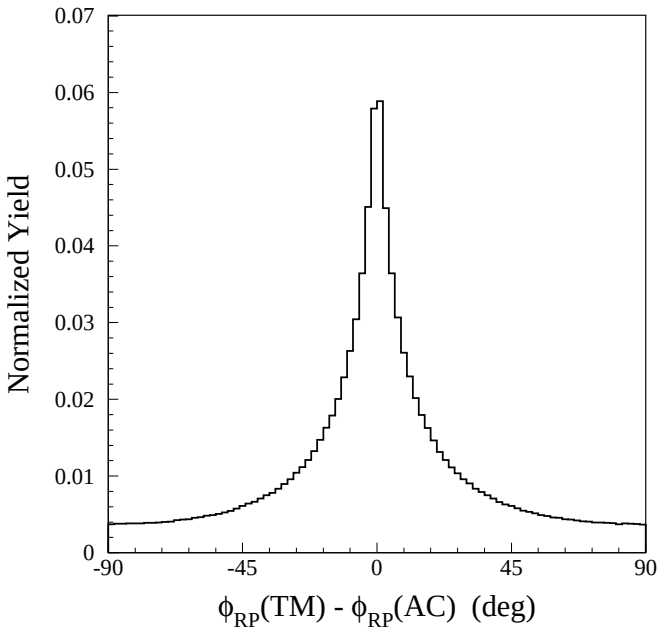

Figure 3.10: Distribution of azimuthal angle differences between reaction planes found using the transverse momentum analysis $\phi_{\mathrm{RP}}(\mathrm{TM})$, and the azimuthal correlation method $\phi_{\mathrm{RP}}(\mathrm{AC})$ for 75 MeV/nucleon ^{40}Ar+^{45}Sc events.

that the flow and the general in-plane enhancement are coplanar [Wils92]. Consequently, the method of azimuthal correlations remains more suitable to determine the reaction plane in cases where transverse collective motion can become weak, *e.g.,* beam energies near the balance energy.

As previously stated, the POI was excluded from the sums in Equation 3.13 to avoid autocorrelation. The large peak at 0° in Figure 3.11 demonstrates there is little reduction in accuracy resulting from exclusion of the POI in the reaction plane determination [Wils92]. Shown in this figure is the azimuthal distribution of the differences between reaction planes found for the entire event $\phi_{\mathrm{RP}}(\mathrm{event})$, and reaction planes found leaving out the particle of interest $\phi_{\mathrm{RP}}(\mathrm{POI})$ for 75 MeV/nucleon ^{40}Ar+^{45}Sc events. The small peak at 180° represents the slight probability that the positive side of the reaction plane flips when the POI is removed in the calculation.

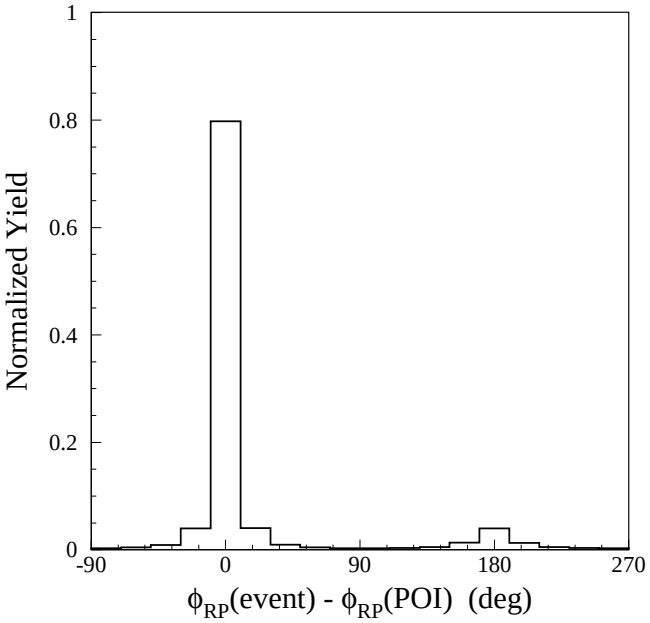

Figure 3.11: Azimuthal distribution of the differences between reaction planes found for the entire event $\phi_{\rm RP}$(event), and reaction planes found leaving out the particle of interest $\phi_{\rm RP}$(POI) for 75 MeV/nucleon ^{40}Ar+^{45}Sc events.

The azimuthal angles of the reaction planes $\phi_{\rm RP}$ calculated with $Z = 3$ as the POI versus $\phi_{\rm RP}$ calculated with $Z = 2$ as the POI is shown in Figure 3.12 for 115 MeV/nucleon ^{40}Ar+^{45}Sc reactions. A strong correlation clearly exists between the reaction planes determined for different POI [Pak95]. The faint bands originating at 180° are again due to the reversal of the positive side of the reaction plane. To investigate whether there is any multiplicity dependence of this correlation, the difference of the azimuthal angles for the reaction planes with He and Li fragments as the POIs $\Delta\phi_{\rm RP} = \phi_{\rm RP}(Z = 2) - \phi_{\rm RP}(Z = 3)$ was calculated as a function of the charged-particle multiplicity N_{chgd}. We observed that the rms width of this distribution for $\Delta\phi_{\rm RP}$ is independent of N_{chgd}, so that multiplicity distortions are a negligible effect on this correlation. Comparison between other particle types yields similar results.

Having shown that the reaction planes for different particle types are strongly correlated, we can examine azimuthal distributions with respect to the reaction plane

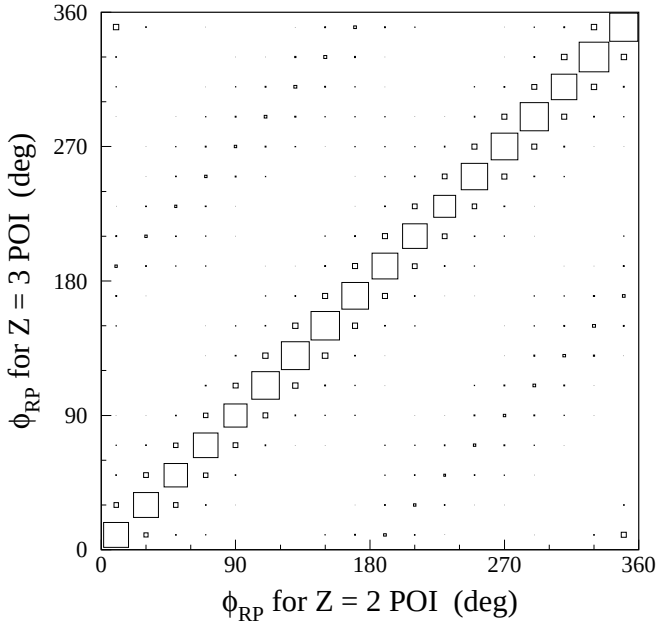

Figure 3.12: Azimuthal angles of the reaction planes $\phi_{\rm RP}$ calculated with $Z = 3$ as the POI versus $\phi_{\rm RP}$ calculated with $Z = 2$ as the POI for 115 MeV/nucleon ^{40}Ar+^{45}Sc reactions.

that include all charged particles. In Figure 3.13 we display $dN/d\phi$ in arbitrary units as a function of $\phi - \phi_{\rm RP}$ for two rapidity regions, where N is the number of identified fragments and $\phi - \phi_{\rm RP}$ is the azimuthal angle around the beam axis measured with respect to the forward side of the reaction plane. Enhanced emission for the 45 MeV/nucleon ^{40}Ar+^{45}Sc collisions is indicated by the simultaneous peaks on both the forward flow side ($\phi - \phi_{\rm RP} = 0°$) and the backward flow side ($\phi - \phi_{\rm RP} = 180°$) of the reaction plane. The panels on the left side demonstrate the spurious autocorrelation between the POI and the reaction plane when the particle of interest is not removed from the sums in Equation 3.13 for the reaction plane calculation. The panels on the right show the effect of including the recoil correction given by Equation 3.11 in the reaction plane determination. In both rapidity regions the particles are boosted toward the forward flow side ($\phi - \phi_{\rm RP} = 0°$) as a result of this measure to restore momentum conservation. Also apparent in upper panel on the right side is a dip at 0°

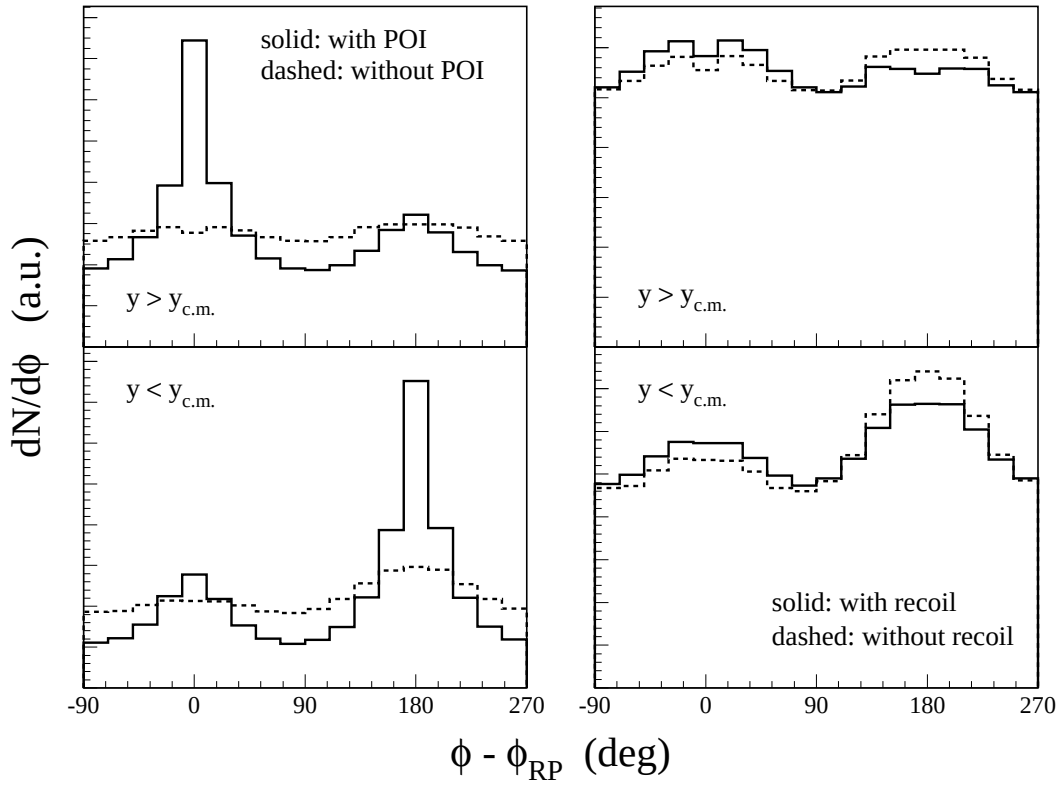

Figure 3.13: Azimuthal distributions of all charged particles from 45 MeV/nucleon ^{40}Ar+^{45}Sc reactions where the upper (lower) panels are for fragments forward (backward) of the system center-of-mass. The solid (dashed) histograms in the panels on the left side are found with (without) the POI included in the reaction plane calculation. The solid (dashed) histograms in the panels on the right side are found with (without) the recoil correction included in the reaction plane calculation.

attributed to the finite granularity of the detector array. This dip occurs because it is difficult to place a POI close to the found reaction plane since some of the detectors at azimuthal angles must already have been hit [Wils92].

The dependence on incident beam energy for the azimuthal distributions is shown in Figure 3.14 for rapidities y forward (left panels) and backward (right panels) of the system center-of-mass. The particle of interest is lithium in these distributions, and the recoil correction given by Equation 3.11 was used in the reaction plane calculation. The in-plane enhancement pattern is consistent with directed collective flow in the reaction plane, *i.e.,* a peak on the forward (backward) flow side for rapidities greater (less) than the system center-of-mass. The strength of the signal diminishes as the incident beam energy increases already hinting at the disappearance of flow that will be explored in greater detail in Chapter 5. That more azimuthally symmetric distributions of light particles are produced as the projectile energy increases has been demonstrated with correlation functions [Lace93] and anisotropy ratios [Wils90, Wils95].

As a final note about reaction plane determination, the above methods can only estimate the true reaction plane. Even for a perfect detector system, thermal fluctuations would cause dispersion about the true value for the reaction plane of the event [Sull92]. Because of the difference between the true and estimated reaction planes, the observed transverse flow projected into the estimated reaction plane will always be smaller than the actual flow. Various means [Dani85, Doss86, Dani88] have been devised to compensate for such effects, but a systematic study of these correction factors [Sull92] concluded that introducing the inaccuracies of the reaction plane determination into the theoretical calculations is better for comparisons with the data. The choice of the observable for zero collective flow removes the need to correct for the dispersion of the estimated reaction plane with respect to the true

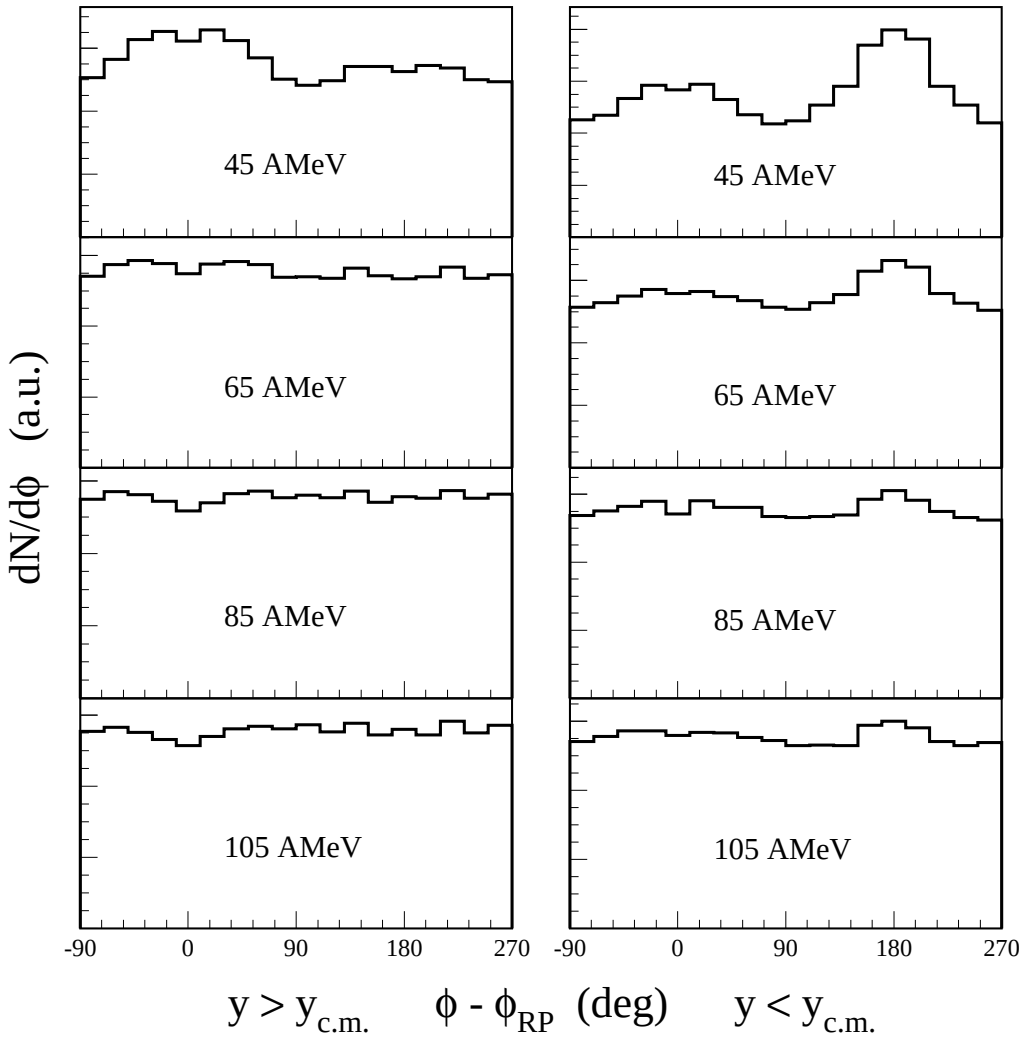

Figure 3.14: Azimuthal distributions for $Z = 3$ fragments from ^{40}Ar+^{45}Sc reactions at four incident beam energies. The panels on the left (right) side are for lithiums forward (backward) of the system center-of-mass. The reactions planes calculated in these distributions include a recoil correction.

reaction plane altogther [Ogil90], because the balance energy is independent of this dispersion. Consequently, the difficulties inherent with filtering transport model calculations are avoided, and the measured balance energies can be directly compared to the theoretical predictions.

3.4 Temperature

The subject of a temperature to describe the state of nuclear matter has been a major area of study in the field of heavy-ion reactions. The reason for this interest is that equilibrium and temperature represent central concepts in the thermodynamic description of these reactions and their evolution [Morr94]. In this section we shall only briefly outline the established method we used to extract the temperature from our data. The kinetic energy spectra of light particles produced in intermediate energy heavy-ion collisions can be described by an expression for volume emission from thermal sources of the form:

$$\frac{d^2N}{d\Omega dE} \propto \sqrt{E}\exp\left(-\frac{E}{T}\right) \tag{3.15}$$

in the source frame of reference. In this expression, called a non-relativistic Maxwell-Boltzmann (MB) distribution, N is the number of particles emitted into solid angle Ω, E is the kinetic energy of the emitted particle, and T is the temperature parameter.

In Figure 3.15 we display the kinetic energy spectra for protons from central collisions (for $\hat{b}$ bin BIN1 in Table 3.1) at all nine incident beam energies. To isolate the midrapidity participant source (for reasons described in detail in Chapter 4) only protons with center-of-mass polar angle $\theta_{\rm c.m.} = 90^\circ \pm 15^\circ$ are considered in these spectra. The azimuthal rings of detectors at laboratory polar angles (given in Table A.1 in Appendix A) corresponding to this range of angles in the c.m. frame were used to construct this gating condition. The spectra are cutoff at 200 MeV because

at this energy the protons begin to punch-out the back of the main ball detector telescopes.

The distibution in Equation 3.15 is assumed to be isotropic in a frame moving with velocity β with respect to the laboratory frame. Fits to the spectra in the laboratory frame are obtained by transforming relativistically from the source rest frame to the laboratory using:

$$\frac{d^2N}{d\Omega dE} = \left(\frac{p}{p'}\right) \frac{d^2N}{d\Omega' dE'} \tag{3.16}$$

where

$$E' = \gamma(E - \beta p \cos\theta). \tag{3.17}$$

The primed (unprimed) quantities refer to the source (laboratory) frame, where E, p, and θ denote the total energy, momentum, and polar emission angle of a particle with mass m, and $\gamma = (1-\beta^2)^{-1/2}$. Fitting the spectra with Equations 3.16 and 3.17 yields the curves shown in Figure 3.15. The temperature parameters (inverse "slopes") extracted from this fitting procedure, which increase as the incident beam energy increases, are listed in the third column of Table 4.1.

In Figure 3.16 we display kinetic energy spectra for $Z = 3$ fragments at all nine incident beam energies produced under the same conditions given above for the protons (for $\hat{b}$ bin BIN1 in Table 3.1 and $\theta_{\rm c.m.} = 90^\circ \pm 15^\circ$). These spectra for lithium are not described well by the relativistic MB funtional form, and the temperatures yielded by this fitting procedure are not the same as those for the protons at the corresponding incident beam energies as listed in Table 4.1. This discrepancy becomes the main motivation behind the study in the following chapter of this thesis.

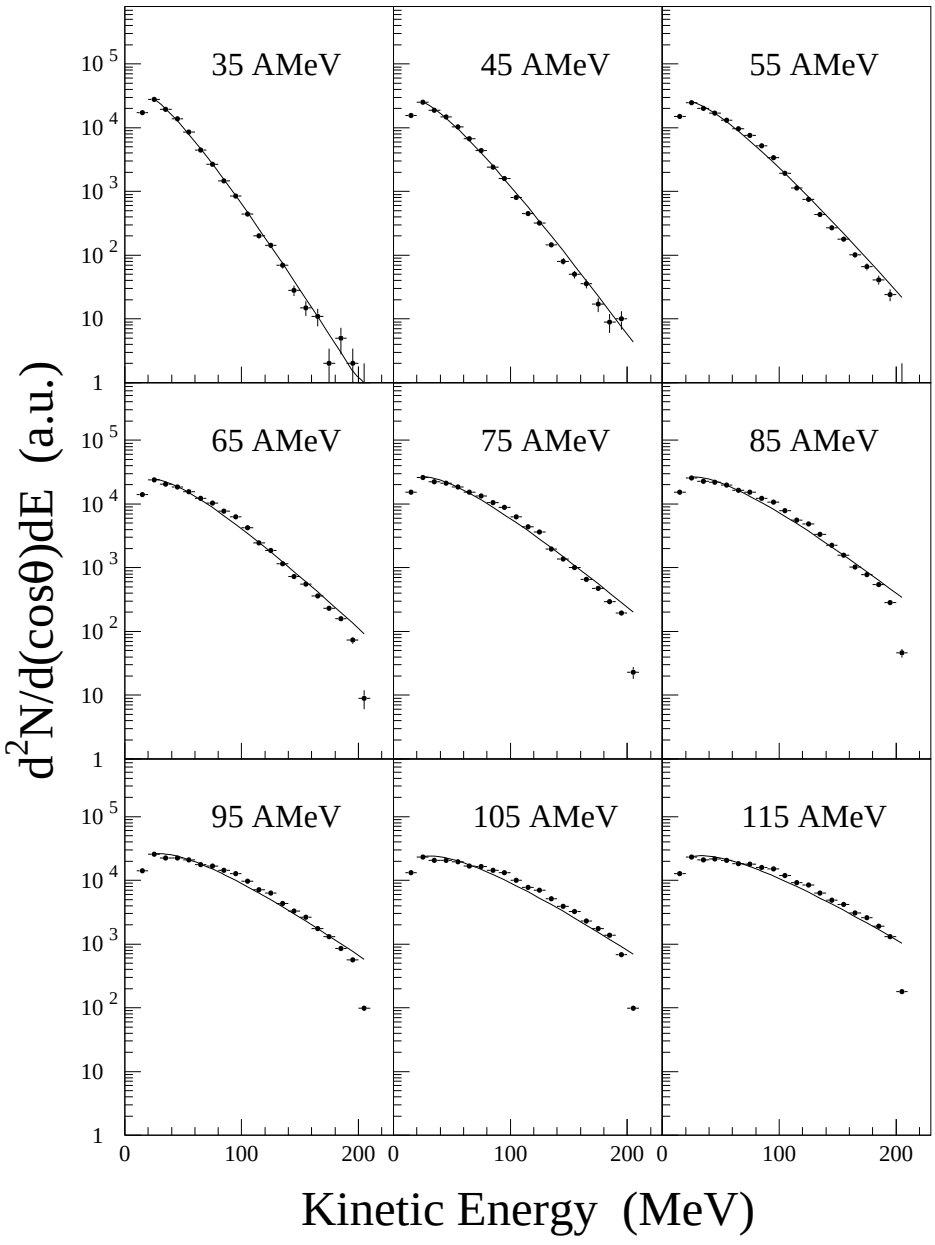

Figure 3.15: Kinetic energy spectra in the laboratory frame for protons from central ^{40}Ar+^{45}Sc collisions at $\theta_{\rm c.m.} = 90° \pm 15°$ for nine incident beam energies. The lines are single moving thermal source fits.

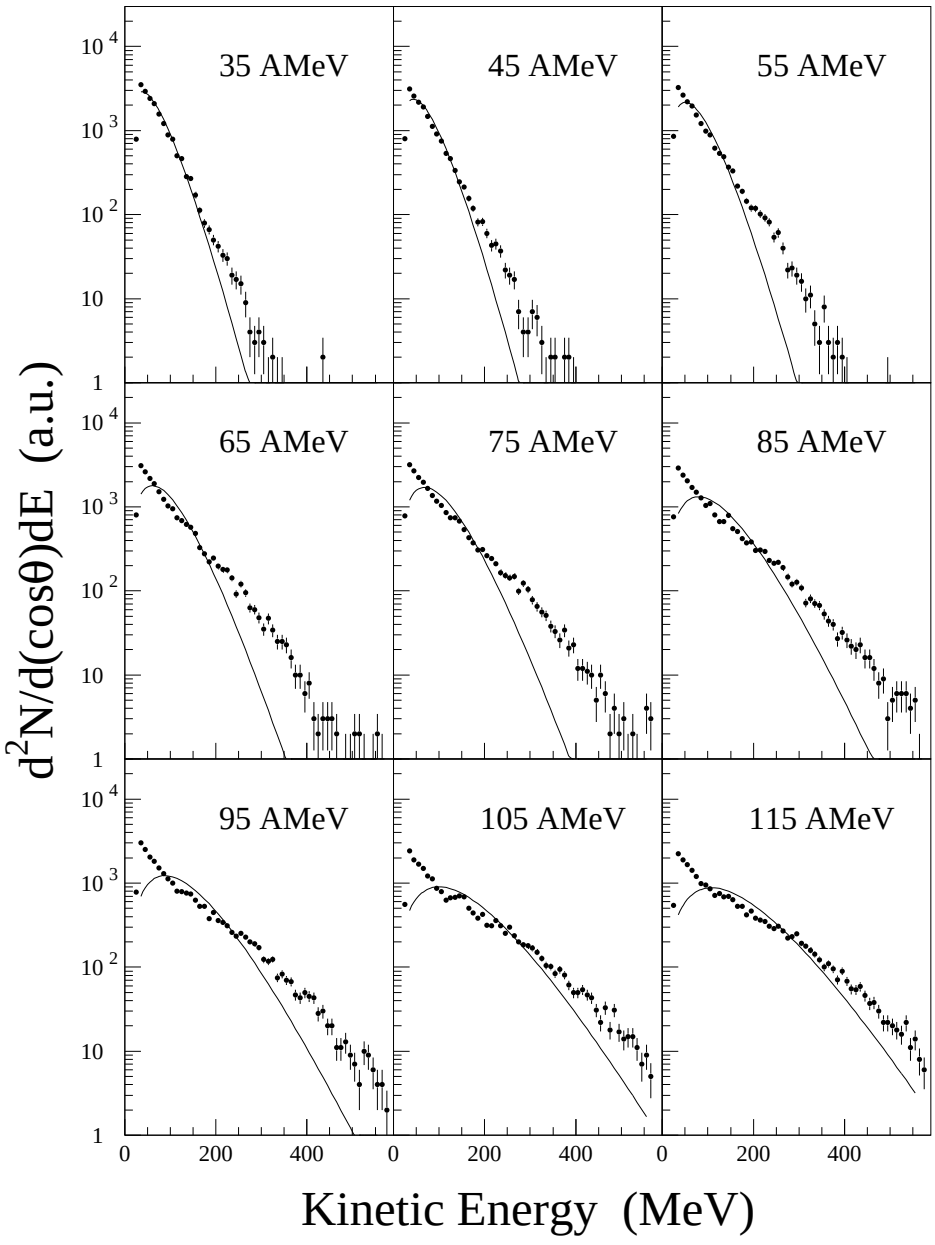

Figure 3.16: Kinetic energy spectra in the laboratory frame for $Z = 3$ fragments from central ^{40}Ar+^{45}Sc collisions at $\theta_{\rm c.m.} = 90° \pm 15°$ for nine incident beam energies. The lines are single moving thermal source fits.

Chapter 4

Radial Flow

4.1 Introduction

Collective motion of nucleons in heavy-ion collisions offers a glimpse at the true many-body effects not present in simple superpositions of individual two-body interactions. Derivation of an equation of state (EOS) for nuclear matter has been the main motivation for studying the collective effects resulting from these collisions [Gutb89]. Collective radial expansion of particle emission from central nuclear collisions, termed radial flow, was originally postulated to explain the observed differences in the slopes of the inclusive pion and proton energy spectra [Siem79]. Radial flow was primarily attributed to the conversion of thermal and compressional energy into work through a pressure gradient in the hydrodynamic limit [Bond78, Siem79]. Consequently, the fragments acquire a net outward radial velocity in addition to their random thermal component, which is evident from the increased curvature in the single-particle energy spectrum. After directed collective transverse flow was demonstrated to be a signature of hydrodynamical compression [Gust84, Gutb89], a study of transverse energy production [Doss88] was undertaken, aimed at accounting for the discrepancy between the measured and calculated thermal mean transverse energies. In that investigation, approximately 40% of the total kinetic energy in the center-of-mass (c.m.) frame was

reported to be converted into compressional energy in the moment of highest density [Doss88]. Subsequent work [Dani92, Jeon94, Hsi94, Kund95, Dani95, Pogg95, Lisa95] for heavy systems at relatively high beam energies ($\geq$ 100 MeV/nucleon) has also revealed that radial flow is a major contribution to the energy dissipation in the disassembly process of excited nuclear matter (see Figures 1.5 and 1.6).

Indications are that radial flow persists down into the intermediate beam energy regime [Frie90, Barz91, Hage92, deSo93, Baue93, Heue94, Schu95, Jeon95], and is also important for spectator emission from the excited projectile-like fragment [Kund95, Jeon95]. This radial flow phenomenon may even lead to the transient formation of hollow structures such as bubbles or toroids [Baue92, More92] at these projectile energies. At the end of Chapter 3, we presented kinetic energy spectra at 90° in the c.m. frame for lithium fragments produced in central ^{40}Ar+^{45}Sc collisions, which exhibited increased curvature compared to the proton spectra (Figures 3.15 and 3.16). The observed differences in the temperatures extracted from single moving thermal source fits to these spectra are attributed to collective radial expansion of the midrapidity participant volume.

In this chapter we present results from a systematic study for the incident beam energy and impact parameter dependence of collective radial flow for our relatively light system in the intermediate beam energy energy regime. Comparison to predictions of Boltzmann-Uehling-Uhlenbeck (BUU) model and WIX multifragmentation model calculations showing agreement with our measured values of radial flow observables are presented. We shall show that the relative contribution of collective radial flow extracted from the mean transverse kinetic energy accounts for approximately half of the emitted particle's energy for the heavier fragments ($Z \geq 4$) at the highest beam energy studied here in this thesis experiment.

4.2 Transverse Energy Production

In addition to selecting central collisions to search for a radial flow signal (as emphasized in Section 3.2), reaction products should be measured at 90° in the center-of-mass (c.m.) frame to suppress the contamination by spectator emission and directed flow effects [Siem79, Dani92, Hsi94, Lisa95]. We show in Figure 4.1 the effect of placing various centrality and angular gating conditions on the data. The mean transverse

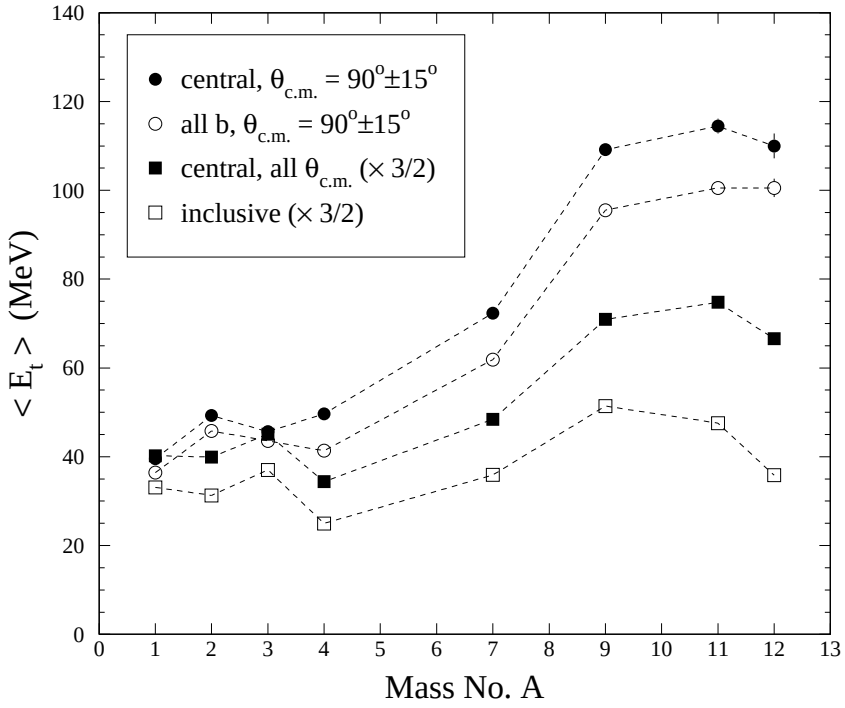

Figure 4.1: Mean transverse kinetic energy from ^{40}Ar+^{45}Sc reactions at beam energy 115 MeV/nucleon versus fragment mass number for various centrality and angular gating conditions as defined in the inset and the text. The lines are included to guide the eye.

kinetic energy $\langle E_t \rangle$ is plotted versus the mass number A for fragments up to carbon from ^{40}Ar+^{45}Sc reactions at a beam energy of 115 MeV/nucleon. The errors shown are statistical. The quantity $\langle E_t \rangle$ is defined as the mean value over all events meeting the specified selection criteria, where the transverse kinetic energy E_t for each of these

events is found using Equation 3.5.

A systematic increase in the values of $\langle E_t \rangle$ for central events without any angular cut (solid squares) is observed in Figure 4.1 for all fragments over the inclusive (open squares) data set. The values of $\langle E_t \rangle$ for these two data types have been multiplied by a factor of three halves [Dani92] for comparison to the data at 90° in the c.m. frame ($\theta_{\rm c.m.} = 90°$). The values of $\langle E_t \rangle$ again show an increase for all fragments over the inclusive values, when only fragments at $90° \pm 15°$ in the c.m. frame with no restriction on impact parameter (open circles) are considered. The azimuthal rings of detectors at laboratory polar angles (given in Table A.1 in Appendix A) corresponding to this range of angles in the c.m. frame were used to construct this gating condition. Finally, the central event set at $90° \pm 15°$ in the c.m. frame (solid circles) systematically shows the largest values for $\langle E_t \rangle$, demonstrating the importance of satisfying both conditions in searching for a radial flow signal. The trends are essentially preserved for the protons, deuterons, and tritons although the differences between data types are not as pronounced due to contributions from pre-equilibrium emission [Pete90a], and because radial flow has been shown to be smaller for these lighter particle species [Siem79, Dani92, Barz91, Baue93]. These selection criteria were applied to the data in the radial flow analysis described below.

In Figure 4.2 we display the dependence of $\langle E_t \rangle$ on the incident beam energy for the different fragment types at two reduced impact parameter bins. The data are for ^{40}Ar+^{45}Sc reactions at $\theta_{\rm c.m.} = 90° \pm 15°$, and the errors shown are statistical. The reduced impact parameter bins were determined as outlined in Section 3.2 (the values of b/b_{max} correspond to the upper limit of each $\hat{b}$ bin). For the more central events displayed in the lower panel, the values of $\langle E_t \rangle$ show a monotonic increase as the beam energy increases for all particle types, which becomes particularly dramatic for the larger mass fragments. This is in striking contrast to the more peripheral event

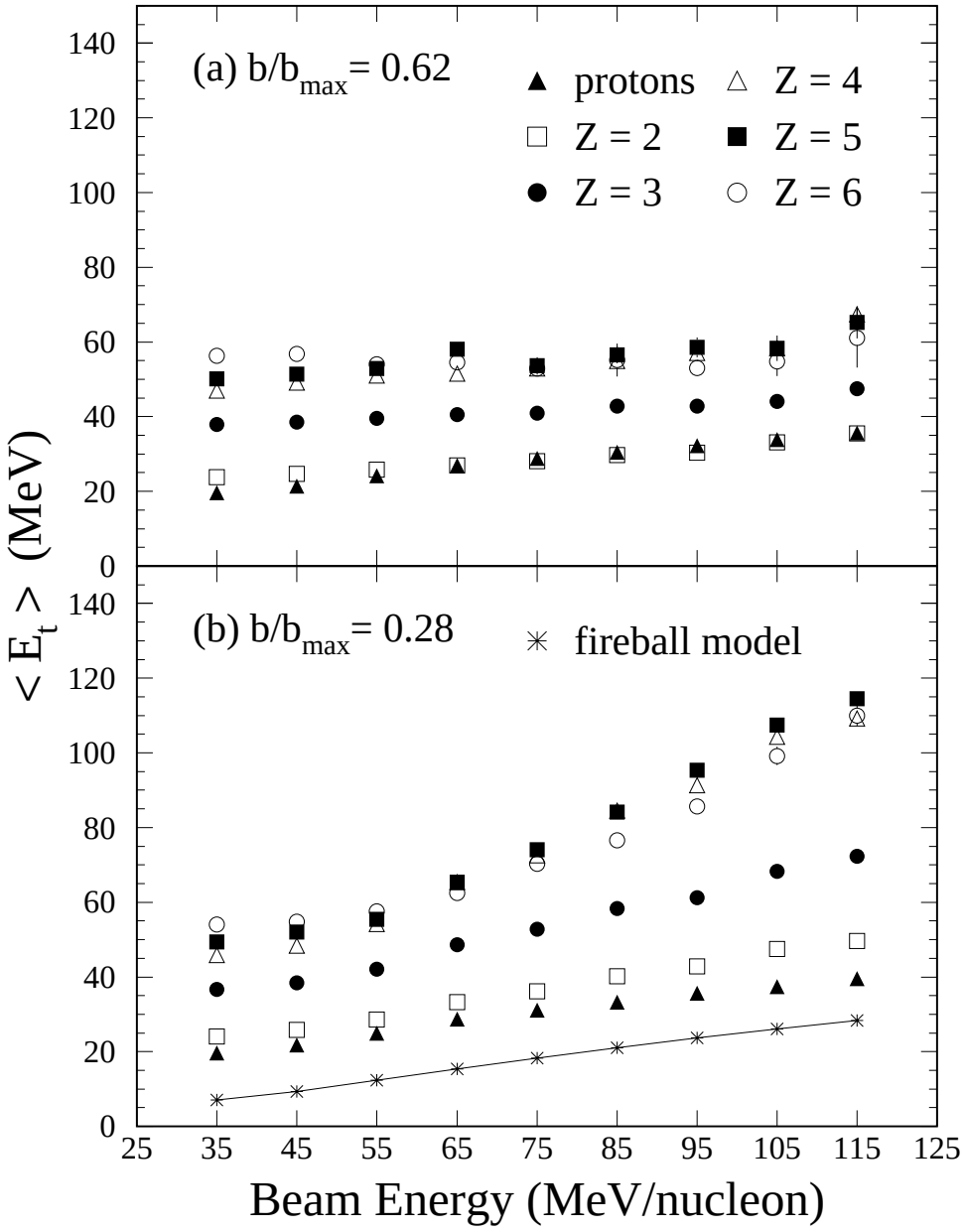

Figure 4.2: Mean transverse kinetic energy of fragments from ^{40}Ar+^{45}Sc reactions at polar angles $\theta_{\mathrm{c.m.}} = 90° \pm 15°$ versus incident beam energy for two impact parameters bins. Predictions from the fireball model [West76] are shown in lower panel (asterisks).

set shown in the upper panel, for which the values of $\langle E_t \rangle$ exhibit a gradual increase as a function of beam energy regardless of mass.

The difference in the values of $\langle E_t \rangle$ at each beam energy between fragment types in the upper panel of Figure 4.2 is attributed to the difference in the low-energy thresholds in the BCCs for the different particle types, and should not be interpreted as a deviation from thermal equilibrium. This difference (an effect also present in the lower panel) nearly vanishes if an artificial common threshold equal to the low-energy threshold in the BCCs for carbon is made in software on the other particle types. This is demonstrated in Figure 4.3, which is identical to Figure 4.2 except that this artificial common low-energy threshold was placed on all fragments with $Z \leq 5$. The lines connecting the points for carbon are included to guide the eye. The apparent leveling of $\langle E_t \rangle$ for heavier fragments in central collisions at beam energies below 55 MeV/nucleon (most evident in the lower panel of Figure 4.2) is also an artifact of these low-energy thresholds.

At the higher beam energies, where low-energy thresholds have a less significant effect, the dramatic increase in the values of $\langle E_t \rangle$ for the heavier fragments produced in central collisions is linked to larger values of the radial flow energy [Pak96b]. This is in contrast to expectations of a purely thermal source for which the different particle types are emitted with the same mean kinetic energy. For comparison we show in the lower panel of Figure 4.2 the predictions of a purely thermal model calculation, the fireball model [West76], at each of the projectile energies (asterisks). These calculations were not corrected for detector acceptance effects. The large values of $\langle E_t \rangle$ for the heavy fragments ($Z \geq 4$) in central collisions at the higher beam energies underscore the importance of radial flow in the nuclear disassembly process for these events.

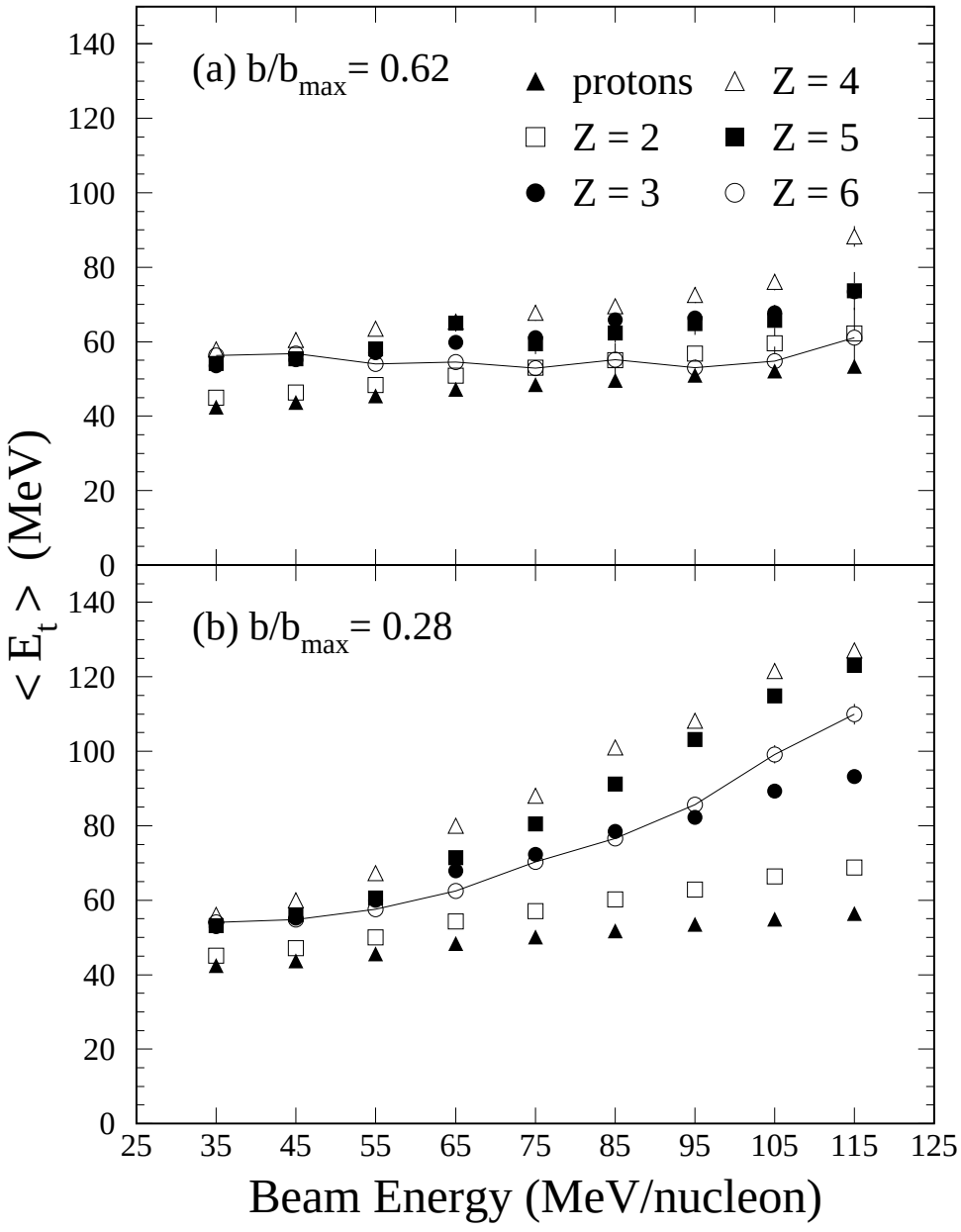

Figure 4.3: Same as Figure 4.2 except with an artificial common low-energy threshold set for all fragments with $Z \leq 5$. The lines are included to guide the eye.

At the beginning of this section, we stated that reaction products should be measured at 90° in the c.m. frame in order to suppress the contamination by spectator emission and directed flow effects [Siem79, Dani92, Hsi94, Lisa95]. Figure 4.4 shows the reduction in $\langle E_t \rangle$ due to these effects for central collisions ($\hat{b} = 0.28$) of the ^{40}Ar+^{45}Sc system. The upper (lower) panel in this figure is for c.m. polar angle bin $\theta_{\rm c.m.} = 45° \pm 15°$ ($\theta_{\rm c.m.} = 90° \pm 15°$). At $\theta_{\rm c.m.} = 45°$, there is a larger contribution to light particle emission from the projectile spectator, and a greater directed transverse flow signal than at $\theta_{\rm c.m.} = 90°$. Consequently, we observe a systematic reduction in the values of $\langle E_t \rangle$ for all particle types in the upper panel of Figure 4.4 compared to those in the lower panel of this figure.

To examine more thoroughly the impact parameter dependence of $\langle E_t \rangle$, we present in Figure 4.5 the mean transverse kinetic energy for the different particle types plotted versus the reduced impact parameter at four incident beam energies. Again the data are for ^{40}Ar+^{45}Sc reactions at $\theta_{\rm c.m.} = 90° \pm 15°$ and the errors shown are statistical. The values of $\hat{b} = b/b_{max}$, as listed in Table 3.1, correspond to the upper limit of each reduced impact parameter bin. Up to a projectile energy of 55 MeV/nucleon the data exhibit a constant value of $\langle E_t \rangle$ for each particle type, while above 55 MeV/nucleon a monotonic rise in the values of $\langle E_t \rangle$ occurs as the impact parameter becomes smaller. The rising value of $\langle E_t \rangle$ with increasing centrality becomes progressively stronger at higher bombarding energies (the heavier fragments are missing in the largest $\hat{b}$ bin, because of the forward focusing effects in fixed target experiments). This result is in qualitative agreement with previous data [Doss88], and BUU model calculations [Dani92] for light particle emission (p, d, t, and ^{3}He) from collisions for heavier entrance channels at higher beam energies. The authors of those works attributed this phenomenon to collective expansion of a blast of light fragments in central collisions.

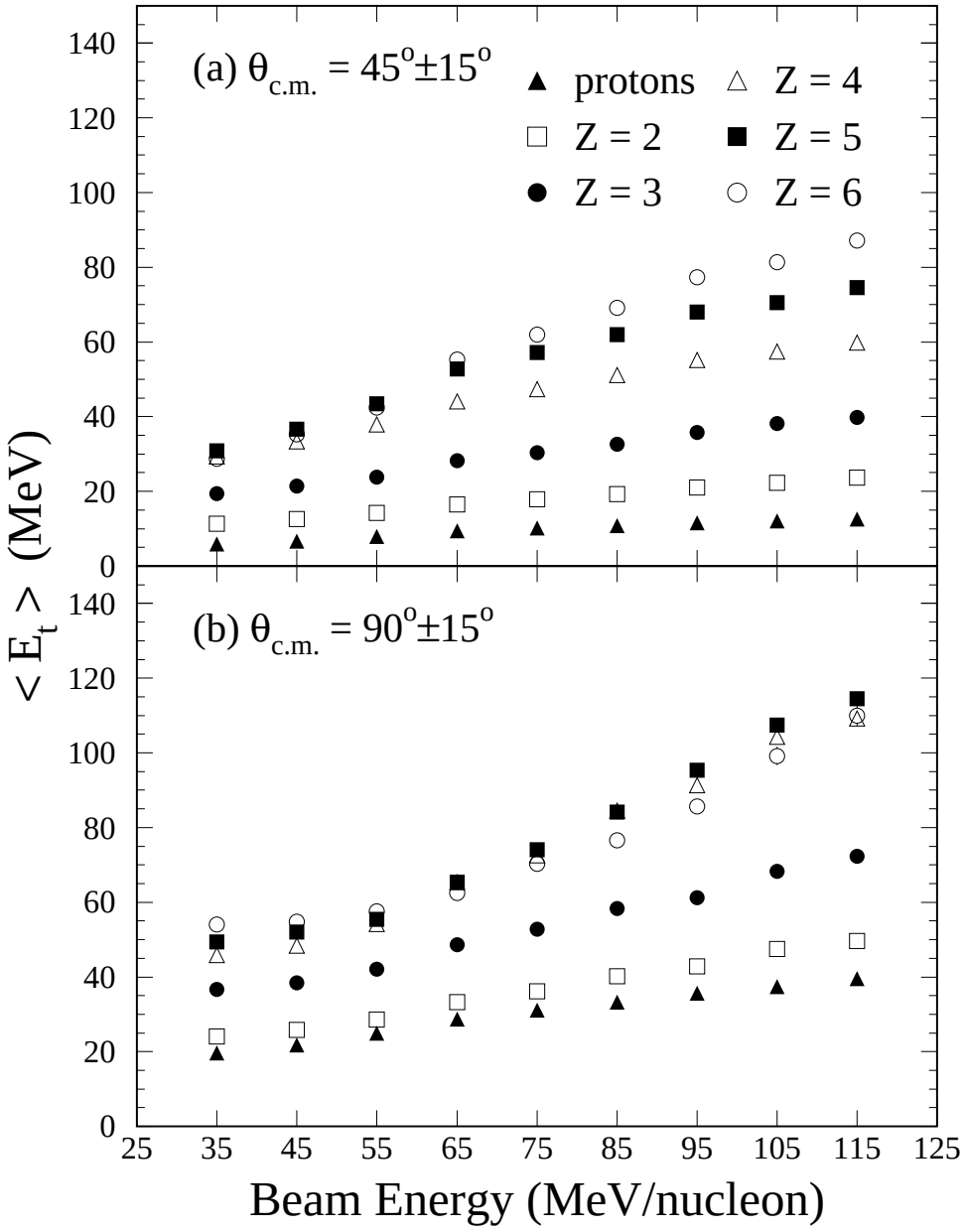

Figure 4.4: Mean transverse kinetic energy of fragments from central ^{40}Ar+^{45}Sc collisions versus incident beam energy for two c.m. polar angle bins. The upper (lower) panel is for $\theta_{\mathrm{c.m.}} = 45° \pm 15°$ ($\theta_{\mathrm{c.m.}} = 90° \pm 15°$).

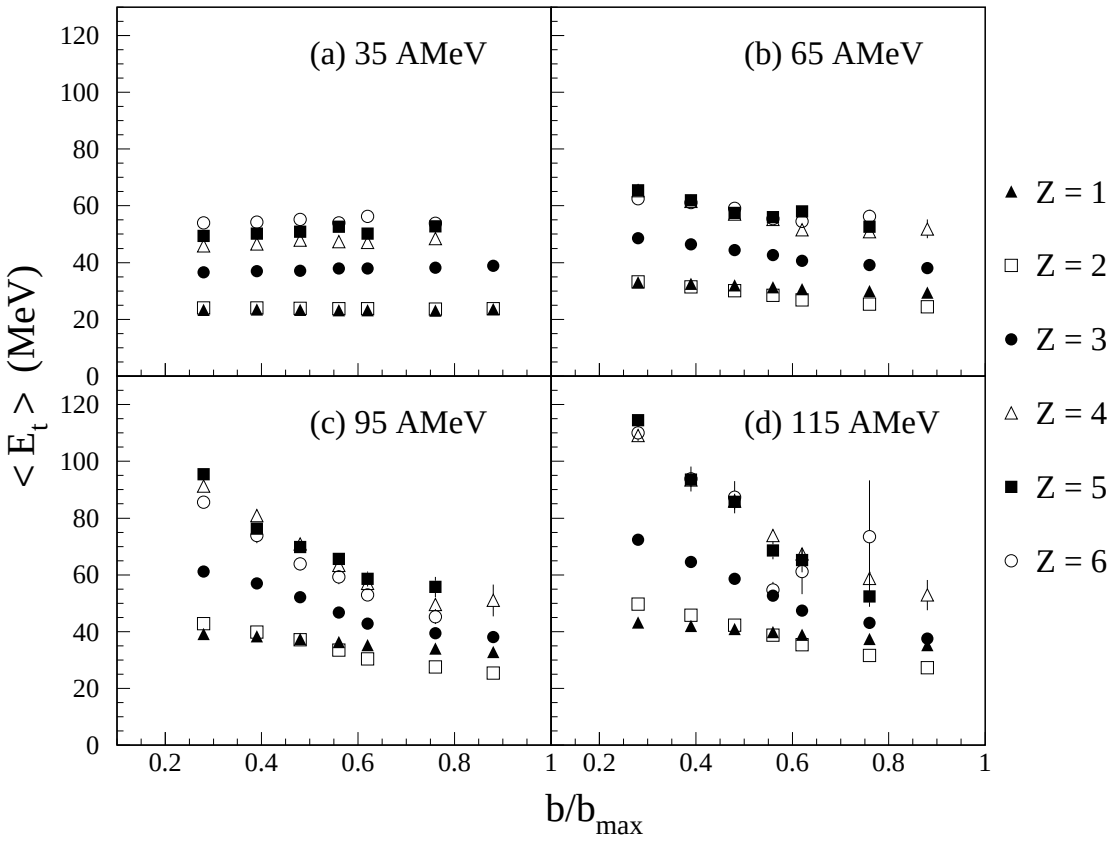

Figure 4.5: Mean transverse kinetic energy of fragments from ^{40}Ar+^{45}Sc reactions at polar angles $\theta_{\mathrm{c.m.}} = 90° \pm 15°$ versus the reduced impact parameter at four incident beam energies.

4.3 BUU Model

To estimate the magnitude of the mean transverse kinetic energy imparted to the fragments in the nuclear disassembly process, we used a Boltzmann-Uehling-Uhlenbeck (BUU) model calculation [Baue86, Baue88]. In this model the nucleons are assumed to interact with a collectively generated mean field and with each other through two-body collisions which respect the Pauli exclusion principle. All the calculations were performed at a fixed impact parameter of $b = 0$ for an EOS with compressibility $\kappa = 240$ MeV except where noted, and were not corrected for effects due to detector acceptance. Calculations with small finite impact parameters ($b \approx 0.01$ fm) show negligible difference with those for perfectly central collisions ($b = 0$). Shown in Figure 4.6 for central ^{40}Ar+^{45}Sc reactions at four bombarding energies are results for $\langle E_t \rangle$ of the nucleons as a function of time [Pak96b]. The upper (lower) panel shows the mean transverse kinetic energy per nucleon when only particles that move in a medium whose density is less (greater) than one eighth of the normal nuclear density $\rho_0 = 0.168$ fm^{-3} were included in the calculation. For particles in medium with $\rho/\rho_0 < \frac{1}{8}$, we found collisions are no longer sufficiently frequent to allow conversion of thermal and compressional energy into collective radial flow, so that freeze-out has occurred for these nucleons. The dashed line in the lower panel represents the value of two thirds the Fermi energy of the initial configuration of the system before the collision occurs.

The results displayed in Figure 4.6 clearly show that in either case the maximum value of $\langle E_t \rangle$ increases as the projectile energy increases. The present calculations are consistent with a scenario [Baue93] in which the maximum density is reached when the colliding nuclei completely stop within each other and the maximum flow energy is attained shortly afterwards. This is demonstrated in Figure 4.7 where the

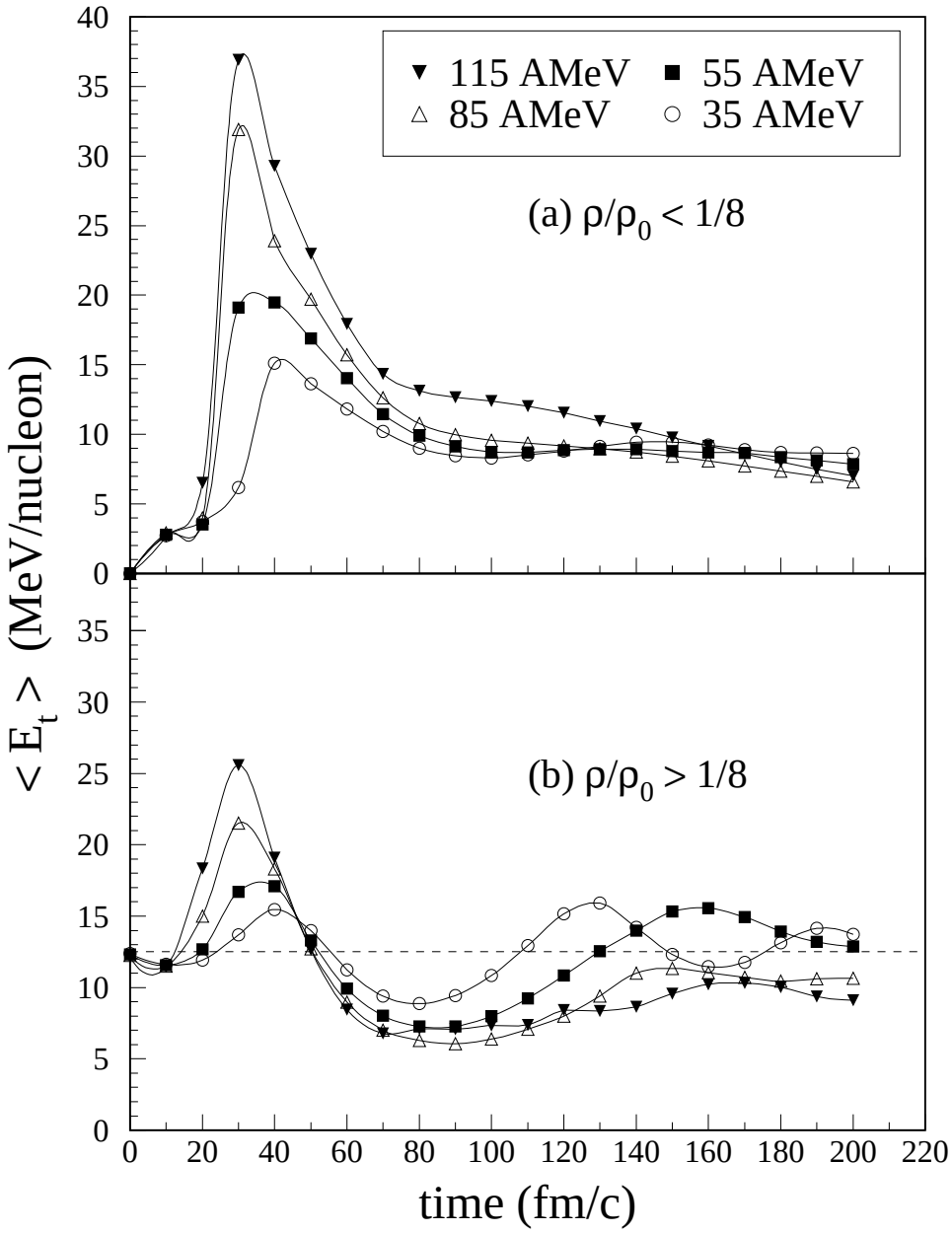

Figure 4.6: Mean transverse kinetic energy per nucleon for ^{40}Ar+^{45}Sc reactions at four bombarding energies as a function of time from BUU theory [Baue86, Baue88]. The calculations are at a fixed impact parameter of $b = 0$ for a medium EOS. The upper (lower) panel shows $\langle E_t \rangle$ when only particles that move in a medium whose density is less (greater) than one eighth of the normal nuclear density are included in the calculation.

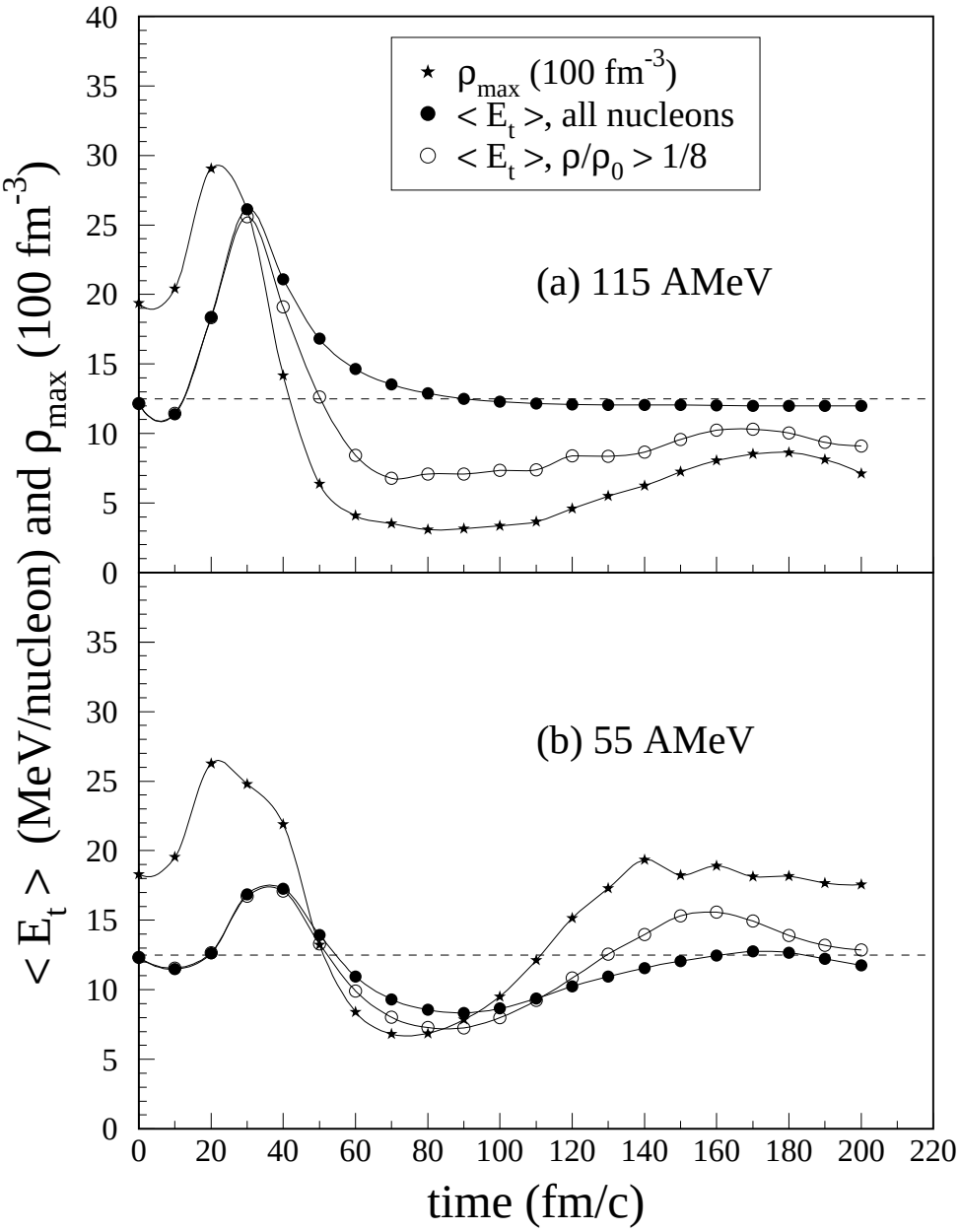

Figure 4.7: Maximum density (solid stars) attained in ^{40}Ar+^{45}Sc reactions at 115 (55) MeV/nucleon as a function of time from BUU theory is shown in the upper (lower) panel. Also shown are mean transverse kinetic energy per nucleon when all nucleons are included (solid circles), and when only particles that move in a medium whose density is greater than one eighth of the normal nuclear density are included (open circles) in the calculation.

maximum density ρ_{max} of the colliding nuclei is plotted as a function of time for two projectile energies (solid stars). The values of ρ_{max} are given in units of 100 fm^{-3} so that they have the same scale as $\langle E_t \rangle$ also shown in this diagram (circles). A higher projectile energy results in more compressional energy stored during the collision, which is consequently released as radial flow energy. The rate of this energy transfer is very rapid with the entire process occurring in less than 60 fm/c. This tends to rule out evaporative decay processes as the source of intermediate mass fragment production [Barz91, Baue93] at these projectile energies. Figure 4.7 also demonstrates that the maximum values of $\langle E_t \rangle$ are the same whether only particles in medium with $\rho/\rho_0 > \frac{1}{8}$ are considered (open circles) or all particles are included (solid circles) in the calculation, similar to what has been previously reported [Baue93].

Another interesting feature present in the lower panel of Figure 4.7 is the kink in ρ_{max} at time $\approx$ 40 fm/c, compared with the smooth drop in the maximum density shown in the upper panel. This occurs because in the BUU model the radially expanding density wave stalls [Baue92] in perfectly central ^{40}Ar+^{45}Sc collisions at a beam energy of 55 MeV/nucleon, while at 115 MeV/nucleon the outflowing matter more promptly disintegrates. This gives rise to the transient formation of bubble and toroid shapes in the density profiles [Baue92, More92] of the disassembling system produced by the model at a beam energy of 55 MeV/nucleon. A major challenge still left in experimental heavy-ion reactions is to unambiguously measure the signatures produced by the break-up of these non-compact geometries.

Although the maximum density attained by the colliding nuclei was sensitive to the nuclear EOS (a larger compression is achieved for a soft EOS than a stiff EOS), the EOS had only a minor influence on the mean transverse kinetic energy as found elsewhere [Lisa95]. The Coulomb interaction was also found to have only a small effect on the maximum value of $\langle E_t \rangle$ for the ^{40}Ar+^{45}Sc system. This is shown in

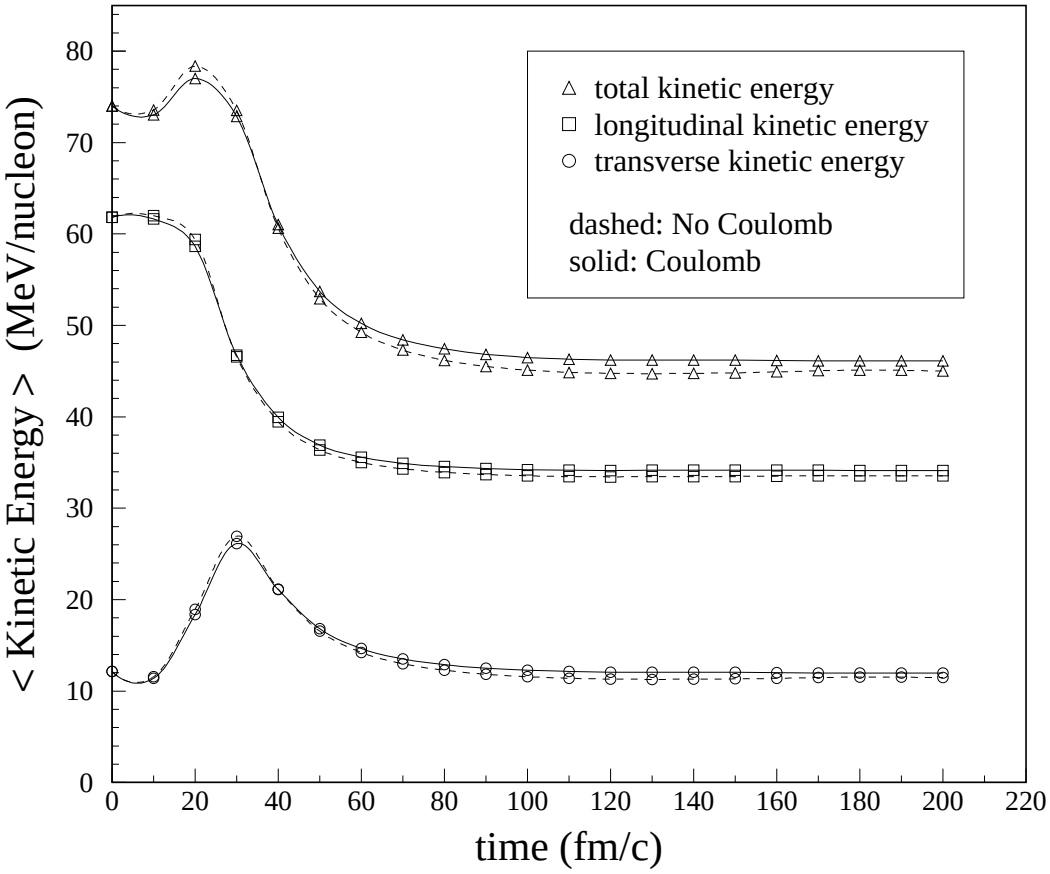

Figure 4.8: Mean total kinetic energy (open triangles) per nucleon, and its longitudinal (open squares) and transverse (open circles) components plotted as a function of time for 115 MeV/nucleon ^{40}Ar+^{45}Sc collisions. The solid (dashed) lines are for a BUU calculation which included (excluded) the Coulomb repulsion.

Figure 4.8 where $\langle E_t \rangle$ per nucleon (open circles) is plotted as a function of time for 115 MeV/nucleon ^{40}Ar+^{45}Sc reactions. The solid (dashed) lines are for a BUU calculation which included (excluded) the Coulomb repulsion. The height of the first peak only slightly diminishes due to the greater repulsion, which allowed less compression during the initial stages of the collision. Also apparent in Figure 4.8 is the stopping of the projectile by the target. The drop in the mean longitudinal kinetic energy per nucleon (open squares) coincides with the build-up of the mean transverse component, as the incident beam energy is transformed into this mode due to nuclear damping. The mean total kinetic energy (open triangles) per nucleon is shown for completeness. The release of this stored compression energy as collective radial expansion will now be used to account for the discrepancy in the temperatures extracted for different fragment types at the end of Chapter 3.

4.4 Comparison to BUU and WIX

To compare the data to the values of $\langle E_t \rangle$ predicted by the BUU model calculations, we replot the lower panel of Figure 4.2 rescaling the vertical axis to MeV per nucleon as shown in Figure 4.9 [Pak96b]. This is done because our BUU calculations involve only nucleons, *i.e.,* no fragments with $A > 1$ are produced in the calculations. The data for deuterons and tritons are also displayed. The solid triangles in Figure 4.9 are the maximum values of $\langle E_t \rangle$ at the respective bombarding energies extracted from the top panel of Figure 4.6 for the case where only particles in medium with $\rho/\rho_0 < \frac{1}{8}$ are included in the calculation. There is surprising agreement between these points and the data for the protons (open stars). To extract the maximum values of $\langle E_t \rangle$ for the case where only particles in medium with $\rho/\rho_0 > \frac{1}{8}$ are considered, two thirds of the value of the Fermi energy for the initial configuration (dashed line) is subtracted from the value of the height of the first peak for each projectile energy shown in the lower

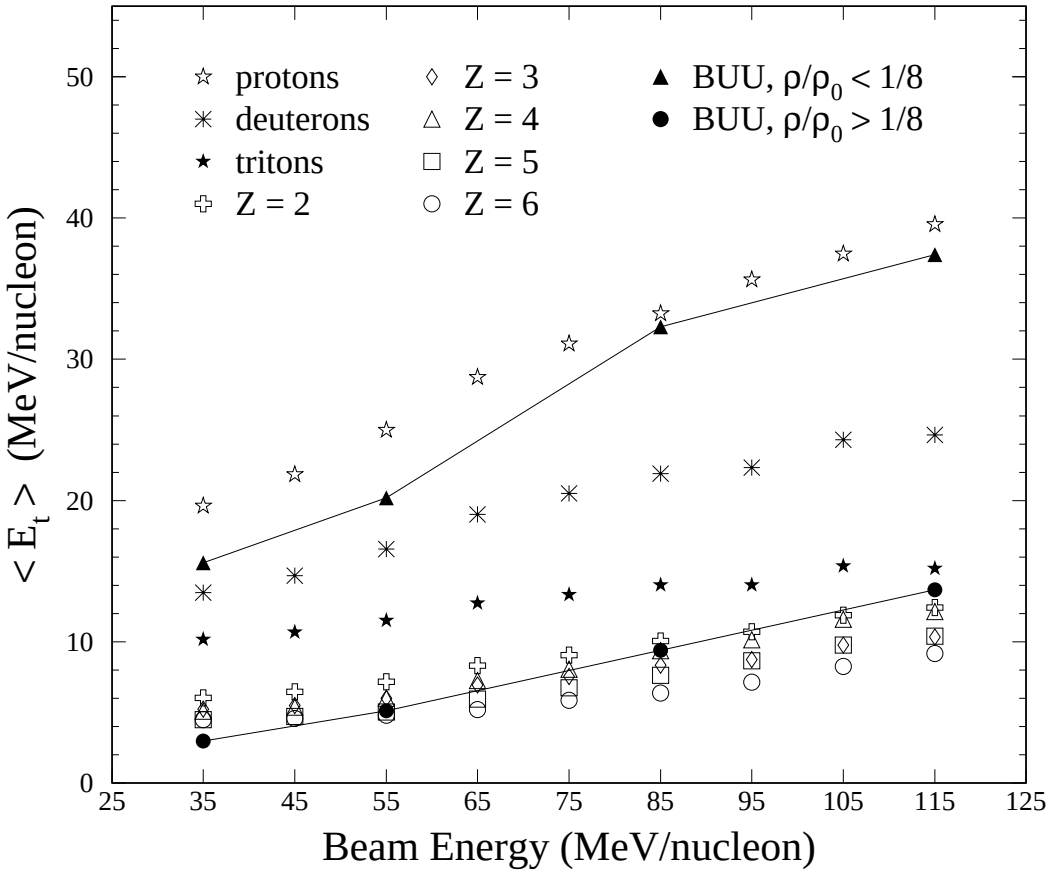

Figure 4.9: Mean transverse kinetic energy per nucleon of fragments from central ^{40}Ar+^{45}Sc collisions at polar angles $\theta_{\rm c.m.} = 90° \pm 15°$ versus incident beam energy compared with predictions of BUU model calculations. The lines are included to guide the eye.

panel of Figure 4.6. These values, plotted as solid circles in Figure 4.9, show good agreement with the data for fragments with $Z \geq 2$. Although our BUU calculation can not produce fragments, we are still able to delineate the approximate limits on the value of $\langle E_t \rangle$ as a function of incident beam energy reasonably well. This lends further support to the interpretation of the disassembly mechanism garnered from the model, as outlined in Section 4.3.

Using our measured values of $\langle E_t \rangle$, we calculate the radial expansion velocity β_{flow} for the heavier fragments at the highest beam energy where the flow signal is the most pronounced. The mean transverse kinetic energy may be written as:

$$\begin{aligned} \langle E_t \rangle &= \frac{2}{3}\langle E_{thermal} \rangle + \langle E_{radial} \rangle \\ &= T + \langle E_{radial} \rangle, \end{aligned} \tag{4.1}$$

because cross terms between the collective and the random thermal components vanish on the average [Kund95]. The sum of the initial expansive flow and the Coulomb induced energy can be non-relativistically approximated [Hsi94, Pogg95] by:

$$\begin{aligned} \langle E_{radial} \rangle &= E_{flow} + E_{Coulomb} \\ &= \frac{3}{5}\left[\frac{1}{2} m_f c^2 \beta_{flow}^2 + \frac{Z_f(Z_S - Z_f)e^2}{R_S}\right], \end{aligned} \tag{4.2}$$

where subscript S refers to the source and f to the fragment type. In this expression for self-similar radial expansion, *i.e.,* a collective velocity field proportional to the radial distance $\mid \mathbf{r} \mid$, a spherical participant volume was assumed which attains its maximum velocity $c\beta_{flow}$ at the surface $r = R_S$. The radial flow and Coulomb repulsion for particles emitted from this spherical volume of uniform density cannot be separately distinguished without isotopic resolution.

As the beam energy increases, it is reasonable to expect from Equation 4.1 that the correlations from collective motion will be reduced by the greater thermal motion

generated in these more energetic collisions. On the contrary, the flow energy is an increasingly larger fraction of the fragment energy while the thermal energy is less important [Doss87]. This is under the assumption that the thermal energy was equally partitioned for the equilibrated system of nucleons and fragments at a fixed freezeout temperature. The thermal energy per nucleon for a fragment of mass A therefore has a $1/A$ dependence. The quantity E_{flow} in Equation 4.2 resulting from the initial compression during these central collisions should roughly scale as A (flow energy per nucleon is independent of A). Figures 4.2 and 4.5 demonstrate that larger mass fragments exhibit enhanced radial flow at higher beam energies.

In Equation 4.2 we have assumed $Z_S = 39$ and $R_S = 8$ fm, representing the maximum Coulomb repulsion from the equilibrated compound source. The expansion velocities determined in the present calculation are insensitive to the difference in source size with those reported from fragment coalescence [Llop95c]. A temperature parameter of $T = 28$ MeV for an incident beam energy of 115 MeV/nucleon was extracted from a single-source Maxwell-Boltzmann (MB) fit to the proton energy spectrum for central collisions at $\theta_{\rm c.m.} = 90^\circ \pm 15^\circ$ as outlined in Section 3.4. Protons were used to determine this temperature because the radial flow component has been shown to least affect the energy spectrum for the light particle species [Siem79, Dani92, Barz91, Baue93]. Under these assumptions we find a radial expansion velocity for the Li, Be, B, and C fragments of $\beta_{flow} \approx 0.15 \pm 0.03$ (the accuracy achieved is about 20%).

Repeating this procedure with the values of $\langle E_t \rangle$ predicted by our BUU model calculation for the case where only particles in medium with $\rho/\rho_0 > \frac{1}{8}$ are considered, we calculate $\beta_{flow} \approx 0.18 \pm 0.02$ for these heavier fragments. These values for T and β_{flow} are also in reasonable agreement with the values we extracted from single source fits which include collective expansion to the kinetic energy spectra for these fragment

types given by [Siem79, Pogg95, Lisa95]:

$$\frac{d^2N}{d\Omega dE} \propto p \exp\left(-\frac{\gamma_{flow}E}{T}\right)\left[(\gamma_{flow}E+T)\frac{\sinh\alpha}{\alpha} - T\cosh\alpha\right]. \qquad (4.3)$$

In this expression E and p are the total energy and momentum of the particle in the center-of-mass frame, $\gamma_{flow} = (1-\beta_{flow}^2)^{-1/2}$, and $\alpha = (\gamma_{flow}\beta_{flow}p/T)$. We found our data to be rather insensitive to this parameterization scheme such that a fairly wide range of T and β_{flow} resulted in reasonable fits, and we could not solely rely on this method to extract these quantities. This could be due to a non-uniform radial velocity profile for the actual decaying source in our system. In Table 4.1 we list for Be fragments from ^{40}Ar+^{45}Sc reactions at each projectile energy: the measured mean transverse kinetic energy; the temperature from MB fits to the proton spectra; the calculated radial expansion velocity; and the relative fraction of the radial flow energy given by $E_{flow}/\langle E_t\rangle$. A value of 15 MeV was used for the Coulomb repulsion of the

Table 4.1: Radial flow parameters.

E_{beam} (AMeV)	$\langle E_t\rangle$ (MeV)	T (MeV)	β_{flow} (v/c)	$E_{flow}/\langle E_t\rangle$ (%)
115	109	28	0.16	61
105	104	26	0.16	61
95	91	25	0.14	56
85	84	23	0.14	55
75	73	21	0.12	51
65	65	20	0.11	46
55	54	17	0.09	41
45	48	14	0.09	42
35	46	12	0.09	41

$Z = 4$ fragments in the determination of these radial flow quantities. Similar trends in the values of these parameters are present in the data for the other fragments types with $Z \geq 2$. The percentages reported in the last column of this table are additional

evidence that radial flow is a major contribution to the energy dissipation in the disassembly process of excited nuclear matter.

For a value of 50% in the relative fraction of the radial flow energy, we have simulated collective radial expansion of light fragment emission in heavy-ion collisions using the statistical multifragmentation model called WIX [Rand93]. The WIX code generated events in which a single source de-excites via explosion and evaporation with this specified collective expansion energy at freeze-out. The calculations included the Coulomb interaction between fragments, and the default parameters were used to characterize the level density, explosion threshold energy, and spacial configuration of the decaying source. The simulated events were analyzed with the same radial flow routine as for the actual data. In Figure 4.10 we show a comparison between data and simulation for the excitation functions of the mean transverse kinetic energy for various light fragment types. The open symbols are data from central ^{40}Ar+^{45}Sc reactions at polar angles $\theta_{\rm c.m.} = 90^\circ \pm 15^\circ$ (as in the lower panel of Figure 4.2). The solid symbols are the predictions of the WIX multifragmentation model assuming half the available energy of the disassembly process is associated with radial flow. All effects of the experimental acceptance were included in these filtered simulations (low-energy thresholds, target shadowing, double hits, etc.). The errors shown are statistical, and the dashed lines are included only to guide the eye. Similar trends are present in the filtered simulation of the other particle types not shown for clarity. The agreement between data and simulation in Figure 4.10 demonstrates that the measured radial flow is not an artifact of our detector acceptance or analysis method, and substantiates our claim that approximately half of the emitted particle's energy originates from collective radial expansion [Pak96b].

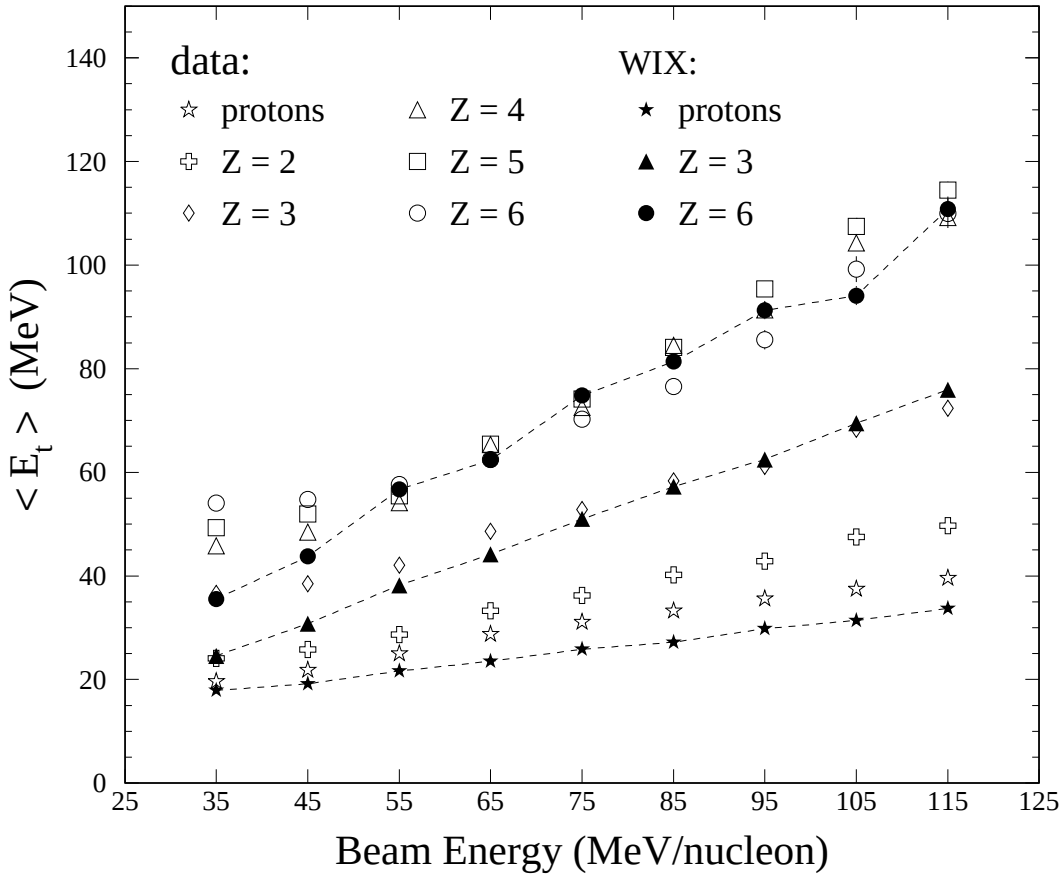

Figure 4.10: Mean transverse kinetic energy of fragments from central ^{40}Ar+^{45}Sc reactions at polar angles $\theta_{\mathrm{c.m.}} = 90° \pm 15°$ versus incident beam energy compared with predictions of WIX model [Rand93] calculations assuming half the available energy is associated with radial flow. The lines are included to guide the eye.

4.5 Conclusions

In summary, we have investigated collective radial flow of light fragments for the system ^{40}Ar+^{45}Sc at beam energies in the range E = (35 - 115) MeV/nucleon using the MSU 4π Array. The mean transverse kinetic energy of the different fragment types increases with event centrality, and increases as a function of the incident beam energy. Comparison of our measured values of $\langle E_t \rangle$ shows agreement with predictions of BUU model and WIX multifragmentation model calculations. The radial flow extracted from $\langle E_t \rangle$ accounts for approximately half of the emitted particle's energy for the heavier fragments ($Z \geq 4$) at the highest beam energy studied.

Chapter 5

Directed Transverse Flow

5.1 Introduction

A major goal in the field of heavy-ion reaction dynamics is the derivation of an equation of state (EOS) for nuclear matter. The study of collective flow in these nucleus-nucleus collisions can provide information about the nuclear EOS [Stoc86, Dani88, Goss89, Gutb89, Peil89, Pan93, Peil94]. Collective transverse flow in the reaction plane disappears at an incident energy, termed the balance energy E_{bal} [Ogil90], where the attractive scattering dominant at energies around 10 MeV/nucleon balances the repulsive interactions dominant at energies around 400 MeV/nucleon [Moli85b, Bert87, Krof89, Ogil89b, Sull90, Zhan90, Krof91, Krof92, Shen93, Laur94, Buta95]. We recently completed a systematic study of the disappearance of flow for central collisions in symmetric entrance channels [West93], which showed that E_{bal} scales as $A^{-1/3}$ where A is the mass of the combined projectile-target system (see Figure 1.2). The general trend of this result, which was reproduced by Boltzmann-Uehling-Uhlenbeck (BUU) model [West93, Klak93] and Landau-Vlasov (LV) model [dlMo92] calculations at a fixed impact parameter, demonstrated that E_{bal} is insensitive to the compressibility of the EOS but sensitive to the in-medium nucleon-nucleon cross section. This is an example of how the information resulting from the study of collective flow can

be used to constrain the parameters in the nuclear EOS.

The importance of the role of the impact parameter in the determination of the disappearance of flow has been both theoretically [Bert87, dlMo92, Klak93] and experimentally recognized [Sull90]. As two nuclei collide, the pressure and density increase in the interaction region, *i.e.,* compression of the nuclear matter occurs in the participant volume [Sche74, Gutb89]. At nonzero impact parameters there is anisotropy in the pressure, resulting in a transverse flow of nuclear matter in the directions of lowest pressure (see Figure 1.4). In symmetric collisions the compressed midrapidity participant volume is expected to decrease in size with increasing impact parameter. Thus a similar scaling effect as for the mass dependence is also at work here, *i.e.,* a larger incident energy is required to compensate for the effects of the mean field in more peripheral collisions [Klak93]. From trends present in the data for the reverse kinematic reaction ^{40}Ar+^{27}Al [Sull90], we expect E_{bal} to increase as the impact parameter increases. These expectations are also based on theory, because predictions from BUU [Bert87] and LV [dlMo92] model calculations demonstrate the impact parameter dependence of directed transverse momentum flow (see Figure 1.9). Using the transverse momentum analysis method [Dani85], we show that flow can be determined from midrapidity participant fragments for even relatively peripheral collisions. The impact parameter dependence of the balance energies extracted from the measured flow values agrees with predictions from Quantum Molecular Dynamics (QMD) model [Soff95] calculations.

5.2 Preliminary Results

Before directly proceeding to the transverse momentum analysis to extract balance energies we shall briefly present a few preliminary results in this section. These results

are meant to convince the reader that collective transverse flow in the reaction plane can be well measured with the MSU 4π Array, as expected from simulations for the ^{40}Ar+^{45}Sc system at the beam energies in this experiment. For the purpose of comparison to our previous work [West93], all the results presented in this chapter are for Ball-2 data (see Section 3.2) except where noted. All the results presented in this section are for an incident beam energy of 45 MeV/nucleon, because a unmistakably strong signal for directed transverse flow is expected at this projectile energy [West93].

Once the impact parameter of the event has been assigned (as outlined in Section 3.2), and the reaction plane for a particular particle of interest (POI) in the event has been calculated (as outlined in Section 3.3), the transverse momentum of the POI in the reaction plane can be evaluated. The directed or in-plane transverse momentum is simply the projected component of the total transverse momentum of the POI into the found reaction plane. To quantify how directed transverse momentum varies along the direction of the beam axis, the mean transverse momentum in the reaction plane is plotted as a function of the center-of-mass (c.m.) rapidity. From this plot the flow is extracted by fitting a straight line to the data over the midrapidity region. The slope of this line is defined as the directed transverse flow, which is a measure of the amount of collective momentum transfer in the reaction.

A simple method to determine the reaction plane not already previously discussed in Section 3.3 is to choose the projectile-like-fragment (PLF) as the POI. Because the intial momentum vector of the projectile lies in the true reaction plane, it is physically reasonable from momentum conservation to expect that there exists a correlation between this reaction plane and a large remanent of the original bombarding particle. Events were selected in which a PLF (here $Z \geq 8$) was measured in the HRA. The azimuthal angle of the PLF is then taken to be the azimuthal angle of the reaction plane (the forward flow side coincides with the PLF). The projection of the transverse

momenta into this reaction plane is evaluated for the remaining particles of the event.

The open squares in Figure 5.1 are the result of plotting the mean fraction of the transverse momentum in the reaction plane determined using the PLF $\langle p_x/p_t \rangle$ for protons versus the reduced c.m. rapidity $(y/y_{proj})_{c.m.}$ for an impact-parameter-inclusive data set [Pak95]. Reduced quantities were used here as done in previous

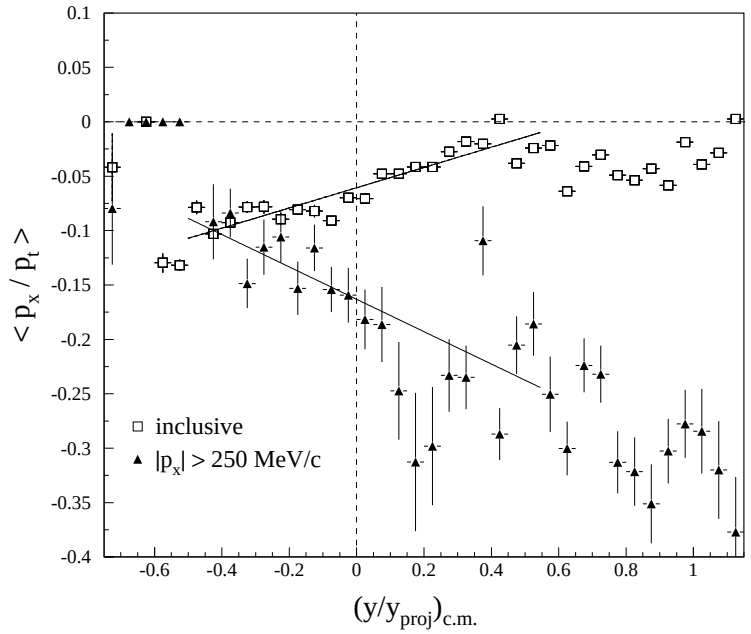

Figure 5.1: Mean fraction of the transverse momentum in the reaction plane determined using the PLF for protons versus the reduced c.m. rapidity for 45 MeV/nucleon ^{40}Ar+^{45}Sc reactions. The open squares are for an inclusive data set, while the solid triangles are the result of applying a cut that allows only protons with transverse momenta in the reaction plane greater than 250 MeV/c. The straight lines are fit in the region -0.5 $\leq (y/y_{proj})_{c.m.} \leq$ 0.5.

studies on directed transverse flow by the MSU 4π Group [Ogil89b, Ogil90, Krof91], where p_t is the fragment's total transverse momentum and y_{proj} is the c.m. rapidity of the projectile. The data, which exhibit the characteristic "S-shape" associated with flow, are offset from the origin because no recoil correction was applied in this case. The straight line is a fit in the midrapidity region -0.5 $\leq (y/y_{proj})_{c.m.} \leq$ 0.5.

The solid triangles in Figure 5.1 are the result of applying a momentum cut to

suppress the contribution to the directed flow from excited spectator matter. This cut allows only protons with transverse momenta in the reaction plane greater in absolute value than 250 MeV/c, effectively eliminating the protons emitted from the "cooler" target and projectile spectators. We show in Figure 5.2 the effect of this gating condition on the transverse momentum distribution for protons in the reaction plane for an inclusive data set. The deficiency of counts at the center of this distribution is an

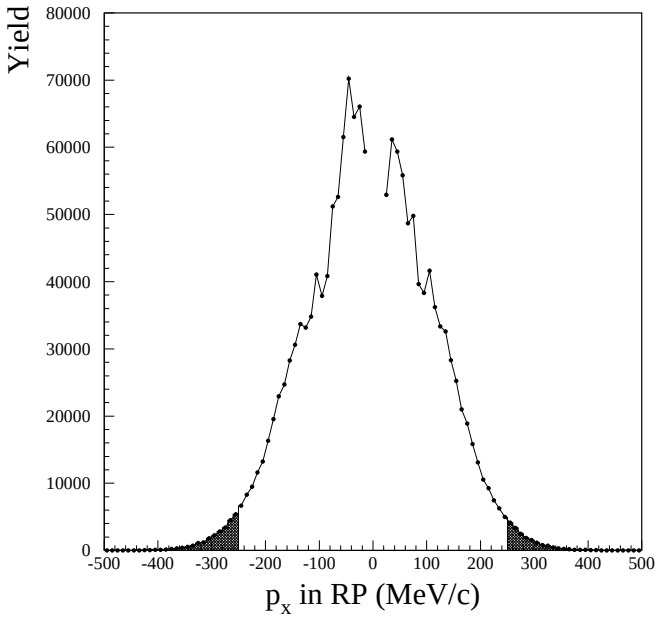

Figure 5.2: Transverse momentum distribution in the reaction plane determined using the PLF for protons from 45 MeV/nucleon ^{40}Ar+^{45}Sc reactions. The shaded area represents protons with transverse momenta in the reaction plane greater in absolute value than 250 MeV/c.

artifact of the detector low-energy thresholds [Wils91a]. Following this cut, the slope of the straight line fit to the solid triangles in Figure 5.1 is negative. Thus protons emitted from the "hotter" midrapidity participant source are preferentially deflected by the mean field away from the PLF for this projectile energy. These conclusions are consistent with those for the ^{12}C+^{12}C data at 50 MeV/nucleon [Wils91a], which is a similar relatively light system measured below the balance energy (E_{bal} = 122

MeV/nucleon for $^{12}C+^{12}C$ [West93]). The method of using the PLF to calculate the reaction plane is not applicable to central collisions, and also suffers from the drawback of low statistics (because a PLF is required in the event). Consequently this technique is not used in the remainder of this thesis. The purpose here is to reproduce a result similar to a previous flow analysis [Wils91a] for more peripheral collisions.

Figure 5.3 demonstrates the acceptance of the MSU 4π Array for measuring directed collective transverse flow. The transverse momentum in the reaction per nucleon p_x/A for all POI is plotted versus the reduced c.m. rapidity for 45 MeV/nucleon $^{40}Ar+^{45}Sc$ reactions. Here the reaction plane has been determined using the azimuthal correlation method with the recoil correction given by Equation 3.11. The directed transverse momentum p_x has been normalized by the particle mass number A because we are including all fragments as the POI. This can be done because of the correlation between reaction planes calculated with different particle types as the POI (shown in Section 3.3). Clearly a target (projectile) source is present at a reduced c.m. rapidity $\hat{y} = (y/y_{proj})_{c.m.}$ = -1.0 ($\hat{y} = 1.0$). The streaks appearing to emanate from the target are due the granularity of the MSU 4π Array, corresponding to azimuthal rings of detectors. Careful examination will reveal a slight imbalance in the number of counts in the histogram near the projectile rapidity, which is greater on the positive side of the p_x/A axis (above the horizontal dashed line). The converse is true near the target rapidity, so that a plot of $\langle p_x/A \rangle$ as a function of $(y/y_{proj})_{c.m.}$ results in the "S-shape" characteristic of collective transverse flow in the reaction plane. Figure 5.3 demonstrates the magnitude of the directed collective motion is small relative to the total available c.m. kinetic energy in agreement with previous work at higher beam energies [Doss88, Gutb89].

We have simulated transverse flow in the reaction plane for heavy-ion collisions using the statistical mulifragmentation model FREESCO [Fai83]. The FREESCO

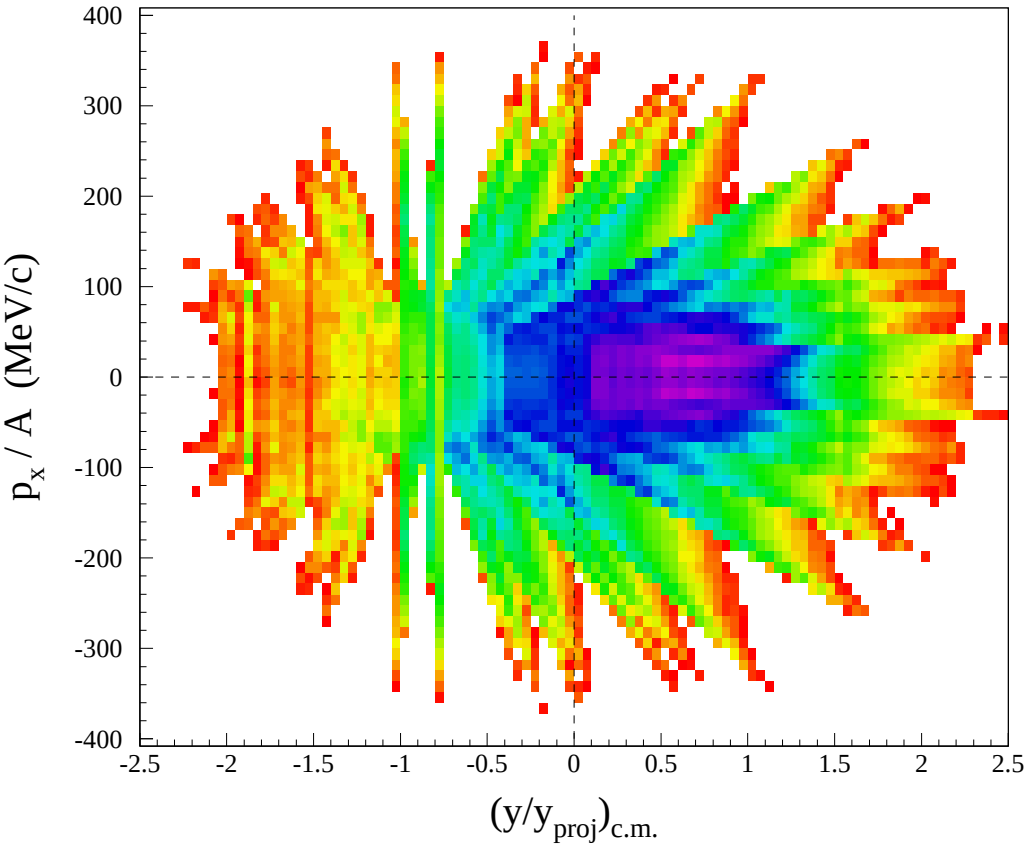

Figure 5.3: Transverse momentum in the reaction per nucleon for all POI versus reduced c.m. rapidity for 45 MeV/nucleon ^{40}Ar+^{45}Sc reactions.

code generated events with a participant source, and two spectator sources for random impact parameters (up to a specified maximum value) using the default parameters to characterize the excitation energy and momenta of these sources. Flow is simulated in FREESCO by dividing the participant into two parts moving in opposite directions in the reaction plane. The simulated events and the actual data were analyzed with the same flow routine using the azimuthal correlation method with the recoil correction to determine the reaction plane. In Figure 5.4 we show a comparison between data and simulation for central collisions at a beam energy of 45 MeV/nucleon [Pak95]. All effects of the experimental acceptance were included in the filtered simulations.

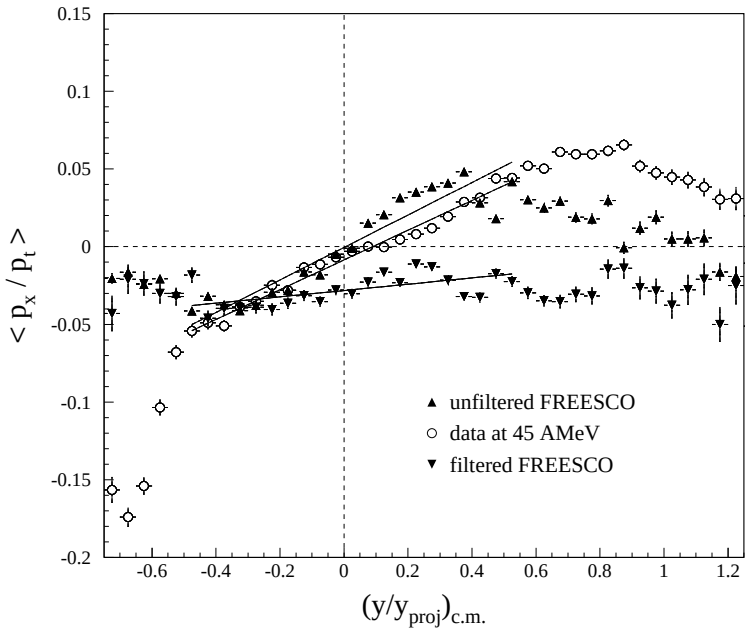

Figure 5.4: Mean fraction of the transverse momentum in the reaction plane for all POI versus the reduced c.m. rapidity for central ^{40}Ar+^{45}Sc collisions at 45 MeV/nucleon. Open circles are data, solid triangles are events generated using FREESCO, and inverted triangles are FREESCO events filtered through our detector acceptance.

The straight lines are fit in the region -0.5 $\leq (y/y_{proj})_{c.m.} \leq$ 0.5. From a comparison of the unfiltered events to the data, it is evident that these results are consistent with the fact that measured flow should be less than the "actual" flow generated by the

code [Sull92]. More importantly, Figure 5.4 demonstrates that the measured flow is not an artifact of our detector acceptance or analysis method.

5.3 Transverse Momentum Analysis

In this section we present results from the transverse momentum analysis [Dani85] for our ^{40}Ar+^{45}Sc data at incident beam energies E = (45 - 115) MeV/nucleon. We shall first examine impact parameter dependence, where the impact parameter of each event analyzed was assigned using the methods outlined in Section 3.2. The mean directed transverse momentum is evaluated for a particular fragment type as the POI in the reaction plane calculation, as stated at the beginning of Section 5.2. In Figure 5.5 we show the mean transverse momentum in the reaction plane $\langle p_x \rangle$ plotted versus the reduced center-of-mass (c.m.) rapidity $(y/y_{proj})_{c.m.}$, where y_{proj} is the c.m. rapidity of the projectile. The data are for fragments with $Z = 2$ from 55 MeV/nucleon ^{40}Ar+^{45}Sc reactions in each of the seven reduced impact parameter bins $\hat{b}$ listed in Table 3.1. Also displayed is the impact-parameter-inclusive result in Panel (h). The errors shown in each panel are statistical; the error on the mean is given for each rapidity bin. The data are fit with a straight line over the midrapidity region -0.5 $\leq (y/y_{proj})_{c.m.} \leq$ 0.5, and the slope of this line is defined as the directed transverse flow.

We next display results for fragments with $Z = 1$ in Figure 5.6, and $Z = 3$ in Figure 5.7, in each of the seven reduced impact parameter bins for 55 MeV/nucleon ^{40}Ar+^{45}Sc collisions. Note the difference in scale on the vertical axis for the three different particle types. For each of the particle types the data exhibit the characteristic "S-shape" associated with directed collective transverse flow, demonstrating the dynamical momentum transfer on opposite sides of the reaction plane (see Figure 1.8).

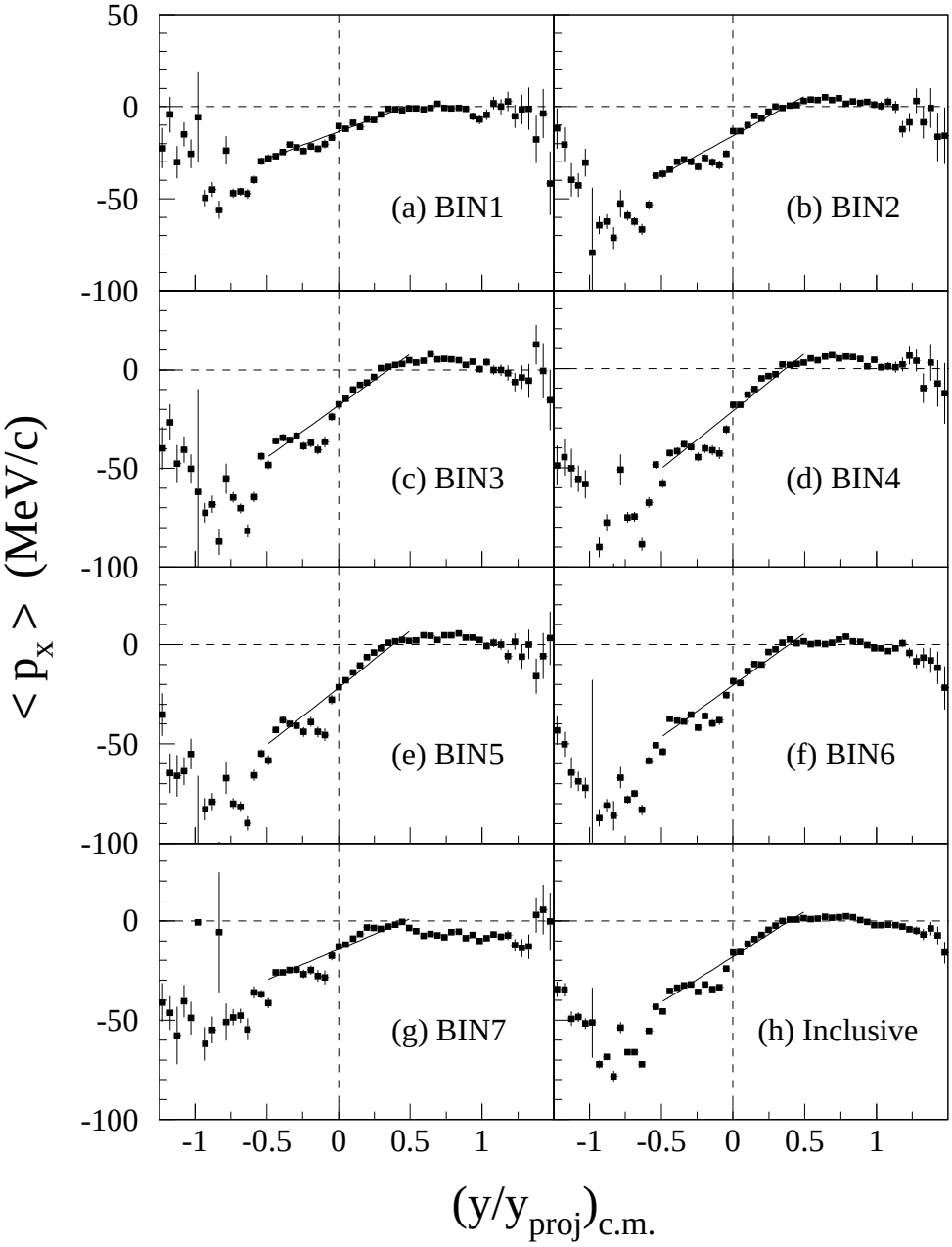

Figure 5.5: Mean transverse momentum in the reaction plane versus the reduced c.m. rapidity for $Z = 2$ fragments in 55 MeV/nucleon ^{40}Ar+^{45}Sc reactions. The reduced impact parameter bins, as indicated in each panel, are listed in Table 3.1. The straight lines are fit in the region -0.5 $\leq (y/y_{proj})_{c.m.} \leq$ 0.5.

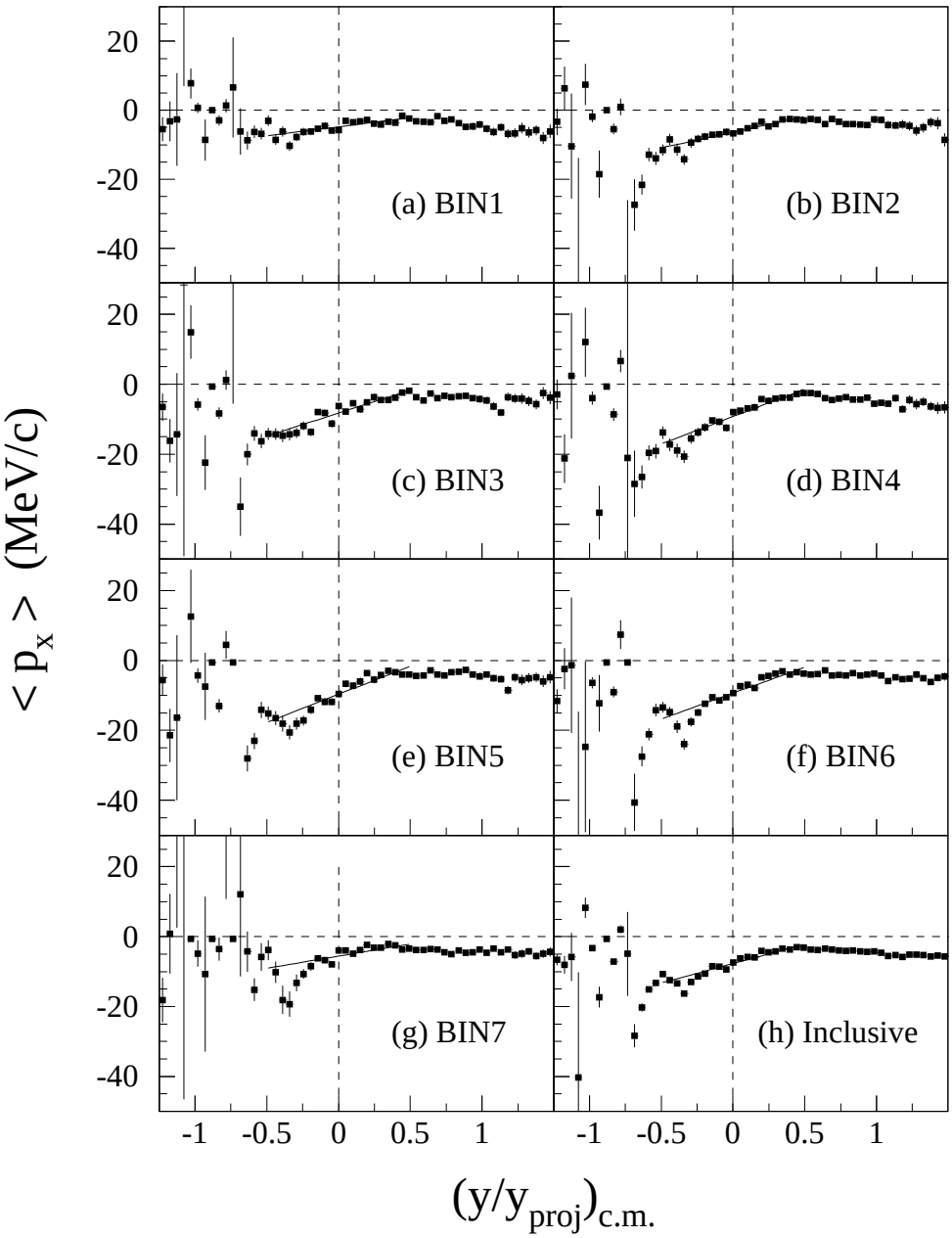

Figure 5.6: Same as Figure 5.5 only for $Z = 1$ fragments.

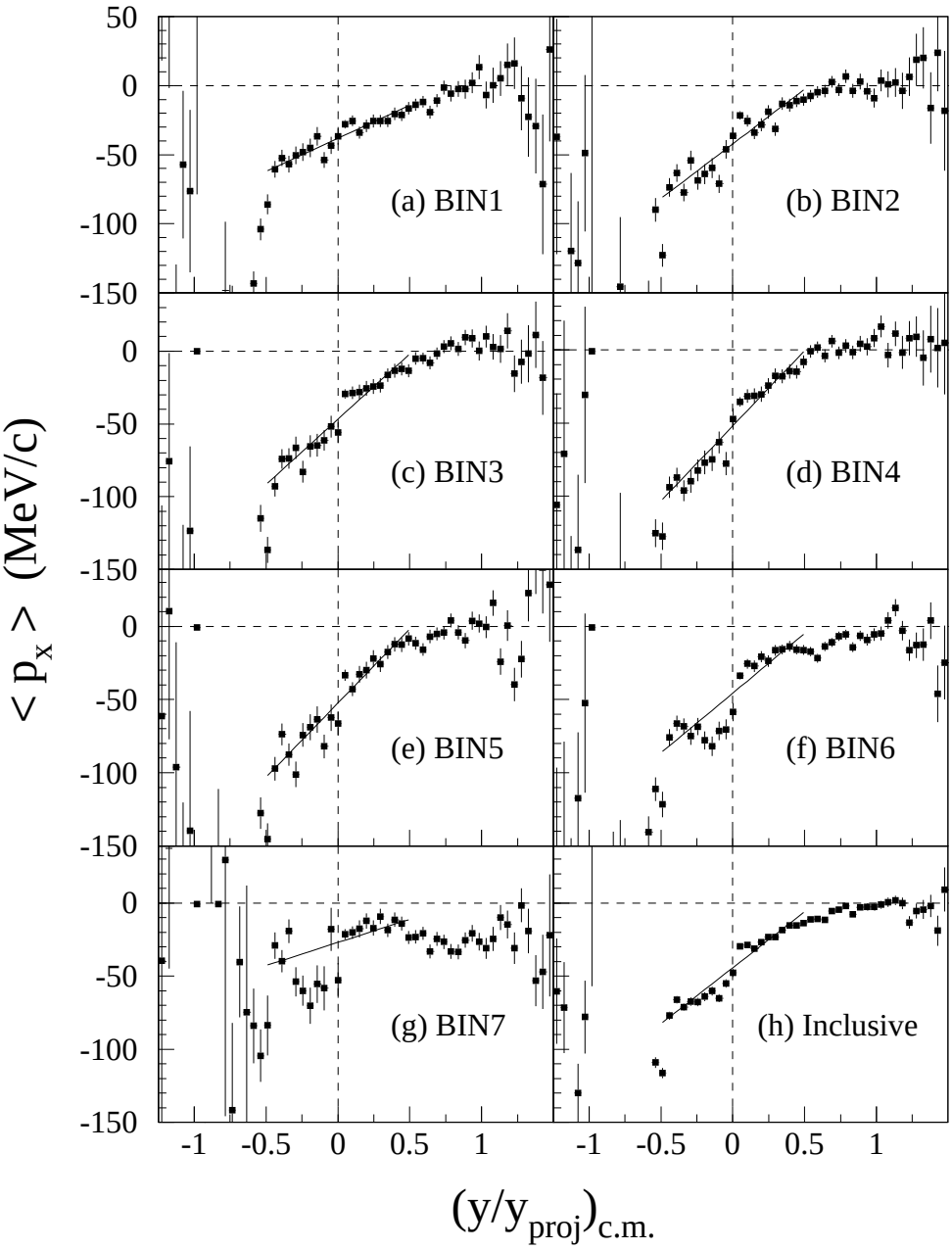

Figure 5.7: Same as Figure 5.5 only for $Z = 3$ fragments.

The directed transverse flow clearly increases as the fragment mass increases for a given impact parameter and incident beam energy, because as the fragment mass increases the flow energy is an increasingly larger fraction of the fragment energy while the thermal energy is less important [Doss87]. This is under the assumption that the thermal energy was equally partitioned for the equilibrated system of nucleons and fragments at a fixed freezeout temperature (as for radial flow in Section 4.4).

The offsets from the origin occur because no recoil correction was applied in the reaction plane calculation for this analysis. We found that a constant fraction of the system mass could not be used in the recoil correction, as given by Equation 3.11, to make the offsets vanish for all impact parameters at a given incident beam energy. We should not expect this to be case, because the system mass in this expression is more correctly viewed as the mass of the interaction volume (participant source), which becomes smaller as the impact parameter increases. Because we are attempting to measure the impact parameter dependence of the directed transverse flow, we did not want to include an *ad hoc* correction factor which strongly depended on this quantity.

As the impact parameter increases in Figure 5.5, the directed transverse flow increases, passes through a maximum, and diminishes for the most peripheral impact parameter bin shown. To see this more directly, we show in Figure 5.8 the transverse flow in the reaction plane as a function of the reduced impact parameter. The open circles are the values of the slope of the linear fits over the midrapidity region shown in Panels (a) - (g) of Figure 5.5. Also displayed are the values of the directed transverse flow for seven other bombarding energies. The errors shown are the statistical errors on the slopes of the linear fits. The systematic error associated with the range of the fitting region is +3 MeV/c and -1 MeV/c. This systematic error results from the competing effect between the better statistics produced by using more points for the linear fit, and the variation in the extracted value of the flow resulting from

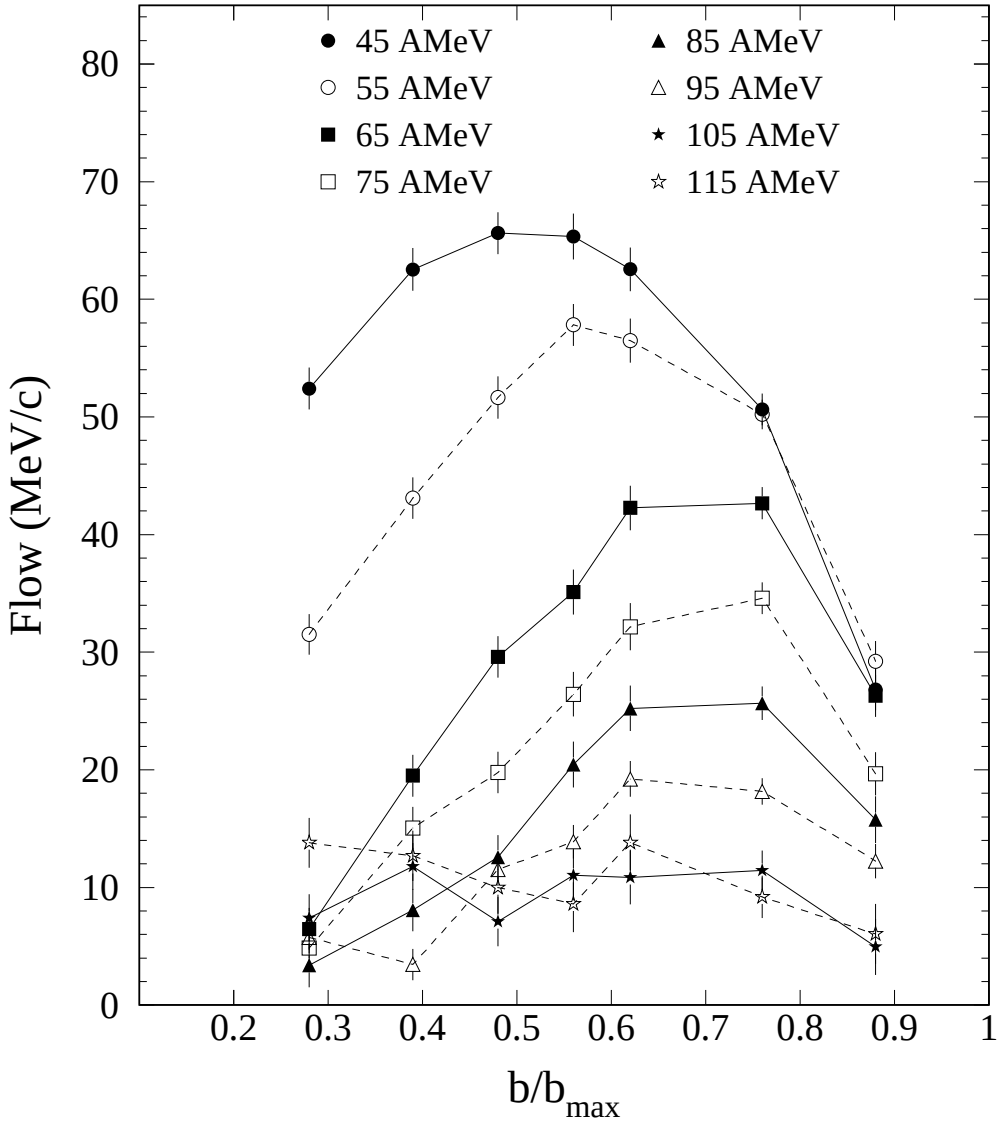

Figure 5.8: Directed transverse flow as a function of reduced impact parameter for He fragments from ^{40}Ar+^{45}Sc collisions at eight beam energies. The lines are included only to guide the eye.

the lever arms created by those points. The resulting impact parameter dependence shown in Figure 5.8 is in qualitative agreement with previous results that range in beam energy from 55 MeV/nucleon [Sull90, Pete92] to 400 MeV/nucleon [Gutb89]. That collective transverse flow is maximal at some intermediate impact parameter is reasonable because it must vanish at the extrema, *i.e.,* for grazing and perfectly central collisions.

Having demonstrated that there is an impact parameter dependence for transverse flow in reaction plane, we next examine the beam energy dependence at a specified impact parameter. The dependence of directed transverse flow on the projectile energy is well established [Krof89, Ogil89b, Sull90, Zhan90, Krof91, Krof92, Shen93, Laur94, Buta95]; our purpose here being to show our data for the ^{40}Ar+^{45}Sc system conform with the standard result. The following pages are the results of the transverse momentum analysis for the four most central reduced impact parameter bins. In Figure 5.9 to Figure 5.12 we show the mean transverse momentum in the reaction plane $\langle p_x \rangle$ plotted versus the reduced c.m. rapidity $(y/y_{proj})_{c.m.}$. The data are for fragments with $Z = 2$ from ^{40}Ar+^{45}Sc reactions at eight incident beam energies, where the given reduced impact parameter bins are listed in Table 3.1. The errors shown in each panel are statistical; the error on the mean is given for each rapidity bin. The data are fit with a straight line in the midrapidity region -0.5 $\leq (y/y_{proj})_{c.m.} \leq$ 0.5 for the purpose of extracting the directed transverse flow. Normalization of the c.m. rapidity facilitates this fitting procedure over the entire range of beam energies studied. The balance energy will be extracted in Section 5.4 as a function of impact parameter from the linear fits in Figure 5.9 to Figure 5.12, and therefore these figures are included for sake of completeness.

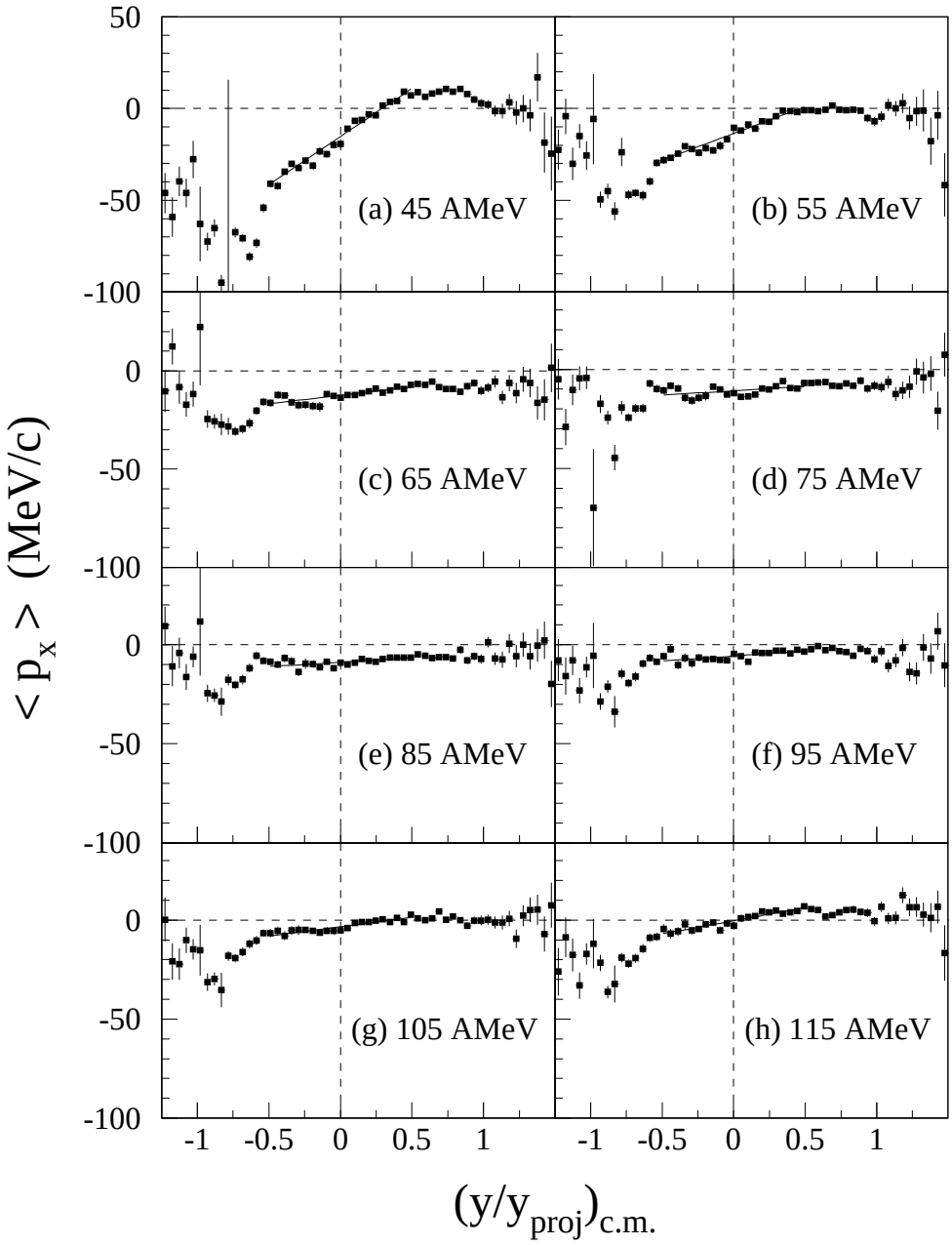

Figure 5.9: Mean transverse momentum in the reaction plane versus the reduced c.m. rapidity for $Z = 2$ fragments from ^{40}Ar+^{45}Sc reactions in $\hat{b}$ bin BIN1. The straight lines are fit in the region -0.5 $\leq (y/y_{proj})_{c.m.} \leq$ 0.5.

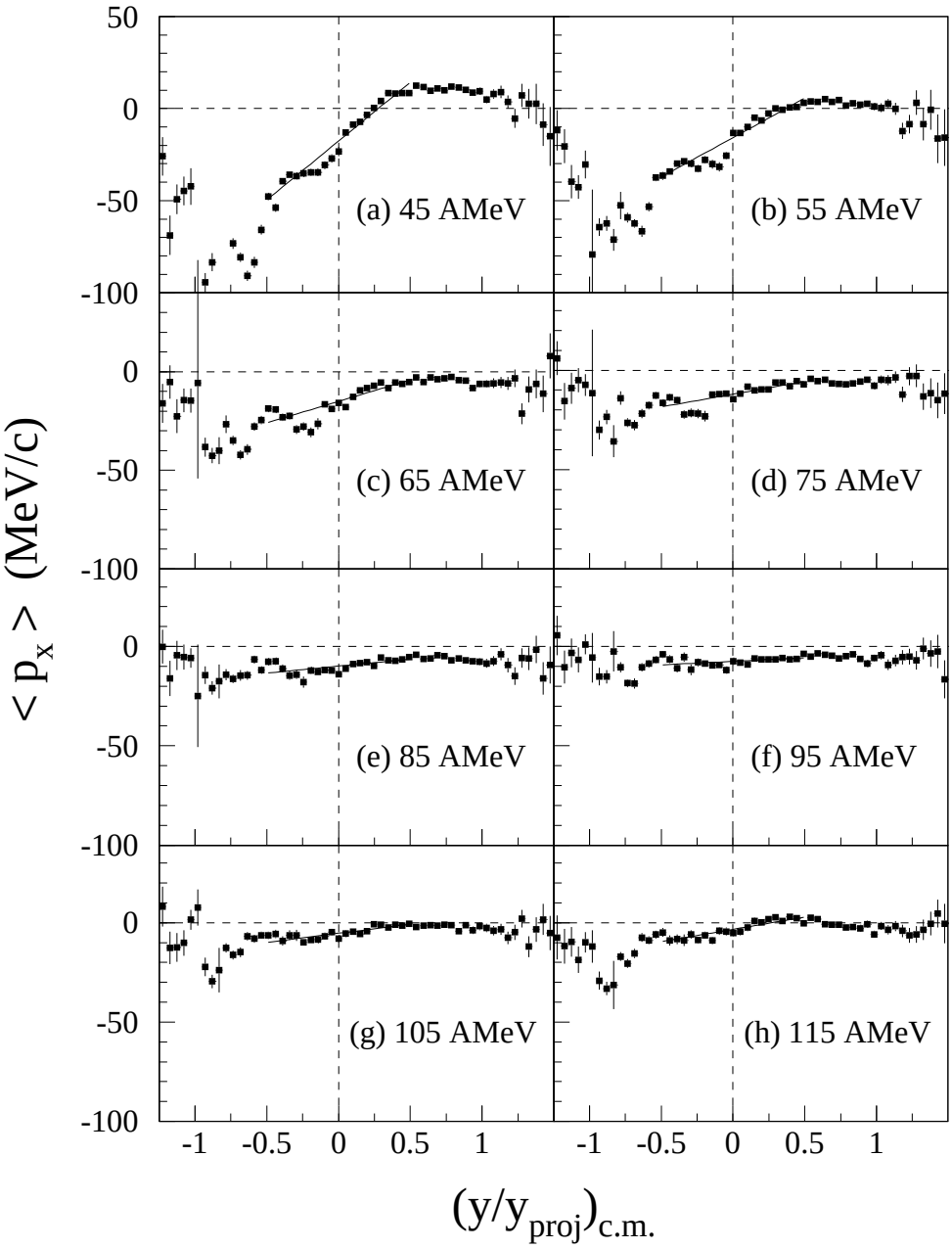

Figure 5.10: Same as Figure 5.9 only for $\hat{b}$ bin BIN2.

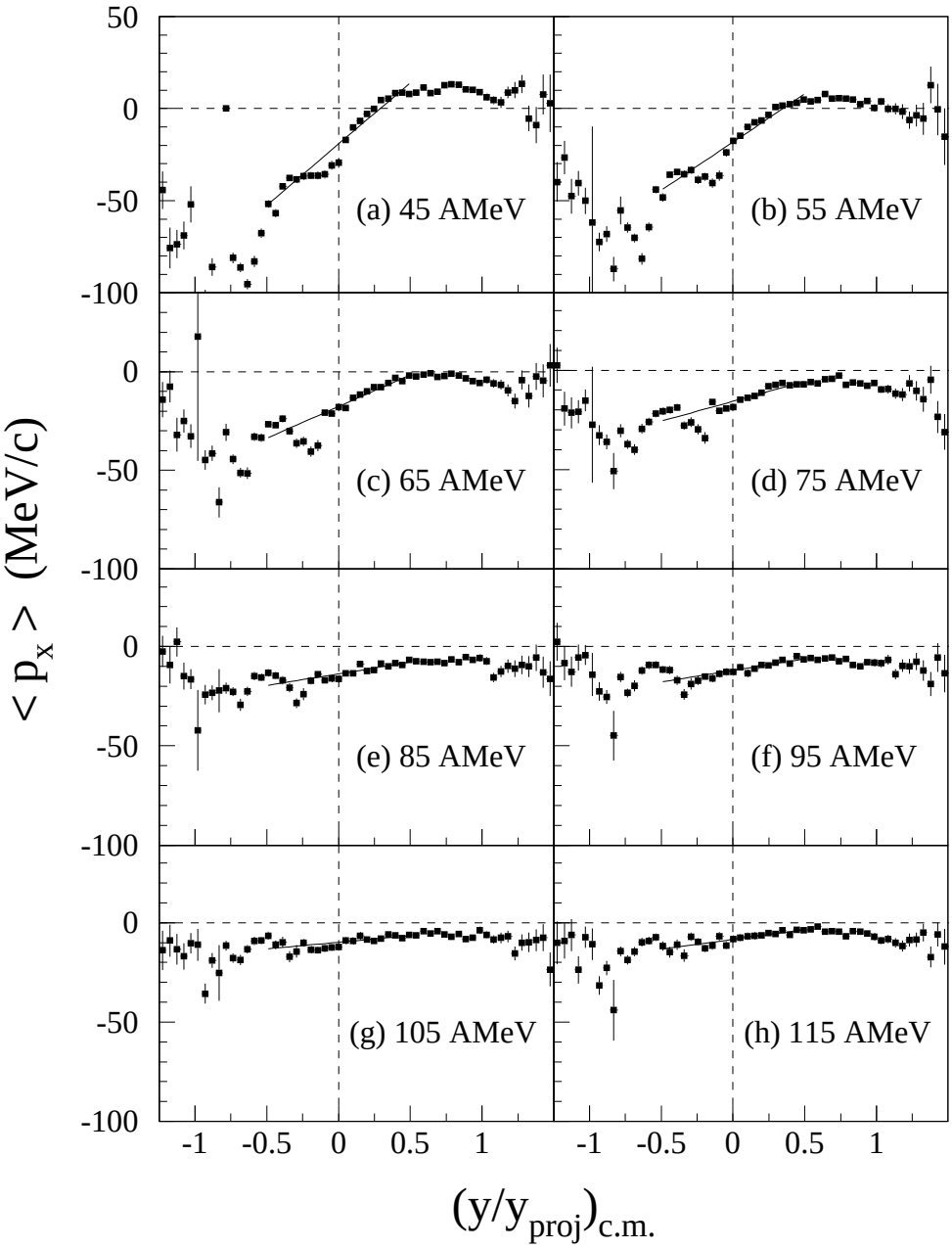

Figure 5.11: Same as Figure 5.9 only for $\hat{b}$ bin BIN3.

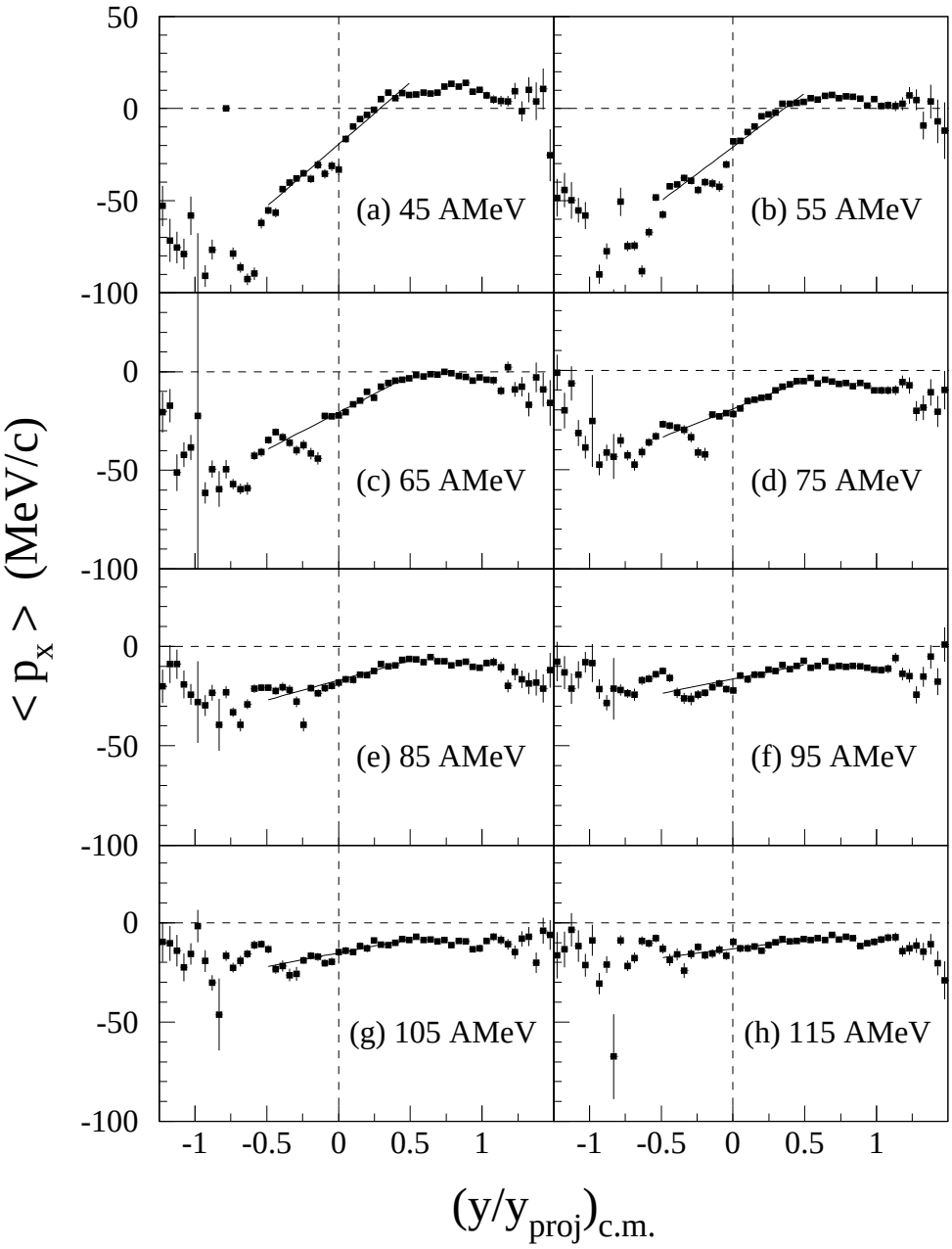

Figure 5.12: Same as Figure 5.9 only for $\hat{b}$ bin BIN4.

5.4 Balance Energy

The extracted values of the directed transverse flow plotted versus the beam energy are shown in Figure 5.13 for the four most central reduced impact parameter bins (as listed in Table 3.1). These values are the slopes of the linear fits shown in Figure 5.9 to Figure 5.12 for $Z = 2$ fragments from ^{40}Ar+^{45}Sc collisions taken with a Ball-2 hardware trigger. The errors shown are the statistical errors on the slopes of the linear fits. As stated for Figure 5.8, the systematic error associated with the range of the fitting region is +3 MeV/c and -1 MeV/c. The data points for each $\hat{b}$ bin are fit with a second-order polynomial for the purpose of finding the balance energy E_{bal}. We found that the analytic form of the fitting function does not significantly affect the value of the extracted balance energy [Ogil90]. We assume collective transverse flow to be symmetric in the vicinity of the balance energy, and our measurements are unable to distinguish the sign (+ or -) of the flow, so that a parabolic function is the lowest order symmetric fit we can use without *a priori* knowledge of E_{bal}. In addition this local parabolic fit, which also has been previously investigated [Ogil90], facilitates extraction of the balance energy for the larger impact parameters where the flow does not strongly reappear.

The curves shown in Figure 5.13 pass through minima for which the value of the abscissa corresponds to the balance energy at each reduced impact parameter $E_{bal}(b)$. For the largest $\hat{b}$ bin displayed in this figure only a lower limit on the value of $E_{bal}(b)$ could be determined from these data, because the higher beam energies necessary to extract $E_{bal}(b)$ for more peripheral collisions were not available from the K1200 cyclotron. The curves do not pass through zero at $E_{bal}(b)$ because no recoil correction was used in the reaction plane determination. Although the extracted values of $E_{bal}(b)$ remain unaffected within error, the recoil correction was found to

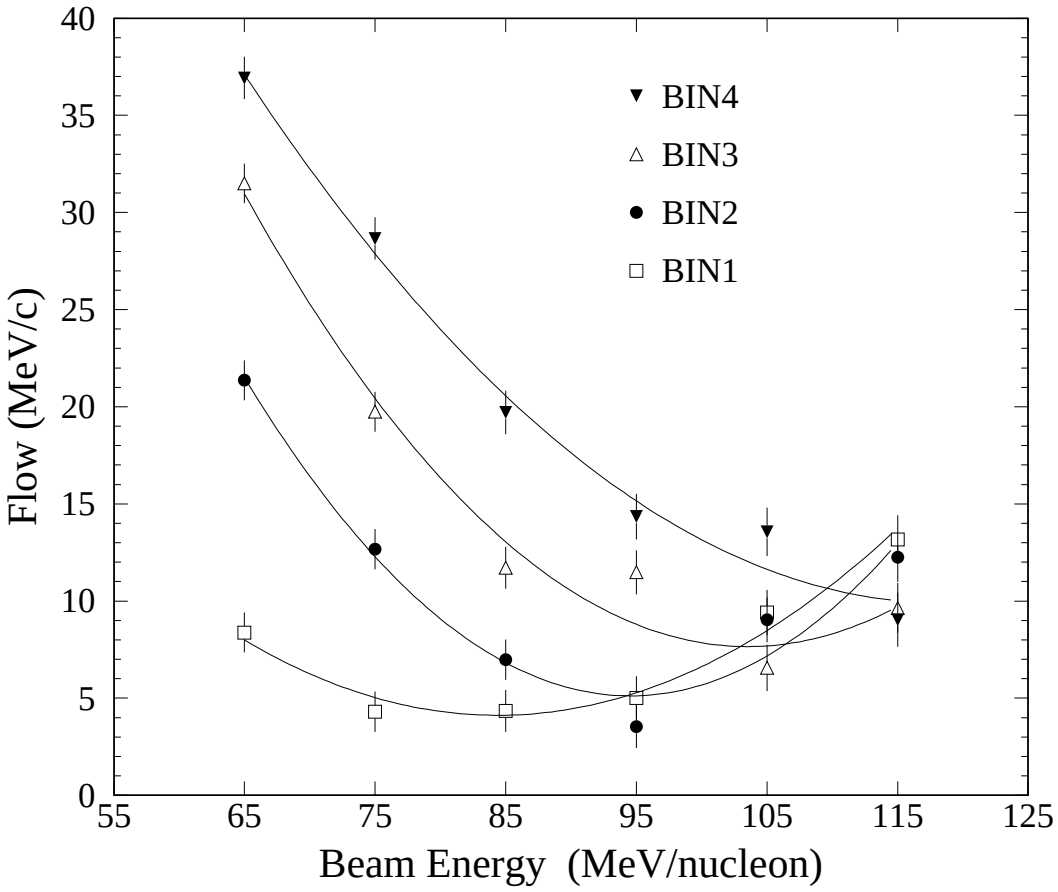

Figure 5.13: Excitation functions of the measured transverse flow in the reaction plane for $Z = 2$ fragments at four reduced impact parameter bins for ^{40}Ar+^{45}Sc reactions. The corresponding values of $\hat{b}$ are given in Table 3.1. The solid curves are parabolic fits as described in the text.

shift the locus of the data for a given $\hat{b}$ bin vertically downward, and even cause negative flow values. Negative flow values are inconsistent with the basic premises of the transverse momentum analysis [Dani85], and therefore the recoil correction was not further applied in the present work.

This is demonstrated in Figure 5.14, which shows the excitation functions of the measured reduced transverse flow in the reaction plane calculated with the recoil correction (given by Equation 3.11) for $Z = 2$ fragments in the four most central $\hat{b}$ bins for ^{40}Ar+^{45}Sc reactions. Reduced flow is calculated using $\langle p_x/p_t \rangle$ (instead of $\langle p_x \rangle$) where the POI's transverse momentum in the reaction plane has been normalized using the magnitude of that fragment's total transverse momentum p_t. The minima of the second-order fits in this figure are clearly the same within error as those in Figure 5.13. Although $E_{bal}(b)$ remains unaffected, some of the values for the reduced flow are negative in Figure 5.14 when the recoil correction was used.

The horizontal shift in the minima of the curves in Figure 5.13 clearly indicates that $E_{bal}(b)$ increases as the impact parameter increases [Pak96a]. This result is in qualitative agreement with previous work [Sull90], but here we are able to more definitively extract $E_{bal}(b)$ for larger impact parameters because our measurements include more data points above the balance energy. This result was also found through an entirely different analysis using correlation functions [Buta95], which does not require reaction plane determination or recoil correction. The measured values of the balance energies for ^{40}Ar+^{45}Sc reactions extracted for the four most central reduced impact parameter bins are listed in the second column of Table 5.1, and the errors given are statistical. The corresponding values of $\hat{b}$ are given in Table 3.1.

As additional verification for the validity of the systematics of our transverse momentum analysis method, we repeated the entire analysis for data taken with a

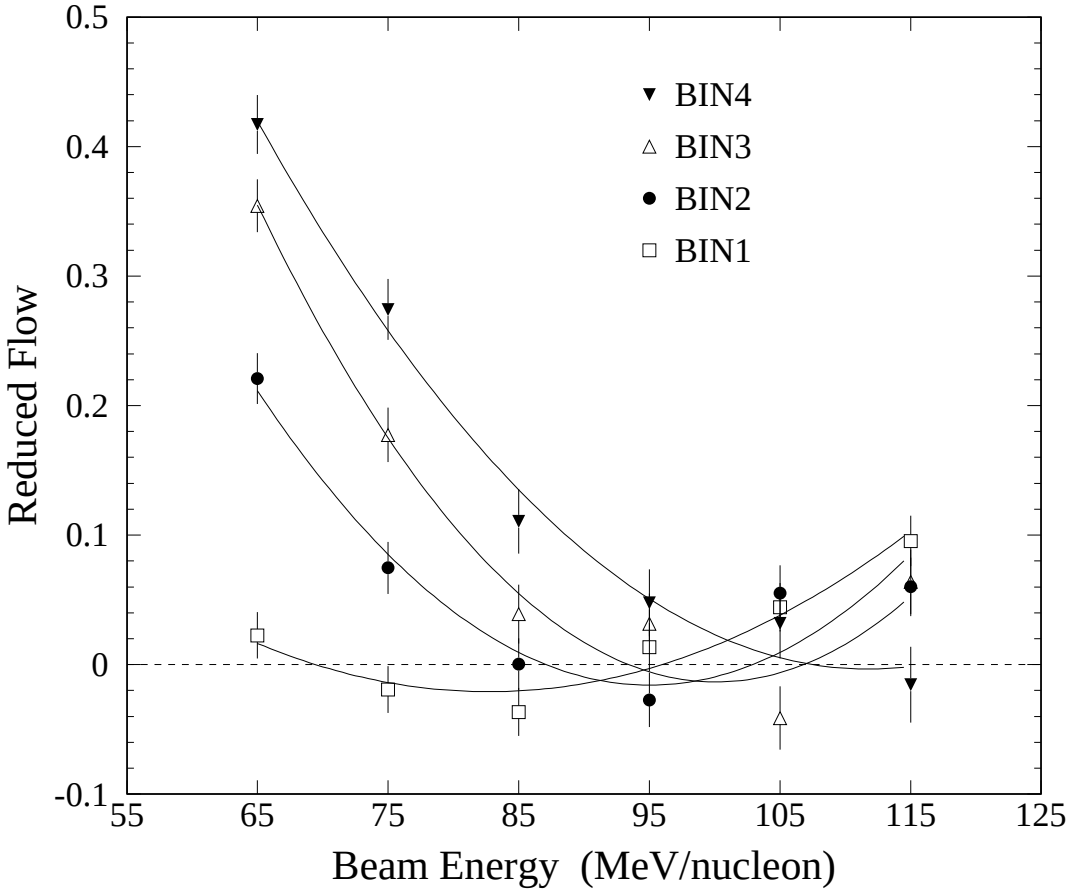

Figure 5.14: Excitation functions of the measured reduced transverse flow in the reaction plane calculated with the recoil correction for $Z = 2$ fragments at four reduced impact parameter bins for ^{40}Ar+^{45}Sc reactions. The corresponding values of $\hat{b}$ are given in Table 3.1. The solid curves are parabolic fits as described in the text.

Table 5.1: Balance energies for four reduced impact parameter bins.

Bin No.	E_{bal} (Ball-2) (MeV/nucleon)	E_{bal} (HRA-1) (MeV/nucleon)
BIN1	84±7	86±8
BIN2	95±4	97±5
BIN3	104±5	114±9
BIN4	119±10	133±13

HRA-1 hardware trigger. These results are displayed in Figure 5.15, which shows the excitation functions of the measured transverse flow in the reaction plane calculated for $Z = 2$ fragments at four reduced impact parameter bins for ^{40}Ar+^{45}Sc reactions. The extracted balance energies for the HRA-1 data listed in the third column of Table 5.1 are (as expected) systematically higher than those for the Ball-2 data in the second column. This is because the event set cut on for impact parameter selection for the HRA-1 data contains more peripheral collisions than the Ball-2 data set, raising the $E_{bal}(b)$ for each $\hat{b}$ bin.

Up to this point in this section, we have only considered balance energies extracted with He fragments as the POI. As noted in Section 5.3, the directed transverse flow increases as the fragment mass increases for a given impact parameter and incident beam energy. However, the balance energy does not depend on the particle type, as shown in Figure 5.16. The open circles in each panel are the directed transverse flow values for $Z = 2$ fragments at each $\hat{b}$ bin previously shown in Figure 5.13. Included now are the directed flow values for fragments with $Z = 1$ (solid squares) and $Z = 3$ (solid triangles), which demonstrate that the $E_{bal}(b)$ is the same for these three particle types and increases as the impact parameter increases. The larger spread in value of $E_{bal}(b)$ for the different POI in panels (c) and (d) can be attributed to the lack of data points to fit above the balance energy.

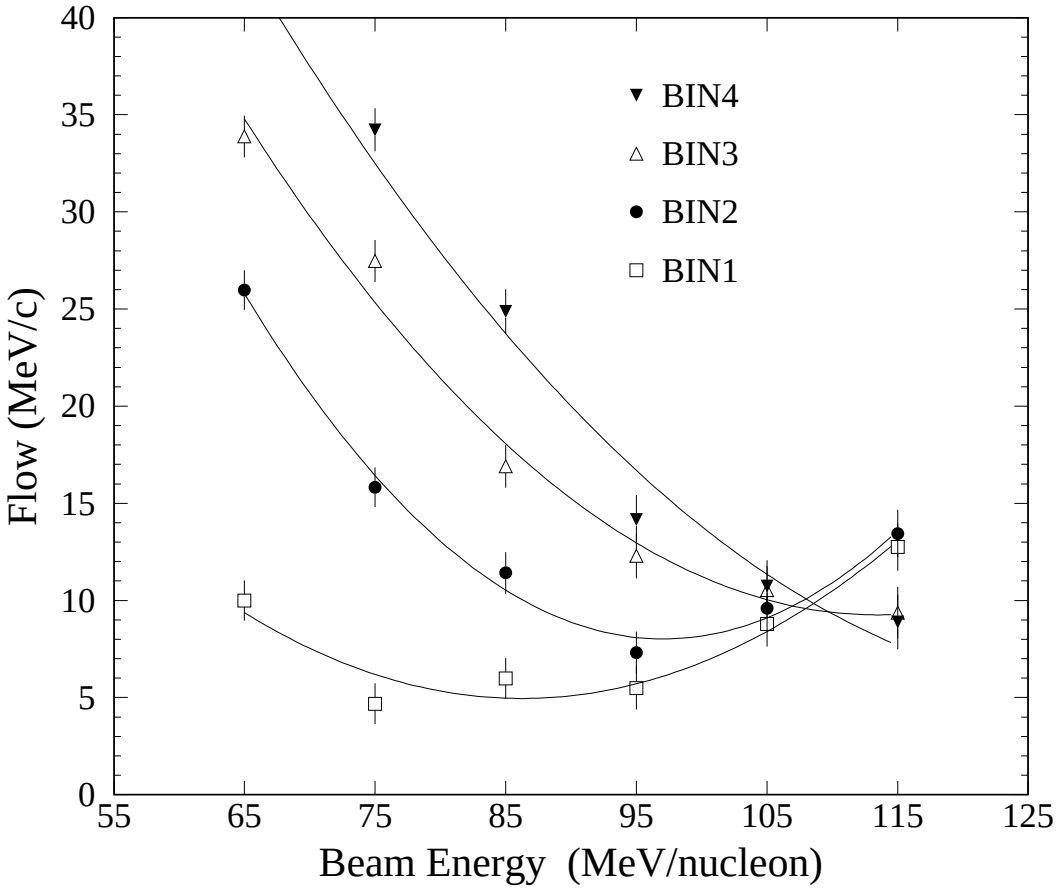

Figure 5.15: Same as Figure 5.13 except for data taken with a HRA-1 trigger.

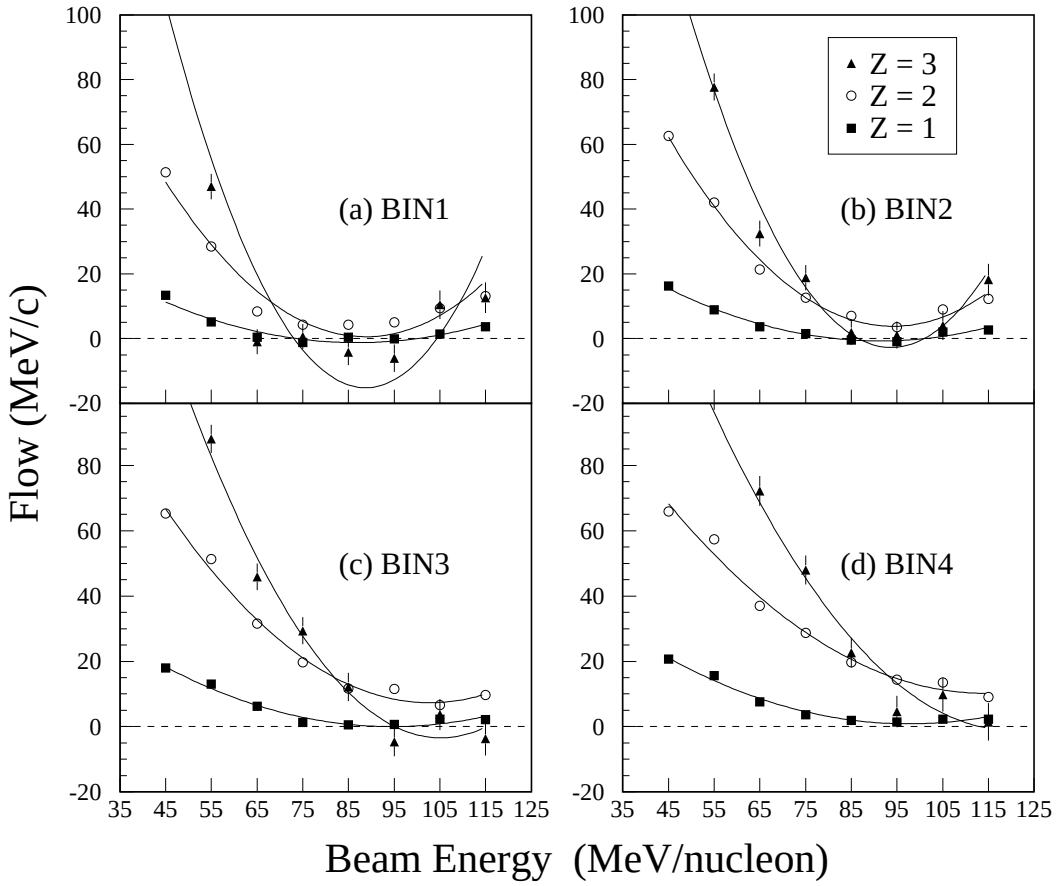

Figure 5.16: Excitation functions of the measured transverse flow in the reaction plane for three particle types at four reduced impact parameter bins for ^{40}Ar+^{45}Sc reactions. Solid squares are for fragments with $Z = 1$; open circles for $Z = 2$; and solid triangles for $Z = 3$. The corresponding values of $\hat{b}$ are given in Table 3.1. The solid curves are parabolic fits as described in the text.

5.5 Comparison to QMD

Transport model calculations can incorporate soft and stiff descriptions of the nuclear EOS as well as momentum dependence in the mean field. The predictions of Quantum Molecular Dynamics (QMD) model [Soff95] calculations are displayed in Figure 5.17 for a stiff equation of state without momentum dependence for ^{40}Ca+^{40}Ca reactions (open circles). These points are calculated for a fixed impact parameter and are not corrected for the acceptance effects of our detector array. Also shown in this figure are the measured values of the balance energies for ^{40}Ar+^{45}Sc reactions extracted for the four most central reduced impact parameter bins (solid triangles). The experimental values of $E_{bal}(b)$ are plotted at the upper limit of each $\hat{b}$ bin represented by the dotted histogram. The errors shown on the measured values of the balance energies are statistical (the systematic error is estimated to be +5% and -0%). We find that $E_{bal}(b)$ increases approximately linearly as a function of the impact parameter [Pak96a] in good agreement with QMD theory [Soff95]. This agreement demonstrates that the impact parameter dependence of the disappearance of transverse flow may potentially provide a powerful probe of the nuclear EOS. The result shown for BIN2 ($\hat{b} = 0.39$) is comparable with our previous measurement of E_{bal} for ^{40}Ar+^{45}Sc of 87±12 MeV/nucleon (solid square) at $\hat{b} = 0.40$ assigned through a cut on the total transverse momentum [West93]. The value of $\hat{b}$ for this point has not been corrected as in the present analysis.

Predictions of QMD model [Soff95] calculations are displayed in Figure 5.18 for a stiff equation of state with momentum dependence (open circles) and without momentum dependence (open squares) for ^{40}Ca+^{40}Ca reactions. Also shown are the measured values of the balance energies for ^{40}Ar+^{45}Sc reactions extracted for the four most central reduced impact parameter bins (solid triangles) as in Figure 5.17.

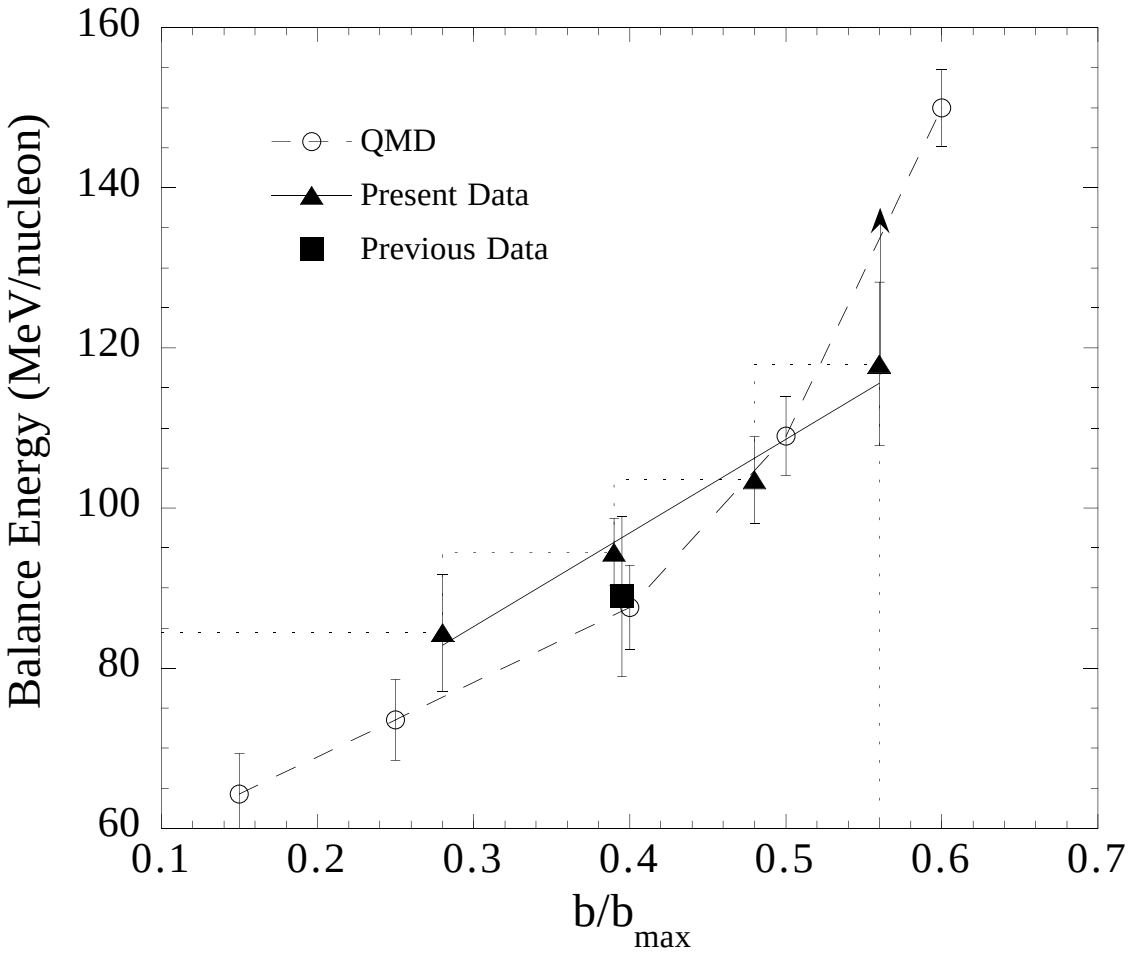

Figure 5.17: Measured balance energies for ^{40}Ar+^{45}Sc reactions at the four most central reduced impact parameter bins compared with the predictions of the QMD model for ^{40}Ca+^{40}Ca reactions [Soff95]. The experimental values of $E_{bal}(b)$ are plotted at the upper limit of each $\hat{b}$ bin represented by the dotted histogram. The curves are included only to guide the eye. The value of previous data is from Reference [West93].

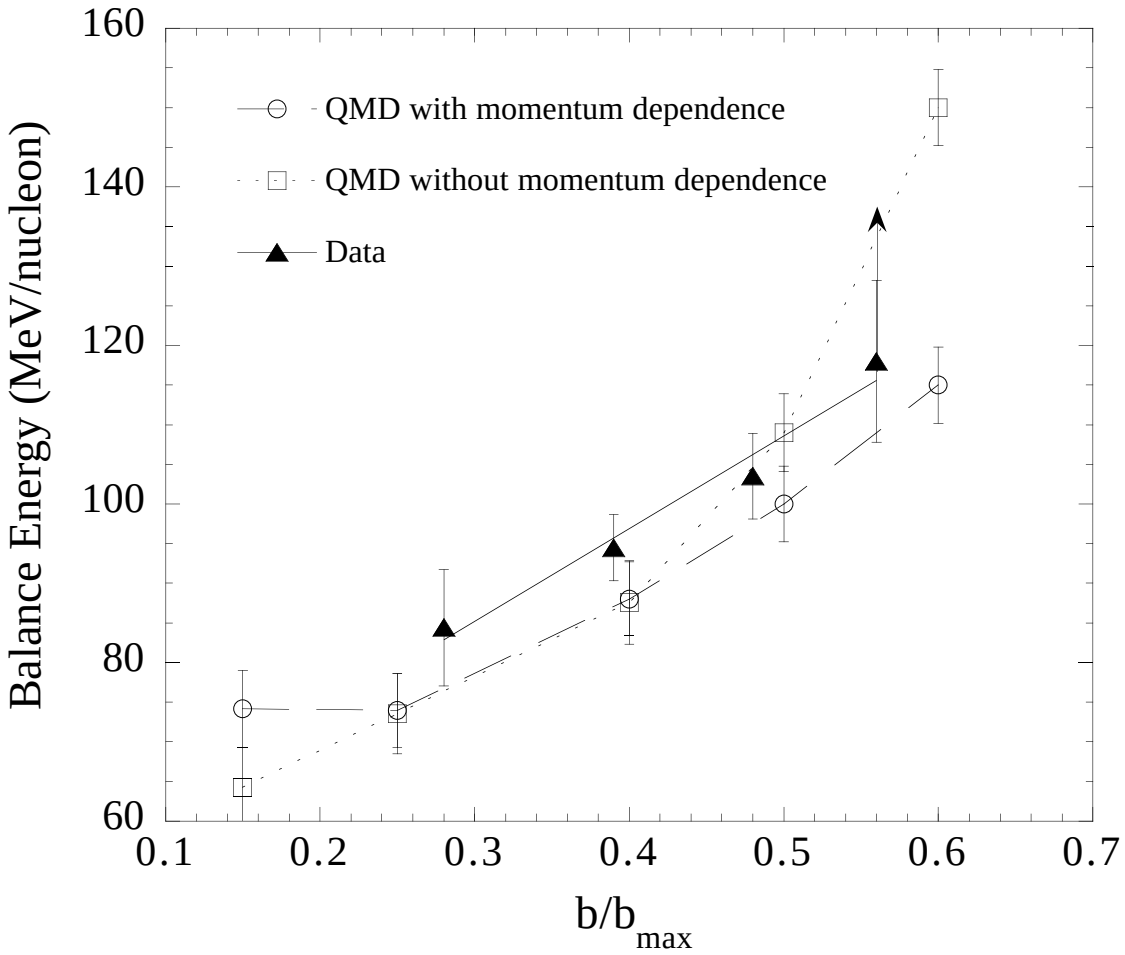

Figure 5.18: Measured balance energies for ^{40}Ar+^{45}Sc reactions at the four most central reduced impact parameter bins compared with the predictions of the QMD model [Soff95] with and without momentum dependence in the mean field for ^{40}Ca+^{40}Ca reactions. The curves are included only to guide the eye.

From Figure 5.18 it is apparent that additional experiments at higher beam energies are necessary to measure $E_{bal}(b)$ at larger impact parameters where sensitivity to the momentum dependence in the nuclear mean field is indicated by the QMD model. In addition transport model calculations which account for the impact parameter distribution sampled by the data [Hand94], and run through our detector filter would allow a more definitive comparison between experiment and theory. Indeed, we concur with statement that a precise knowledge of the impact parameter is of utmost importance before conclusions about the nuclear EOS can be drawn from the balance energy [Soff95].

5.6 Conclusions

In summary, we have investigated the impact parameter dependence of the disappearance of directed transverse flow for ^{40}Ar+^{45}Sc reactions using the MSU 4π Array upgraded with the HRA. Our results indicate that the balance energy increases approximately linearly as a function of impact parameter. Physically this dependence results from a smaller participant zone in more peripheral collisions, so that a larger incident energy is required to overcome effects of the mean field. Comparison of the trends in our measured values of $E_{bal}(b)$ is consistent with the predictions of QMD model calculations. We agree with the point of view expressed in previous theoretical work [Klak93, Soff95] that the balance energy is indeed dependent upon impact parameter.

Chapter 6

Conclusion

We have investigated collective flow of light fragments for the system ^{40}Ar+^{45}Sc at beam energies in the range E = (35 - 115) MeV/nucleon, because the study of collective flow in these heavy-ion collisions can provide information about the EOS of nuclear matter. Event characterization was achieved through high-statistics exclusive measurements using the MSU 4π Array upgraded with the High Rate Array (HRA). The major motivation behind this study has been to extract information which would further constrain the parameters in the nuclear EOS through comparison of our experimental data to the predictions of theoretical model calculations. In the following paragraphs we briefly reiterate the main conclusions drawn from the analyses in the previous chapters of this thesis.

Collective radial flow of light fragments in the nuclear disassembly process was demonstrated through transverse energy production. The mean transverse kinetic energy of the different fragment types increases with event centrality, and increases as a function of the incident beam energy. At the higher beam energies, the dramatic increase in the values of $\langle E_t \rangle$ for the heavier fragments produced in central collisions is linked to larger values of the radial flow energy. This is in contrast to expectations of a purely thermal source for which the different particle types are emitted with the same

mean kinetic energy. Comparison of our measured values of $\langle E_t \rangle$ shows agreement with predictions of BUU model and WIX multifragmentation model calculations. The radial flow extracted from $\langle E_t \rangle$ accounts for approximately half of the emitted particle's energy for the heavier fragments ($Z \geq 4$) at the highest beam energy studied.

Collective directed transverse flow was measured with a transverse momentum analysis method in which the reaction plane was determined using the azimuthal correlation technique. The energy at which collective transverse flow in the reaction plane disappears, termed the balance energy E_{bal}, is found to increase approximately linearly as a function of impact parameter b. Physically this dependence results from a smaller participant zone in more peripheral collisions, so that a larger incident energy is required to compensate for the effects of the mean field. Comparison of the trends in our measured values of $E_{bal}(b)$ is consistent with the predictions of QMD model calculations. This agreement demonstrates that the impact parameter dependence of the disappearance of transverse flow may potentially provide a powerful probe of the nuclear EOS.

Appendix A

Mean Angles for the Phoswiches

On the following pages of this appendix are tables listing the angular positions for each of the phoswiches in the MSU 4π Array. Table A.1 lists the mean angles (θ, ϕ) for the main ball phoswiches in degrees. The mean angles for the High Rate Array phoswiches (in degrees) are given in the Table A.2. Here θ is the laboratory polar angle, defined as the angle between the beam axis and a line from the target to the center of the detector. The azimuthal angle ϕ is the angle between an arbitrary, fixed reference plane that includes the beam axis and the plane that passes through the beam axis and the center of the detector.

Table A.1: Mean angles for the ball phoswiches.

Module	A		B		C		D		E		F	
	θ	ϕ	θ	ϕ	θ	ϕ	θ	ϕ	θ	ϕ	θ	ϕ
1	23.1	342.0	32.3	5.6	46.0	356.3	51.7	342.0	46.0	324.7	32.3	318.4
2	23.1	270.0	32.3	293.6	46.0	287.3	51.7	270.0	46.0	252.7	32.3	246.4
3	23.1	198.0	32.3	221.6	46.0	215.3	51.7	198.0	46.0	180.7	32.3	174.4
4	23.1	126.0	32.3	149.6	46.0	143.3	51.7	126.0	46.0	108.7	32.3	102.4
5	23.1	54.0	32.3	77.6	46.0	71.3	51.7	54.0	46.0	36.7	32.3	30.4
6	54.7	298.0	54.7	314.0	67.3	317.5	74.6	306.0	67.3	294.5		
7	54.7	226.0	54.7	242.0	67.3	245.5	74.6	234.0	67.3	222.5		
8	54.7	154.0	54.7	170.0	67.3	173.5	74.6	162.0	67.3	150.5		
9	54.7	82.0	54.7	98.0	67.3	101.5	74.6	90.0	67.3	78.5		
10	54.7	10.0	54.7	26.0	67.3	29.5	74.6	18.0	67.3	6.5		
11	64.9	342.0	72.4	355.0	86.5	354.4	93.5	342.0	86.5	329.6	72.4	329.0
12	64.9	270.0	72.4	283.0	86.5	282.4	93.5	270.0	86.5	257.6	72.4	257.0
13	64.9	198.0	72.4	211.0	86.5	210.4	93.5	198.0	86.5	185.6	72.4	185.0
14	64.9	126.0	72.4	139.0	86.5	138.4	93.5	126.0	86.5	113.6	72.4	113.0
15	64.9	54.0	72.4	67.0	86.5	66.4	93.5	54.0	86.5	41.6	72.4	41.0
16	86.5	306.0	93.5	318.4	107.6	319.0	115.1	306.0	107.6	293.0	93.5	293.6
17	86.5	234.0	93.5	246.4	107.6	247.0	115.1	234.0	107.6	221.0	93.5	221.6
18	86.5	162.0	93.5	174.4	107.6	175.0	115.1	162.0	107.6	149.0	93.5	149.6
19	86.5	90.0	93.5	102.4	107.6	103.0	115.1	90.0	107.6	77.0	93.5	77.6
20	86.5	18.0	93.5	30.4	107.6	31.0	115.1	18.0	107.6	5.0	93.5	5.6
21	105.4	342.0	112.7	353.5	125.3	350.0	125.3	334.0	112.7	330.5		
22	105.4	270.0	112.7	281.5	125.3	278.0	125.3	262.0	112.7	258.5		
23	105.4	198.0	112.7	209.5	125.3	206.0	125.3	190.0	112.7	186.5		
24	105.4	126.0	112.7	137.5	125.3	134.0	125.3	118.0	112.7	114.5		
25	105.4	54.0	112.7	65.5	125.3	62.0	125.3	46.0	112.7	42.5		
26	128.3	306.0	134.0	323.3	147.7	329.6	156.9	306.0	147.7	282.4	134.0	288.7
27	128.3	234.0	134.0	251.3	147.7	257.6	156.9	234.0	147.7	210.4	134.0	216.7
28	128.3	162.0	134.0	179.3	147.7	185.6	156.9	162.0	147.7	138.4	134.0	144.7
29	128.3	90.0	134.0	107.3	147.7	113.6	156.9	90.0	147.7	66.4	134.0	72.7
30	128.3	18.0	134.0	35.3	147.7	41.6	156.9	18.0	147.7	354.4	134.0	0.7

Table A.2: Mean angles for the HRA phoswiches.

Detector	θ	ϕ	Detector	θ	ϕ	Detector	θ	ϕ
1	5.4	0.0	16	10.6	246.0	31	14.3	279.0
2	5.4	324.0	17	10.6	222.0	32	14.3	261.0
3	5.4	288.0	18	9.6	198.0	33	15.9	243.0
4	5.4	252.0	19	10.6	174.0	34	15.9	225.0
5	5.4	216.0	20	10.6	150.0	35	14.3	207.0
6	5.4	180.0	21	9.6	126.0	36	14.3	189.0
7	5.4	144.0	22	10.6	102.0	37	15.9	171.0
8	5.4	108.0	23	10.6	78.0	38	15.9	153.0
9	5.4	72.0	24	9.6	54.0	39	14.3	135.0
10	5.4	36.0	25	10.6	30.0	40	14.3	117.0
11	10.6	6.0	26	15.9	9.0	41	15.9	99.0
12	9.6	342.0	27	14.3	351.0	42	15.9	81.0
13	10.6	318.0	28	14.3	333.0	43	14.3	63.0
14	10.6	294.0	29	15.9	315.0	44	14.3	45.0
15	9.6	270.0	30	15.9	297.0	45	15.9	27.0

Bibliography

[Barz91] H.W. Barz, J.P. Bondorf, R. Donangelo, R. Elmér, F.S. Hansen, B. Jakobsson, L. Karlsson, H. Nifenecker, H. Schulz, F. Schussler, K. Sneppen, and K. Söderström, Nucl. Phys. **A531**, 453 (1991).

[Baue86] W. Bauer, G.F. Bertsch, W. Cassing, and U. Mosel, Phys. Rev. C **34**, 2127 (1986).

[Baue88] W. Bauer, Phys. Rev. Lett. **61**, 2534 (1988).

[Baue92] W. Bauer, G.F. Bertsch, and H. Schulz, Phys. Rev. Lett. **69**, 1888 (1992).

[Baue93] W. Bauer, J.P. Bondorf, R. Donangelo, R. Elmér, B. Jakobsson, H. Schulz, F. Schussler, and K. Sneppen, Phys. Rev. C **47**, R1838 (1993).

[Bert87] G.F. Bertsch, W.G. Lynch, and M.B. Tsang, Phys. Lett. B **189**, 384 (1987).

[Bicr85] Bicron Inc. Newbury, OH 44065 USA and NE Technology Inc. Monmouth Junction, NJ 08852 USA.

[Bond78] J.P. Bondorf, S.I.A. Garpman, and J. Zimànyí, Nucl. Phys. **A296**, 320 (1978).

[Bres82] A. Breskin, Nucl. Instr. and Methods **196**, 11 (1982).

[Buta95] A. Buta, J.C. Angélique, G. Auger, G. Bizard, R. Brou, C. Cabot, Y. Cassagnou, E. Crema, D. Cussol, Y. El Masri, Ph. Eudes, M. Gonin, K. Hagel, Z.Y. He, A. Kerambrun, C. Lebrun, R. Legrain, J.P. Patry, A. Péghaire, J. Péter, R. Popescu, R. Régimbart, E. Rosato, F. Saint-Laurent, J.C. Steckmeyer, B. Tamain, E. Vient, and R. Wada, Nucl. Phys. **A584**, 397 (1995).

[Cava90] C. Cavata, M. Demoulins, J. Gosset, M.-C. Lemaire, D. L'Hôte, J. Poitou, and O. Valette, Phys. Rev. C **42**, 1760 (1990).

[Cebr91] D.A. Cebra, S. Howden, J. Karn, D. Kataria, M. Maier, A. Nadasen, C.A. Ogilvie, N. Stone, D. Swan, A. Vander Molen, W.K. Wilson, J. Yurkon, G.D. Westfall, and E. Norbeck, Nucl. Instr. and Methods **A300**, 518 (1991).

[Cebr92] D.A. Cebra, W.K. Wilson, A. Vander Molen, and G.D. Westfall, Nucl. Instr. and Methods **A313**, 367 (1992).

[Cugn82] J. Cugnon, J. Knoll, C. Riedel, and Y. Yariv, Phys. Lett. **109B**, 167 (1982).

[Dani85] P. Danielewicz and G. Odyniec, Phys. Lett. **157B**, 146 (1985).

[Dani88] P. Danielewicz, H. Ströbele, G. Odyniec, D. Bangert, R. Bock, R. Brockmann, J.W. Harris, H.G. Pugh, W. Rauch, R.E. Renfordt, A. Sandoval, D. Schall, L.S. Schroeder, and R. Stock, Phys. Rev. C **38**, 120 (1988).

[Dani92] P. Danielewicz and Q. Pan, Phys. Rev. C **46**, 2002 (1992).

[Dani95] P. Danielewicz, Phys. Rev. C **51**, 716 (1995).

[deSo93] R.T. de Souza, D. Fox, W.A. Friedman, L. Phair, D.R. Bowman, C.K. Gelbke, W.G. Gong, Y.D. Kim, M.A. Lisa, W.G. Lynch, G.F. Peaslee, M.B. Tsang, and F. Zhu, Phys. Lett. B **300**, 29 (1993).

[DGup93] S. Das Gupta and G.D. Westfall, Physics Today **46**(5), 34 (1993).

[dlMo92] V. de la Mota, F. Sebille, M. Farine, B. Remaud, and P. Schuck, Phys. Rev. C **46**, 677 (1992).

[Doss86] K.G.R. Doss, H.Å. Gustafsson, H.H. Gutbrod, K.H. Kampert, B.W. Kolb, H. Löhner, B. Ludewigt, A.M. Poskanzer, H.G. Ritter, H.R. Schmidt, and H. Weiman, Phys. Rev. Lett. **57**, 302 (1986).

[Doss87] K.G.R. Doss, H.Å. Gustafsson, H. Gutbrod, J.W. Harris, B.V. Jacak, K.H. Kampert, B. Kolb, A.M. Poskanzer, H.G. Ritter, H.R. Schmidt, L. Teitelbaum, M. Tincknell, S. Weiss, and H. Weiman, Phys. Rev. Lett. **59**, 2720 (1987).

[Doss88] K.G.R. Doss, H.Å. Gustafsson, H.H. Gutbrod, K.H. Kampert, B.W. Kolb, H. Löhner, B. Ludewigt, A.M. Poskanzer, H.G. Ritter, and H.R. Schmidt, Mod. Phys. Lett. A **3**, 849 (1988).

[Fai83] G. Fái and J. Randrup, Nucl. Phys. **A404**, 551 (1983).

[Frie90] W.A. Friedman, Phys. Rev. C **42**, 667 (1990).

[Gaff95] S.J. Gaff, C.K. Gelbke, W. Bauer, F.C. Daffin, T. Glasmacher, E. Gualtieri, K. Haglin, D.O. Handzy, S. Hannuschke, M.J. Huang, G.J. Kunde, R. Lacey, W.G. Lynch, L. Martin, C.P. Montoya, R. Pak, S. Pratt, N. Stone, M.B. Tsang, A.M. Vander Molen, G.D. Westfall, and J. Yee, Phys. Rev. C **52**, 2782 (1995).

[Goss89] J. Gosset, O. Valette, J.P. Alard, J. Augerat, R. Babinet, N. Bastid, F. Brochard, N. De Marco, P. Dupieux, Z. Fodor, L. Fraysse, P. Gorodetzky, M.C. Lemaire, D. L'Hôte, B. Lucas, J. Marroncle, G. Montarou, M.J. Parizet, J. Poitou, C. Racca, A. Rahmani, W. Schimmerling, and Y. Terrien, Phys. Rev. Lett. **62**, 1251 (1989).

[Gruh82] C.R. Gruhn, M. Binimi, R. Legrain, R. Loveman, W. Pang, M. Roach, D.K. Scott, A. Shotter, T.J. Symons, J. Wouters, M. Zisman, R. de Vries, Y.C. Peng, and W. Sondheim, Nucl. Instr. and Methods **196**, 33 (1982).

[Gual95] E.E. Gualtieri, J. Yee, D. Craig, S. Hannuschke, Roy A. Lacey, T. Li, W.J. Llope, A. Nadasen, E. Norbeck, R. Pak, N.T.B. Stone, A.M. Vander Molen, J.S. Winfield, G.D. Westfall, and S.J. Yennello, Phys. Lett. B **357**, 7 (1995).

[Gust84] H.Å. Gustafsson, H.H. Gutbrod, B. Kolb, H. Löhner, B. Ludewigt, A.M. Poskanzer, T. Renner, H. Riedesel, H.G. Ritter, A. Warwick, F. Weik, and H. Weiman, Phys. Rev. Lett. **52**, 1590 (1984).

[Gutb89] H.H. Gutbrod, A.M. Poskanzer, and H.G. Ritter, Rep. Prog. Phys. **52**, 1267 (1989).

[Gutb91] H. Gutbrod and H. Stöcker, Scientific American **265**(5), 58 (1991).

[Gyul82] M. Gyulassy, K.A. Frankel, and H. Stöcker, Phys. Lett. **110B**, 185 (1982).

[Hage92] K. Hagel, M. Gonin, R. Wada, J.B. Natowitz, B.H. Sa, Y. Lou, M. Gui, D. Utley, G. Nebbia, D. Fabris, G. Prete, J. Ruiz, D. Drain, B. Chambon, B. Cheynis, D. Guinet, X.C. Hu, A. Demeyer, C. Pastor, A. Giorni, A. Lleres, P. Stassi, J.B. Viano, and P. Gonthier, Phys. Rev. Lett. **68**, 2141 (1992).

[Hand94] D.O. Handzy, M.A. Lisa, C.K. Gelbke, W. Bauer, F.C. Daffin, P. Decowski, W.G. Gong, E. Gualtieri, S. Hannuschke, R. Lacey, T. Li, W.G. Lynch, C.M. Mader, G.F. Peaslee, T. Reposeur, S. Pratt, A.M. Vander Molen, G.D. Westfall, J. Yee, and S.J. Yennello, Phys. Rev. C **50**, 858 (1994).

[Hand95] D.O. Handzy, W. Bauer, F.C. Daffin, S.J. Gaff, C.K. Gelbke, T. Glasmacher, E. Gualtieri, S. Hannuschke, M.J. Huang, G.J. Kunde, R. Lacey, T. Li, M.A. Lisa, W.J. Llope, W.G. Lynch, L. Martin, C.P. Montoya, R. Pak, G.F. Peaslee, S. Pratt, C. Schwarz, N. Stone, M.B. Tsang, A.M. Vander Molen, G.D. Westfall, J. Yee, and S.J. Yennello, Phys. Rev. Lett. **75**, 2916 (1995).

[Hann95] S.A. Hannuschke, A.M. Vander Molen, D. Craig, E. Gualtieri, W.J. Llope, R. Pak, N. Stone, G.D. Westfall, J. Yee, R.A. Lacey, A. Nadasen, and E. Norbeck, "Advances in Nuclear Dynamics, Proc. of the 11^{th} Winter Workshop on Nuclear Dynamics", eds. W. Bauer, Key West, Florida (1995).

[Harr87] J.W. Harris, B.V. Jacak, K.H. Kampert, G. Claesson, K.G.R. Doss, R. Ferguson, A.I. Gavron, H.A. Gustafsson, H. Gutbrod, B. Kolb, F. Lefebvres, A.M. Poskanzer, H.G. Ritter, H.R. Schmidt, L. Teitelbaum, M. Tincknell, S. Weiss, H. Weiman, and J. Wilhelmy, Nucl. Phys. **A471**, 241c (1987).

[Heue94] D. Heuer, A. Chabane, M.E. Brandan, M. Charvet, A.J. Cole, P. Désesquelles, A. Giorni, A. Lleres, A. Menchaca-Rocha, J.B. Viano, D. Benchekroun, B. Cheynis, A. Demeyer, E. Gerlic, D. Guinet, M.Stern, and L. Vagneron, Phys. Rev. C **50**, 1943 (1994).

[Hsi94] W.C. Hsi, G.J. Kunde, J. Pochodzalla, W.G. Lynch, M.B. Tsang, M.L. Begemann-Blaich, D.R. Bowman, R.J. Charity, F. Cosmo, A. Ferrero, C.K. Gelbke, T. Glasmacher, T. Hofmann, G. Imme, I. Iori, J. Hubele, J. Kempter, P. Kreutz, W.D. Kunze, V. Lindenstruth, M.A. Lisa, U. Lynen, M. Mang, A. Moroni, W.F.J. Müller, M. Neumann, B. Ocker, C.A. Ogilvie, G.F. Peaslee, G. Raciti, F. Rosenberger, H. Sann, R. Scardaoni, A. Schüttauf, C. Schwarz, W. Seidel, V. Serfling, L.G. Sobotka, L. Stuttge, S. Tomasevic, W. Trautmann, A. Tucholski, C. Williams, A. Wörner, and B Zwieglinski, Phys. Rev. Lett. **73**, 3367 (1994).

[Jeon94] S.C. Jeong, N. Herrmann, Z.G. Fan, R. Freifelder, A. Gobbi, K.D. Hildenbrand, M. Krämer, J. Randrup, W. Reisdorf, D. Schüll, U. Sodan, K. Teh, J.P. Wessels, D. Pelte, M. Trzaska, T. Wienold, J.P. Alard, V. Amouroux, Z. Basrak, N. Bastid, I.M. Belayev, L. Berger, M. Bini, Th. Blaich, S. Boussange, A. Buta, R. Čaplar, C. Cerruti, N. Cindro, J.P. Coffin, R. Dona, P. Dupieux, J. Erö, P. Fintz, Z. Fodor, L. Fraysse, S. Frolov, Y. Grigorian, G. Guillaume, S. Hölbling, A. Houari, F. Jundt, J. Kecskemeti, P. Koncz, Y. Korchagin, R. Kotte, C. Kuhn, M. Ibnouzahir, I. Legrand, A. Lebedev, C. Maguire, V. Manko, P. Mauerenzig, G. Mgebrishvili, J. Mösner, D. Moisa, G. Montarou, I. Montbel, P. Morel, W. Neubert, A. Olmi, G. Pasquali, M. Petrovici, G. Poggi, F. Rami, V. Ramillien, A. Sadchikov, Z. Seres, B. Sikora, V. Simion, S. Smolyankin, R. Tezkratt, M.A. Vasiliev, P. Wagner, Z. Wilhelmi, D. Wohlfarth, and A.V. Zhilin, Phys. Rev. Lett. **72**, 3468 (1994).

[Jeon95] S.C. Jeong, D. Cussol, D. Durand, R. Laforest, J. Péter, J.C. Angélique, G. Auger, G. Bizard, R. Brou, A. Buta, C. Cabot, Y. Cassagnou, E. Crema, Y. El Masri, P. Eudes, Z.Y. He, A. Kerambrun, C. Lebrun, R. Legrain, J.P. Patry, A. Péghaire, R. Régimbart, E. Rosato, F. Saint-Laurent, J.C. Steckmeyer, B. Tamain, and E. Vient, submitted to Phys. Lett. B

[Klak93] D. Klakow, G. Welke, and W. Bauer, Phys. Rev. C **48**, 1982 (1993).

[Krof89] D. Krofcheck, W. Bauer, G.M. Crawley, C. Djalali, S. Howden, C.A. Ogilvie, A. Vander Molen, G.D. Westfall, and W.K. Wilson, Phys. Rev. Lett. **63**, 2028 (1989).

[Krof91] D. Krofcheck, D.A. Cebra, M. Cronqvist, R. Lacey, T. Li, C.A. Ogilvie, A. Vander Molen, K. Tyson, G.D. Westfall, W.K. Wilson, and J.S. Winfield, Phys. Rev. C **43**, 350 (1991).

[Krof92] D. Krofcheck, W. Bauer, G.M. Crawley, S. Howden, C.A. Ogilvie, A. Vander Molen, G.D. Westfall, W.K. Wilson, R.S. Tickle, C. Djalali, and C. Gale, Phys. Rev. C **46**, 1416 (1992).

[Kund95] G.J. Kunde, W.C. Hsi, W.D. Kunze, A. Schüttauf, A. Wörner, M. Begemann-Blaich, Th. Blaich, D.R. Bowman, R.J. Charity, F. Cosmo, A. Ferrero, C.K. Gelbke, J. Hubele, G. Immé, I. Iori, P. Kreutz, V. Lindenstruth, M.A. Lisa, W.G. Lynch, U. Lynen, M. Mang, T. Möhlenkamp, A. Moroni, W.F.J. Müller, M. Neumann, B. Ocker, C.A. Ogilvie, G.F. Peaslee, J. Pochodzalla, G. Raciti, T. Rubehn, H. Sann, W. Seidel, V. Serfling, L.G. Sobotka, J. Stroth, L. Stuttge, S. Tomasevic, W. Trautmann, M.B. Tsang, A. Tucholski, G. Verde, C.W. Williams, E. Zude, and B Zwieglinski, Phys. Rev. Lett. **74**, 38 (1995).

[Lace93] R.A. Lacey, A. Elmaani, J. Lauret, T. Li, W. Bauer, D. Craig, M. Cronqvist, E. Gualtieri, S. Hannuschke, T. Reposeur, A. Vander Molen, G.D. Westfall, W.K. Wilson, J.S. Winfield, J. Yee, S.J. Yennello, A. Nadasen, R.S. Tickle, and E. Norbeck, Phys. Rev. Lett. **70**, 1224 (1993).

[Laur93] J. Lauret, private communication.

[Laur94] J. Lauret, R.A. Lacey, A. Elmaani, A. Tsepetis, A. Moores, G.D. Westfall, D. Craig, E. Gualtieri, S. Hannuschke, T. Li, W.J. Llope, R. Pak, N. Stone, A. Vander Molen, J. Yee, A. Nadasen, R.S. Tickle, and E. Norbeck, Phys. Lett. B **339**, 22 (1994).

[Li93] T. Li, W. Bauer, D. Craig, M. Cronqvist, E. Gualtieri, S. Hannuschke, R. Lacey, W.J. Llope, T. Reposeur, A.M. Vander Molen, G.D. Westfall, W.K. Wilson, J.S. Winfield, J. Yee, S.J. Yennello, A. Nadasen, R.S. Tickle, and E. Norbeck, Phys. Rev. Lett. **70**, 1924 (1993).

[Li94] T. Li, W. Bauer, D. Craig, E. Gualtieri, S. Hannuschke, R. Pak, A.M. Vander Molen, G.D. Westfall, J.S. Winfield, J. Yee, S.J. Yennello, R. Lacey, A. Nadasen, R.S. Tickle, and E. Norbeck, Phys. Rev. C **49**, 1630 (1994).

[Lisa95] M.A. Lisa, S. Albergo, F. Bieser, F.P. Brady, Z. Caccia, D.A. Cebra, A.D. Chacon, J.L. Chance, Y. Choi, S. Costa, J.B. Elliot, M.L. Gilkes, J.A. Hauger, A.S. Hirsch, E.L. Hjort, A. Insolia, M. Justice, D. Keane, J. Kintner, H.S. Matis, M. McMahan, C. McParland, D.L. Olson, M.D. Partlan, N.T. Porile, R. Potenza, G. Rai, J. Rasmussen, H.G. Ritter, J. Romanski, J.L. Romero, G.V. Russo, R. Scharenberg, A. Scott, Y. Shao, B.K. Srivastava, T.J.M. Symons, M. Tincknell, C. Tuvé, S. Wang, P. Warren, G.D. Westfall, H.H. Wieman, and K. Wolf, Phys. Rev. Lett. **72**, 2662 (1995).

[Llop95a] W.J. Llope, J.A. Conrad, C.M. Mader, G. Peilert, W. Bauer, D. Craig, E. Gualtieri, S. Hannuschke, R.A. Lacey, J. Lauret, T. Li, A. Nadasen, E. Norbeck, R. Pak, N.T.B. Stone, A.M. Vander Molen, G.D. Westfall, J. Yee, and S.J. Yennello, Phys. Rev. C **51**, 1325 (1995).

[Llop95b] W.J. Llope, W. Bauer, D. Craig, E.E. Gualtieri, S.A. Hannuschke, R.A. Lacey, J. Lauret, T. Li, C.M. Mader, A. Nadasen, E. Norbeck, R. Pak, G. Peilert, N.T.B. Stone, A.M. Vander Molen, G.D. Westfall, J. Yee, and S.J. Yennello, Phys. Rev. C **52**, 1900 (1995).

[Llop95c] W.J. Llope, S.E. Pratt, N. Frazier, R. Pak, D. Craig, E.E. Gualtieri, S.A. Hannuschke, N.T.B. Stone, A.M. Vander Molen, G.D. Westfall, J. Yee, R.A. Lacey, J. Lauret, A.C. Mignerey, and D.E. Russ, Phys. Rev. C **52**, 2004 (1995).

[Moli85a] J.J. Molitoris and H. Stöcker, Phys. Rev. C **32**, 346 (1985).

[Moli85b] J.J. Molitoris and H. Stöcker, Phys. Lett. **162B**, 47 (1985).

[Moli86] J.J. Molitoris, D. Hahn, and H. Stöcker, Nucl. Phys. **A447**, 13c (1986).

[Morr94] D.J. Morrissey, W. Benenson, and W.A. Friedman, Ann. Rev. Nucl. Part. Sci. **44**, 27 (1994).

[More92] L.G. Moretto, K. Tso, N. Colonna, and G.J. Wosniak, Phys. Rev. Lett. **69**, 1884 (1992).

[Ogil89a] C.A. Ogilvie, D.A. Cebra, J. Clayton, S. Howden, J. Karn, A. Vander Molen, G.D. Westfall, W.K. Wilson, and J.S. Winfield, Phys. Rev. C **40**, 654 (1989).

[Ogil89b] C.A. Ogilvie, D.A. Cebra, J. Clayton, P. Danielewicz, S. Howden, J. Karn, A. Nadasen, A. Vander Molen, G.D. Westfall, W.K. Wilson, and J.S. Winfield, Phys. Rev. C **40**, 2592 (1989).

[Ogil90] C.A. Ogilvie, W. Bauer, D.A. Cebra, J. Clayton, S. Howden, J. Karn, A. Nadasen, A. Vander Molen, G.D. Westfall, W.K. Wilson, and J.S. Winfield, Phys. Rev. C **42**, R10 (1990).

[Pak92] R. Pak, W.J. Llope, D. Swan, J. Wagner, G.D. Westfall, D. Craig, E. Gualtieri, S. Hannuschke, T. Li, N. Stone, A.M. Vander Molen, and J. Yee, NSCL/MSU Ann. Rep. 233 (1992).

[Pak93] R. Pak, W.J. Llope, D. Swan, J. Wagner, G.D. Westfall, D. Craig, E. Gualtieri, S. Hannuschke, N. Stone, A.M. Vander Molen, and J. Yee, NSCL/MSU Ann. Rep. 244 (1993).

[Pak95] R. Pak, W.J. Llope, D. Craig, E.E. Gualtieri, S.A. Hannuschke, R.A. Lacey, J. Lauret, A.C. Mignerey, D.E. Russ, N.T.B. Stone, A.M. Vander Molen, G.D. Westfall, and J. Yee, "Advances in Nuclear Dynamics, Proc. of the 11^{th} Winter Workshop on Nuclear Dynamics", eds. W. Bauer, Key West, Florida (1995).

[Pak96a] R. Pak, W.J. Llope, D. Craig, E.E. Gualtieri, S.A. Hannuschke, R.A. Lacey, J. Lauret, A.C. Mignerey, D.E. Russ, N.T.B. Stone, A.M. Vander Molen, G.D. Westfall, and J. Yee, Phys. Rev. C (in press).

[Pak96b] R. Pak, D. Craig, E.E. Gualtieri, S.A. Hannuschke, R.A. Lacey, J. Lauret, W.J. Llope, N.T.B. Stone, A.M. Vander Molen, G.D. Westfall, and J. Yee, submitted to Phys. Rev. C.

[Pan93] Q. Pan and P. Danielewicz, Phys. Rev. Lett. **70**, 2062 (1993).

[Peil89] G. Peilert, H. Stöcker, W. Greiner, A. Rosenhauer, A. Bohnet, and J. Aichelin, Phys. Rev. C **39**, 1402 (1989).

[Peil94] G. Peilert, H. Stöcker, and W. Greiner, Rep. Prog. Phys. **57**, 533 (1994).

[Pete90a] J. Péter, J.P. Sullivan, D. Cussol, G. Bizard, R. Brou, M. Louvel, J.P. Patry, R. Régimbart, J.C. Steckmeyer, B. Tamain, E. Crema, H. Doubre, K. Hagel, G.M. Jin, A. Péghaire, F. Saint-Laurent, Y. Cassagnou, R. Legrain, C. Lebrun, E. Rosato, R. MacGarth, S.C. Jeong, S.M. Lee, Y. Nagashima, T. Nakagawa, M. Ogihara, J. Kasagi, and T. Motobayashi, Phys. Lett. B **237**, 187 (1990).

[Pete90b] J. Péter, J.P. Sullivan, D. Cussol, G. Bizard, R. Brou, M. Louvel, J.P. Patry, R. Régimbart, J.C. Steckmeyer, B. Tamain, E. Crema, H. Doubre, K. Hagel, G.M. Jin, A. Péghaire, F. Saint-Laurent, Y. Cassagnou, R. Legrain, C. Lebrun, E. Rosato, R. MacGarth, S.C. Jeong, S.M. Lee, Y. Nagashima, T. Nakagawa, M. Ogihara, J. Kasagi, and T. Motobayashi, Nucl. Phys. **A519**, 127c (1990).

[Pete92] J. Péter, Nucl. Phys. **A545**, 173c (1992).

[Phai92] L. Phair, D.R. Bowman, C.K. Gelbke, W.G. Gong, Y.D. Kim, M.A. Lisa, W.G. Lynch, G.F. Peaslee, R.T. de Souza, M.B. Tsang, and F. Zhu, Nucl. Phys. **A548**, 489 (1992).

[Pogg95] G. Poggi, G. Pasquali, M. Bini, P. Mauerenzig, A. Olmi, N. Taccetti, J.P. Alard, V. Amouroux, Z. Basrak, N. Bastid, I.M. Belayev, L. Berger, Th. Blaich, S. Boussange, A. Buta, R. Čaplar, C. Cerruti, N. Cindro, J.P. Coffin, R. Donà, P. Dupieux, M. Dželalija, J. Erö, Z.G. Fan, P. Fintz, Z. Fodor, L. Fraysse, R. Freifelder, S. Frolov, A. Gobbi, Y. Grigorian, G. Guillaume, N. Herrmann, K.D. Hildenbrand, S. Hölbling, A. Houari, S.C. Jeong, F. Jundt, J. Kecskemeti, P. Koncz, Y. Korchagin, R. Kotte, M. Krämer, C. Kuhn, M. Ibnouzahir, I. Legrand, A. Lebedev, C. Maguire, V. Manko, G. Mgebrishvili, J. Mösner, D. Moisa, G. Montarou, I. Montbel, P. Morel, W. Neubert, D. Pelte, M. Petrovici, F. Rami, V. Ramillien, W. Reisdorf, A. Sadchikov, D. Schüll, Z. Seres, B. Sikora, V. Simion, S. Smolyankin, U. Sodan, K. The, R. Tezkratt, M. Trzaska, M.A. Vasiliev, P. Wagner, J.P. Wessels, T. Wienold, Z. Wilhelmi, D. Wohlfarth, A.V. Zhilin, and P. Danielewicz, Nucl. Phys. **A586**, 755 (1995).

[Rand93] J. Randrup, Comp. Phys. Comm. **77**, 153 (1993).

[Sche74] W. Scheid, H. Müller, and W. Greiner, Phys. Rev. Lett. **32**, 741 (1974).

[Schu95] F. Schussler, H. Nifenecker, B. Jakobsson, V. Kopljar, K. Söderström, S. Leray, C. Ngô, S. Souza, J.P. Bondorf, and K. Sneppen, Nucl. Phys. **A584**, 704 (1995).

[Shen93] W.Q. Shen, J. Péter, G. Bizard, R. Brou, D. Cussol, M. Louvel, J.P. Patry, R. Régimbart, J.C. Steckmeyer, J.P. Sullivan, B. Tamain, E. Crema, H. Doubre, K. Hagel, G.M. Jin, A. Péghaire, F. Saint-Laurent, Y. Cassagnou, R. Legrain, C. Lebrun, E. Rosato, R. MacGarth, S.C. Jeong, S.M. Lee, Y. Nagashima, T. Nakagawa, M. Ogihara, J. Kasagi, and T. Motobayashi, Nucl. Phys. **A551**, 333 (1993).

[Siem79] P.J. Siemens and J.O. Rasmussen, Phys. Rev. Lett. **42**, 880 (1979).

[Soff95] S. Soff, S.A. Bass, Ch. Hartnack, H. Stöcker, and W. Greiner, Phys. Rev. C **51**, 3320 (1995).

[Stoc86] H. Stöcker and W. Greiner, Phys. Rep. **137**, 277 (1986).

[Sull90] J.P. Sullivan, J. Péter, D. Cussol, G. Bizard, R. Brou, M. Louvel, J.P. Patry, R. Régimbart, J.C. Steckmeyer, B. Tamain, E. Crema, H. Doubre, K. Hagel, G.M. Jin, A. Péghaire, F. Saint-Laurent, Y. Cassagnou, R. Legrain, C. Lebrun, E. Rosato, R. MacGarth, S.C. Jeong, S.M. Lee, Y. Nagashima, T. Nakagawa, M. Ogihara, J. Kasagi, and T. Motobayashi, Phys. Lett. B **249**, 8 (1990).

[Sull92] J.P. Sullivan and J. Péter, Nucl. Phys. **A540**, 275 (1992).

[Tsan84] M.B. Tsang, C.B. Chitwood, D.J. Fields, C.K. Gelbke, D.R. Klesch, W.G. Lynch, K. Kwiatkowski, and V.E. Viola Jr. Phys. Rev. Lett. **52**, 1967 (1984).

[Tsan89] M.B. Tsang, G.F. Bertsch, W.G. Lynch, and M. Tohyama, Phys. Rev. C **40**, 1685 (1989).

[VMol95] A.M. Vander Molen, private communication.

[West76] G.D. Westfall, J. Gosset, P.J. Johansen, A.M. Poskanzer, W.G. Meyer, H.H. Gutbrod, A. Sandoval, and R. Stock, Phys. Rev. Lett. **37**, 1202 (1976).

[West85] G.D. Westfall, J.E. Yurkon, J. Van der Plicht, Z.M. Koenig, B.V. Jacak, R. Fox, G.M. Crawley, M.R. Maier, B.E. Hasselquist, R.S. Tickle, and D. Horn, Nucl. Instr. and Methods **A238**, 347 (1985).

[West93] G.D. Westfall, W. Bauer, D. Craig, M. Cronqvist, E. Gualtieri, S. Hannuschke, D. Klakow, T. Li, T. Reposeur, A.M. Vander Molen, W.K. Wilson, J.S. Winfield, J. Yee, S.J. Yennello, R.A. Lacey, A. Elmaani, J. Lauret, A. Nadasen, and E. Norbeck, Phys. Rev. Lett. **71**, 1986 (1993).

[Wilk52] D.H. Wilkinson, Rev. Sci. Instr. **23**, 414 (1952).

[Wils90] W.K. Wilson, W. Benenson, D.A. Cebra, J. Clayton, S. Howden, J. Karn, T. Li, C.A. Ogilvie, A. Vander Molen, G.D. Westfall, J.S. Winfield, B. Young, and A. Nadasen, Phys. Rev. C **41**, R1881 (1990).

[Wils91a] W.K. Wilson, D. Cebra, S. Howden, J. Karn, D. Krofcheck, R. Lacey, T. Li, A. Nadasen, T. Reposeur, A. Vander Molen, C.A. Ogilvie, G.D. Westfall, and J.S. Winfield, Phys. Rev. C **43**, 2696 (1991).

[Wils91b] W.K. Wilson, Ph.D. Thesis, Michigan State University (1991).

[Wils92] W.K. Wilson, R. Lacey, C.A. Ogilvie, and G.D. Westfall, Phys. Rev. C **45**, 738 (1992).

[Wils95] W.K. Wilson, W. Bauer, D. Cebra, M. Cronqvist, D. Krofcheck, R. Lacey, T. Li, A. Nadasen, E. Norbeck, T. Reposeur, A. Vander Molen, C.A. Ogilvie, G.D. Westfall, J.S. Winfield, and J. Yee, Phys. Rev. C **51**, 3136 (1995).

[Yee95] J. Yee, E.E. Gualtieri, D. Craig, S.A. Hannuschke, T. Li, W.J. Llope, R. Pak, N.T.B. Stone, A.M. Vander Molen, G.D. Westfall, J.S. Winfield, S.J. Yennello, Roy A. Lacey, A. Nadasen, and E. Norbeck, Phys. Lett. B **356**, 191 (1995).

[Zhan90] W.M. Zhang, R. Madey, M. Elaasar, J. Schambach, D. Keane, B.D. Anderson, A.R. Baldwin, J. Cogar, J.W. Watson, G.D. Westfall, G. Krebs, and H. Wieman, Phys. Rev. C **42**, R491 (1990).